Construction of a Single Beam SERF Magnetometer using Potassium Atoms for GNOME

Sun Yool Park

Department of Physics and Astronomy
of Oberlin College

April, 2019

Executive Summary

Since the discovery of dark matter, a number of theories have been proposed to explain what it may consist of. Among these theories is the idea of ultralight axion-like particles. These particles are thought to behave like fields, rather than individual particles just as photons behave like light fields. The random distribution of these particles could have formed topological defects such as domain walls. These defects interact with the spins of elementary particles. This coupling creates a pseudo magnetic field (magnetic-like interaction) which can be detected with an optical magnetometer. An optical magnetometer measures shifts in the energy levels of atoms that occur in the presence of a magnetic field in order to measure the field. The Stalnaker lab at Oberlin College is part of the **G**lobal **N**etwork of **O**ptical **M**agnetometers to search for **E**xotic physics (GNOME). GNOME looks for transient signals from the Earth going through defects, like domain walls, using a network of optical magnetometers. The data collected by each magnetometer are recorded with time synchronization through the global positioning system (GPS). The analysis of the correlation of the signals from different locations not only allows the differentiation of true signals from false positives, but also reveals the spatiotemporal character of such defects.

This experiment investigates the construction and characterization of a single-beam, spin-exchange-relaxation-free (SERF) magnetometer using potassium (K) atoms. The vapor cell, containing K, Rb, and ^{3}He atoms, is housed within four magnetic shields to reduce any external magnetic fields. Circularly polarized light, resonant with the K D1 transition (770 nm), optically pumps the K atoms into a dark state, leading to increased transmission of the light through the vapor cell. In the presence of a magnetic field, the atoms will precess out of the dark state, resulting in decreased transmission. We monitor the transmission signal and apply currents through the coils inside the shields to maintain zero magnetic field. The amount of the currents needed to zero the magnetic field provides a measurement of the residual magnetic field. The future plans to construct a Rb-K-^{3}He SERF comagnetometer, which has higher sensitivity, will also be presented.

Acknowledgment

First of all, I would like to thank my research advisor, Professor Jason Stalnaker, for giving me the opportunity to work in his lab. He always showed enthusiasm for physics and taught me how fun physics can be. His patience and support have inspired me to pursue my career in physics.

To all the physics professors at Oberlin college who have always showed caring and love: you have made learning physics fun and exciting. I am very grateful for the opportunities to have learned from you.

I would like to thank my physics friends, as well as my fellow Honors students, for their encouragement and caring. Special thanks goes to Diane Doman for always checking with us to see how we are and for her delightful presence in the physics building.

I would also like to thank my lab mates, Claire Segura, Dhruv Tandon, Eleda Fernald, and Seraphina Nix. They have made solving physics problems enjoyable and always made me feel at home in the lab. I will miss them incredibly. Claire, I hope we become the next Jason-Derek pair. Go Laser Team!

I would like to thank the whole GNOME collaboration. Special thanks to Szymon Pustelny at Jagiellonian Univeristy in Krakow, Poland for building the data acquisition box and Antoine Weis at University of Fribourg in Fribourg, Switzerland for building the sanity box used in the experiment.

Finally, thank you to my best friend Daniel Katz for proof-reading my thesis and for always being there for me over the past four years. You have truly made my undergraduate experience invaluable.

This work is supported by the US National Science Foundation, Collaborative Research (RUI): Search for Exotic Transient Spin-dependent Signals from Ultralight Dark Matter Fields (PHY-1707803).

Contents

List of Figures

List of Tables

Chapter 1

Introduction

Ordinary matter is only 5% of the energy and mass of the Universe. Dark energy and dark matter make up the remaining 75% and 20% of the Universe's energy budget, respectively. Since the discovery of dark matter, a number of theories have been proposed (for instance, see Refs. [1, 2]). However, none of the proposed theories have been experimentally verified, and the nature of dark matter remains unknown.

One of the candidates for dark matter is the axion. The axion originally was developed as a solution to the strong-CP problem [3]. Axions or axion-like particles (ALPs) are ultralight spin-0 bosons that are not predicted by the Standard Model. The existence of axions or ALPs is well-motivated not only as a possible constituent of dark matter, but also as a solution to several issues in a number of other areas, including the extra-dimensional problems in string theory [4] and the hierarchy problem [5]. Additionally, ALPs are of interest because there are many astrophysical phenomena, such as star evolution, that may indicate the existence of such particles with a coupling strength that can be detected in laboratory experiments [6].

There are a number of experiments searching for axions or axion-like particles. The haloscope experiments, such as ADMX (Axion Dark Matter eXperiment) [7] or HAYSTAC (Haloscope At Yale Sensitive To Axion Cold dark matter) [8], use a resonant cavity with a large applied magnetic field to search for galactic halo axions and ALPs that couple to photons [9]. The Cosmic Axion Spin Precession Experiment (CASPEr)

uses nuclear magnetic resonance (NMR) to detect axion dark matter that causes the spin-precession of nucleons [10]. For a review of axion search experiments, see Ref. [11]. Here, we describe the development of an optical magnetometer that was integrated into a global network as part of the Global Network of Optical Magnetometers to search for Exotic physics (GNOME) experiment.

1.1 The Global Network of Optical Magnetometers to search for Exotic physics (GNOME)

A lot of the axion search experiments, including the ones mentioned earlier, are sensitive to exotic particles whose mass is on the order of or greater than μeV. The Global Network of Optical Magnetometers to search for Exotic physics (GNOME) is sensitive to exotic particles with lighter mass, $<$ neV. This mass region in exotic particle parameter space has not been explored much by current experiments.

GNOME looks for stable topological defects that consist of ALPs. Unlike many other dark matter search experiments discussed earlier, GNOME uses a network of magnetometers that are geographically separated to search for transient signals from a potential exotic field with astrophysical origin passing through the Earth. The network of magnetometers provides two major advantages: first, we can distinguish a true signal from false positives. For instance, it is possible to get a false signal from factors like magnetic-field spikes, laser mode hops, etc. Such false signals can be vetoed by looking at the data from other stations. Second, we can learn about spatiotemporal characteristics of the topological defect. For instance, when there is a transient signal from a topological object, by looking at the relative timing of the signal at different stations, we can resolve the velocity or the width of the object.

One of the topological defects that GNOME is searching for could arise from the formation of ALP domain wall. In the early Universe, it is possible that the random distribution of the vacuum expectation values of the ALPs formed a domain-wall-like

defect as the Universe expanded and cooled [12, 13]. The domain walls separate regions with different energy vacua in space.

If we let the hypothetical ALP pseudoscalar field be $a(\mathbf{r})$, the two possible Hamiltonians describing the coupling between the field $a(\mathbf{r})$ and the atomic spins $\mathbf{S}$ (both electron and nuclear) are defined as [12]

$$\begin{aligned} H_a &= \frac{\hbar c}{(f_i)}\mathbf{S}\cdot\nabla a(\mathbf{r}), \\ H_a &= \frac{\hbar c}{(f_i')^2}\mathbf{S}\cdot\nabla a^2(\mathbf{r}), \end{aligned} \tag{1.1}$$

where $\hbar$ is the reduced Planck's constant and f_i is the effective decay constant that is related to the coupling constant. The subscript i is for different elementary particles (electrons, protons, and neutrons), and the term f_i could be different for different particles. The first Hamiltonian in Eq (1.1) is for the linear interaction, and the second one is for the quadratic interaction. As shown Eq (1.1), the gradient of the ALP field ∇a couples to the spins of elementary particles. This suggests that when ordinary matter goes from one region to another with a different vacuum expectation value it experiences a spin-dependent energy shift. Such events are referred to as domain wall crossing events.

The thickness of the domain walls d is determined as [13]

$$d = \frac{2\hbar}{m_a c}, \tag{1.2}$$

where c is the speed of light and m_a is the mass of the particles (ALPs). This suggests that the mass of the particles limit the duration of the transient signal from the domain walls. The duration of the signal is $\Delta t = d/v_\perp$, where $v_\perp$ is the relative normal speed between the domain wall and the Earth.

The domain walls are assumed to be much larger than the Earth, so the domain wall appears from the Earth to be a plane [12]. In addition, the mean velocity of domain walls is stationary relative to the motion of the Earth in the Milky Way.

Figure 1.1 shows the schematic of the network of magnetometer sensors going through the domain walls.

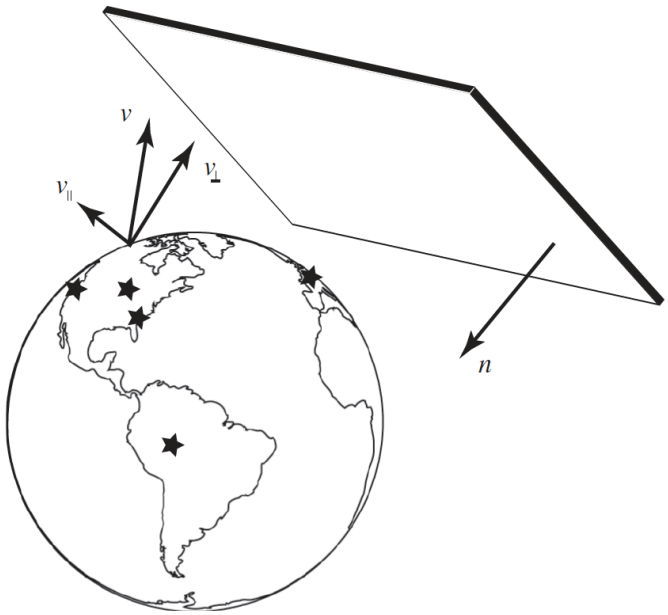

Figure 1.1: Schematic of GNOME magnetometers flying through a domain wall in space. The domain wall is a lot larger than the Earth; therefore the wall appears to be a plane from the Earth. The data at all stations are taken with GPS time stamps, and this allows determination of spatiotemporal characteristics of the domain wall. The figure is taken from Ref. [12].

1.1.1 Optical Magnetometer

When ordinary matter goes through a region with an ALP field gradient, it experiences a spin-dependent energy shift which shows up as a pseudo magnetic field in optical magnetometers. Optical magnetometers measure the dynamics of the spin ensembles, which are determined by magnetic fields and possibly exotic spin-coupling fields; therefore, optical magnetometers can be used to probe the interactions between the spins of elementary particles and hypothetical exotic fields that are not predicted by the Standard Model.

A vapor cell containing alkali-metal atoms is used in an optical magnetometer. The vapor cell is housed within multi-layer magnetic shields to reduce external magnetic noise, but the magnetometer remains sensitive to exotic spin coupling. The atoms in

the vapor cell are polarized by light. The spin-dependent energy shift due to the domain wall crossing events will appear as an effective magnetic field in the magnetometer. The magnetometers at GNOME stations use different atomic species and techniques, but the basic principles are the same. Each magnetometer has a sensitive axis along which the energy shift due to the domain walls can de detected. The characterizations of the first six magnetometers that were used for Science Run 1 can be found in Ref. [14].

1.1.2 Detection

The magnetic data from all GNOME stations are recorded with Global Positioning System (GPS) time stamps by data acquisition boxes designed by the GNOME group at Jagiellonian University in Krakow, Poland. The bandwidth of the GNOME magnetometers is around 100 Hz, and this provides temporal resolution of ≤ 10 ms. In addition, as discussed in section 1.1, the mass of the particles are related to the thickness of the domain walls, which directly affects the duration of the transient signal. The 100 Hz bandwidth suggests that GNOME is sensitive to ALPs with mass ≤ 0.01 neV. The data are taken at a sampling rate of 512 Hz.

The time period over which the Earth passes through the domain wall can be calculated from a simple equation

$$d = v\ t \tag{1.3}$$

where $v \sim 300$ km/s is the speed at which the Earth orbits around the galactic center and $d = 12,800$ km is the diameter of the earth. Solving for t, we get $t \sim 40$ seconds. This suggests that there would be up to ~ 40 second delays between transient signals from domain walls at different GNOME stations.

The magnetometer system includes a sanity box designed and built by the GNOME group at University of Fribourg in Switzerland. The sanity box has an external accelerometer, a magnetometer, a temperature sensor, and several inputs from the magnetometer which are compared against a preset range to monitor the "saneness" of the data. This serves to veto data that were acquired when there was some external problem with the apparatus.

In Science Run 1, six magnetometers recorded data continuously starting in June of 2017. Ten magnetometers participated in Science Run 2, which started in December of 2017. The data from Science Runs 1 and 2 are currently being analyzed. These data will be used to put constraints on the mass and the coupling constants of ALPs. Science Run 3 is currently underway. The eleven participating magnetometers are located in: Oberlin, USA; Lewisburg, USA; Daejeon, South Korea; Beijing, China; Hefei, China; Mainz, Germany; Krakow, Poland; Fribourg, Switzerland; Hayward, USA; and two in Berkeley, USA. Four additional magnetometer are under construction in Australia, Israel, India, and Los Angels, USA.

1.2 Thesis Structure

In this thesis, the construction of the single-beam SERF magnetometer using potassium atoms will be discussed. In Chapter 2, some basic concepts of atomic magnetometry will be reviewed. The experimental setup for the first-generation K magnetometer will be discussed in Chapter 3. In Chapter 4, the characteristics of the K magnetometer are presented and discussed. Chapter 5 includes theory regarding the second-generation magnetometer, the Rb-K-^{3}He comagnetometer, which uses effects of hybrid pumping and nuclear-electron spin coupling, as well as some experimental investigations on hybrid pumping. The thesis is concluded in Chapter 6.

Chapter 2

Optical Magnetometry Theory

Optical magnetometry uses light to measure the response of atoms to magnetic fields. Atoms have magnetic moments, which are intrinsic properties of the atoms that result from their constituent electrons, nuclei, and electronic orbital motion. In a magnetic field $\mathbf{B}$, the magnetic moment $\boldsymbol{\mu}$ feels torque $\boldsymbol{\tau}$ according to

$$\boldsymbol{\tau} = \boldsymbol{\mu} \times \mathbf{B}. \tag{2.1}$$

The magnetic field component transverse to the magnetic moment causes the magnetic moment to precess about $\mathbf{B}$ at the Larmor frequency $\Omega_{Larmor} = \gamma B_{\perp}$, where γ is the gyromagnetic ratio of the atomic species used. Atomic magnetometers use the relationship between the magnetic moment and the magnetic field to measure the magnetic field present.

Optical magnetometry uses the process of optical pumping. Through optical pumping, atoms can be polarized to have a certain angular momentum. Generally, an optical magnetometer is based on the following principles: (1) atoms are optically pumped into a polarized state, (2) the magnetic moment of the atoms precess about the magnetic field, and as a result, the angular momentum of the atoms also precess, and (3) the change in the direction of the atomic angular momenta affect the atom-light interaction. This changing interaction is detected and interpreted in terms of a magnetic field.

In the following sections, some basic theories of atomic physics and optical magnetometry are reviewed.

2.1 Atomic Energy Levels

Alkali metal atoms are of interest because of their high vapor pressure and easily accessible transitions. Additionally, they can easily be put in a vapor cell. Alkali metal atoms have only one valence electron; the energy of the atoms can be well approximated by considering only the valence electron outside of a central potential formed by the nucleus and closed shells. The valence electron has a spin of $S = 1/2$. For all alkali atoms, the ground state is the s shell, which has an angular momentum of $L = 0$. The first excited state is the p shell with $L = 1$.

2.1.1 Fine Structure Splitting

The fine structure splits the $L = 1$ state of alkali atoms into two different energies. Fine structure splitting is due to: (1) magnetic interactions between electron spin angular momentum $\hat{\mathbf{S}}$ and the electron orbital angular momentum $\hat{\mathbf{L}}$ (called spin-orbit coupling) and (2) relativistic corrections in the kinetic energy in the Hamiltonian. More rigorous derivations of fine structures can be found in Refs. [15, 16].

Spin-orbit coupling arises from the interaction of the magnetic moment of the electron with the magnetic field generated by the proton "orbiting" around the electron in the electron's rest frame. This field puts a torque on the electron and the energy eigenstates are the states with the magnetic moment of the electron aligned and anti-aligned with the field. The effective Hamiltonian of the spin-orbit interaction $\hat{H}'$ is [15]

$$\begin{aligned} \hat{H}' &= \xi \hat{\mathbf{L}} \cdot \hat{\mathbf{S}}, \\ &= \frac{\xi}{2}(\hat{\mathbf{J}}^2 - \hat{\mathbf{S}}^2 - \hat{\mathbf{L}}^2), \end{aligned} \tag{2.2}$$

where ξ is some positive constant when the subshells are less than half-filled.

The energy eigenvalue is

$$\Delta E = \frac{\xi \hbar^2}{2}[J(J+1) - S(S+1) - L(L+1)]. \tag{2.3}$$

where J is the total electronic angular moment, S is the electronic spin angular momentum, and L is the orbital angular momentum. The values of J can range from $J = |L - S|$ to $J = L + S$ in integer steps. We can see that the spin-orbit coupling results in splitting of the energies for the states where $L > 0$. Note that for fine structure splitting, the energy eigenstates are also eigenstates of S, L, and J. The energy eigenstates of fine structure splitting are described by $|nL,^{2S+1} L_J\rangle$, where n is the principle quantum number, L is the orbital angular momentum, S is the electronic spin angular moment, and J is the total electronic angular momentum.

Figure 2.1 shows the fine structure of potassium. The ground state $L = 0$ of potassium does not split due to spin-orbit coupling. The first excited state $L = 1$ splits into two two states: $4p^2P_{1/2}$ and $4p^2P_{3/2}$. The transitions from the ground state to these states are known as the D1 and D2 transitions, respectively.

2.1.2 Hyperfine Structure Splitting

The hyperfine structure splitting results from the interaction between the electron's angular momentum and the electric and magnetic multipole fields of the nucleus [15]. Here, we investigate the interaction between the magnetic moment of the nucleus $\hat{\boldsymbol{\mu}_N}$ operator and the magnetic field $\mathbf{B}_e$ generated by the total magnetic moment associated with the electron. The Hamiltonian describing this interaction is

$$\begin{aligned} \hat{H}_{hf} &= -\hat{\boldsymbol{\mu}}_N \cdot \mathbf{B}_e, \\ &= A_{hf}\ \hat{\mathbf{I}} \cdot \hat{\mathbf{J}}, \\ &= \frac{A_{hf}}{2}(\hat{\mathbf{F}}^2 - \hat{\mathbf{I}}^2 - \hat{\mathbf{J}}^2), \end{aligned} \tag{2.4}$$

where A_{hf} is the hyperfine constant, $\hat{\mathbf{J}}$ is the total electron spin operator, $\hat{\mathbf{I}}$ is the nuclear spin operator, and $\hat{\mathbf{F}}$ is the total momentum operator of the atom. Note that

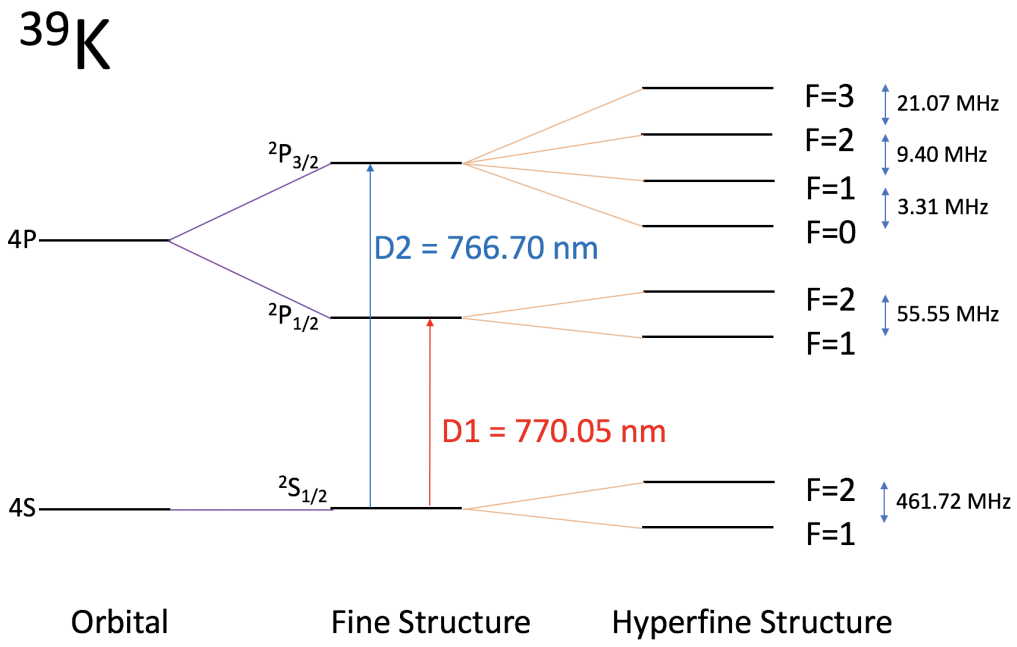

Figure 2.1: The energy levels of ^{39}K atoms (not drawn to scale). The ground and the excited states of K atoms are the s orbital with $L = 0$ and the p orbital with $L = 1$, respectively. The p orbital state is split into two different states $4^2P_{1/2}$ and $4^2P_{3/2}$ due to fine structure splitting. The transition to $4^2P_{1/2}$ and $4^2P_{3/2}$ are called the D1 and D2 transitions, and the wavelengths for each transition are 770.05 nm and 766.70 nm, respectively [17]. The fine structure energy levels are split further into F states due to hyperfine interaction.

the eigenstates of this Hamiltonian are also the eigenstates of $\mathbf{F} = \mathbf{I} + \mathbf{J}$. The energy eigenvalues are

$$E_{hf} = \frac{A_{hf}}{2}[F(F+1) - I(I+1) - J(J+1)]. \tag{2.5}$$

Since F can range from $F = |I - J|$ to $F = I + J$ in integer steps, we can see that the hyperfine interaction results in splitting of the energies. Each F state has degenerate energy levels M_F in the absence of a magnetic field. The M_F levels are the projection of the F state along some axis. The values of M_F can range from $-F, -F+1, ..., F-1, F$.

Note that for hyperfine structure, M_I and M_J are not good quantum numbers.

For hyperfine structure, the energy eigenstates are described by $|nL,\ ^{2S+1}L_J,\ F,\ M_F\rangle$, where n is the principle quantum number, L is the orbital angular momentum, F is the total momentum of the atom, and M_F is the projection of F along a given axis.

Potassium exists in two stable isotopes: ^{39}K and ^{41}K. The natural abundance of ^{39}K and ^{41}K are 93% and 6.7%, respectively. The majority of the K atoms used in this experiment is ^{39}K. The nuclear spin I for ^{39}K is $I = 3/2$. The states $4s^2S_{1/2}$ and $4p^2P_{1/2}$ are each split into two different states $F = I + 1/2$ and $F = I - 1/2$, separated by E_{hf} given in Eq (2.5). In the state $F = I + 1/2$, the atomic spin (F) and the nuclear spin (I) are both "aligned" with the electron spin J, and in the $F = I - 1/2$ state, the electron spin J is anti-aligned with the F and I. The state $4p^2P_{3/2}$ splits into four levels: $F = \{I - 3/2, I - 1/2, I + 1/2, I + 3/2\}$. The hyperfine structure of potassium is shown in Figure 2.1.

2.1.3 Notation

An energy state of an alkali atom can be represented with a principal quantum number of the valence shell and a term depending on **L**, **S**, and **J**. It is customarily written as

$$nL^{2S+1}L_J, \tag{2.6}$$

where n is the principal quantum number, S is the electronic spin angular momentum, L is the orbital angular momentum, and $\hat{\mathbf{J}} = \hat{\mathbf{L}} + \hat{\mathbf{S}}$ is the total electronic angular momentum operator. The value of L is denoted by a letter $S, P, D, F, ...$ corresponding to $L = 0, 1, 2, 3...$, respectively. The values of J can range from $J = |L - S|$ to $J = L + S$ in integer steps [15]. The angular momentum of the nuclear spin is represented by I. The total momentum operator of the atom F, therefore, is given by $\hat{\mathbf{F}} = \hat{\mathbf{I}} + \hat{\mathbf{J}}$, and the values of F range from $F = |I - J|$ to $F = I + J$ in integer steps.

2.1.4 Zeeman effect

In the presence of a static magnetic field, the magnetic moments of both protons and electrons interact with the external magnetic field. As a result, the degeneracies of the

magnetic Zeeman sublevels (the M_F levels) are lifted. For a sufficiently small magnetic field along the **z**-axis, the Hamiltonian describing the Zeeman effect is [18]

$$\begin{aligned} \hat{H}_B &= -(\hat{\boldsymbol{\mu}}_e + \hat{\boldsymbol{\mu}}_n) \cdot \mathbf{B} \\ &= g\mu_0 B\hat{J}_z/\hbar - g_n\mu_n B\hat{I}_z/\hbar, \end{aligned} \tag{2.7}$$

where $\hbar$ is the reduced Planck's constant, g is the g-factor of the electron, g_n is g-factor of the nucleus, μ_0 is the permeability of free space, μ_n is the nuclear magneton, $\hat{J}_z$ is the projection of the electron angular momentum along the z-axis, and $\hat{I}_z$ is the projection of the nuclear spin along the z-axis. Note that M_J and M_I are not good quantum numbers for the Hamiltonian in Eq (2.7). The eigenstates of this Hamiltonian are also the eigenstates of $\hat{\mathbf{F}} = \hat{\mathbf{I}} + \hat{\mathbf{J}}$. Therefore, M_F is a good quantum number to use, and the Hamiltonian becomes

$$\begin{aligned} \hat{H}_B &= -\hat{\boldsymbol{\mu}}_F \cdot \mathbf{B} \\ &= g_F\mu_F\hat{\mathbf{F}} \cdot \mathbf{B}, \end{aligned} \tag{2.8}$$

where

$$g_F = g_J\left[\frac{F(F+1)+J(J+1)-I(I+1)}{2F(F+1)}\right] - g_I\frac{m_e}{m_n}\left[\frac{F(F+1)+J(J+1)-I(I+1)}{2F(F+1)}\right]. \tag{2.9}$$

The energy eigenvalues for this Hamiltonian are

$$E = g_F\mu_B B M_F \tag{2.10}$$

Here, the axis of quantization for M_F is along $\mathbf{B}$. As we can see in Eq (2.10), the external magnetic field splits the M_F energy levels. In Eq (2.9), we can approximate the second term to be zero because the ratio of $m_e/m_n \sim 1/2000$. With this approximation, note that g_F is opposite signs for $F = 1$ and $F = 2$. This causes the two energy eigenstates $F = 1$ and $F = 2$ to precess in the opposite direction in a presence of a magnetic field.

2.2 Spin Evolution in a Magnetic Field

The Hamiltonian of an atom in an external magnetic field $\mathbf{B} = B\hat{\mathbf{z}}$ is [15]

$$\hat{H} = A_{hf}\hat{\mathbf{I}} \cdot \hat{\mathbf{J}} + g_F \mu_F \hat{\mathbf{F}} \cdot \mathbf{B}. \tag{2.11}$$

The first term is from the hyperfine interaction from Eq (2.4), and the second term arise from the Zeeman interaction between the magnetic moments of both electrons and protons in the atom and the external magnetic field from Eq (2.8). In low magnetic fields, the hyperfine interaction term is dominant over the other. When the magnetic field $\mathbf{B}$ is not along the axis of quantization for M_F, the external magnetic field creases a superposition of the M_F energy eigenstates. As a result, we get an evolution of the M_F state. The two hyperfine states precess with the frequency ω_F

$$\begin{aligned} \omega_{F=I\pm1/2} &= \pm\frac{g_e \mu_B B}{(2I+1)\hbar} \\ &= \pm\gamma B. \end{aligned} \tag{2.12}$$

The electron couples more strongly to the external magnetic field than the nuclear spin I.

The $(2I+1)$ term accounts for the dragging by the nuclear spin on the atomic spin precession. The opposite signs come from the fact that the two F states have opposite signs for g_F as discussed earlier, and this suggests for the potassium, the two states $F = 1$ and $F = 2$ precess in opposite directions.

2.3 Absorption Spectral Line

The shape of spectral lines are not only characteristic of the atoms under study, but also depend on the conditions under which the spectra are measured. There are two types of broadening of spectral lines: homogenous and inhomogeneous. For homogenous broadening mechanisms, such as pressure broadening, all atoms in the sample are affected the same way. On the other hand, inhomogeneous broadening mechanisms,

like Doppler broadening, affect individual atoms differently. In the following sections, we will discuss natural width of the spectral line, Doppler broadening, and pressure broadening.

2.3.1 Natural Line Width

The time-energy uncertainty relation prohibits atomic transitions from having discrete energies. According to the uncertainty principle [15, 19]

$$\begin{aligned} \Delta E \Delta t &= \hbar \tau \Delta\omega \geq \hbar, \\ \Delta\omega &\geq \frac{1}{\tau}, \end{aligned} \tag{2.13}$$

where $\hbar$ is the reduced Planck's constant, ω is the angular frequency of the transition, and τ is the lifetime of the transition. The uncertainty in time is τ and the energy $E = 2\pi\hbar\nu$; therefore, the natural line width Γ_0 becomes

$$\Gamma_0 = \frac{\Delta E}{2\pi\hbar} = \frac{1}{2\pi\tau}. \tag{2.14}$$

For potassium, the lifetime of the K D1 transition is 25 ns [15]. Using Eq (2.14), the natural line width of the K D1 transition Γ_0 is

$$\Gamma_0 = \frac{1}{2\pi\ 25 \times 10^{-9}\ \text{ns}} = 6\ \text{MHz}. \tag{2.15}$$

2.3.2 Inhomogeneous Broadening

In this section, Doppler Broadening, a type of inhomogeneous broadening, will be discussed. The root-mean-square thermal velocity of atoms with mass m is $v = \sqrt{3k_BT/m}$, where k_B is the Boltzmann constant and T is the temperature. If the atoms have some velocity along the direction of the laser, they experience a shift in the frequency of the laser because of the Doppler effect. The new frequency ν' then becomes

$$\nu' = \nu\left(1 - \frac{v_\parallel}{c}\right), \tag{2.16}$$

where $v_{\parallel}$ is the velocity component in the direction of the laser and c is the speed of light. This Doppler effect broadens the atomic resonance line width because as the frequency of the laser is detuned from the resonance frequency, some atoms have a velocity such that the frequency they experience is the resonance frequency. The probability of atoms in a vapor cell with mass m with a velocity v_z is described as [15]

$$P_v = \sqrt{\frac{m}{2\pi k_B T}} e^{-mv_z^2/2k_B T}. \tag{2.17}$$

The resulting absorption line width follows a Gaussian curve with full width at half maximum (FWHM) of

$$\Gamma_{\text{Dopper}} = \frac{\nu_0}{c}\sqrt{\frac{2k_B T \ln 2}{m}}, \tag{2.18}$$

where ν_0 is the resonance frequency.

For the K atoms at temperature $T = 165$ °C, the Doppler broadened width of the absorption is calculated to be $\Gamma_{Doppler} = 470$ MHz.

2.3.3 Homogeneous Broadening

When atoms in the sample undergo a lot of collisions with other atoms, in our case buffer gas, the lifetime of the transition is decreased. As a result, the line width is broadened. The broadened line shape due to the pressure broadening has a Lorentzian distribution [20, 21]

$$\mathcal{L}(\nu) = \frac{\Gamma^2/4}{(\nu - \nu_0)^2 + (\Gamma/2)^2}, \tag{2.19}$$

where Γ is the full width at half maximum (FWHM) and ν_0 is the resonance frequency.

An amagat (amg) is a unit for number density, and it is defined as the number density of ideal gas molecules at 1 atm and 0 °C. The number density in amg η is defined as

$$\eta = \frac{n}{n_0} = \left(\frac{p}{p_0}\right)\left(\frac{T_0}{T}\right) \text{ amg} \tag{2.20}$$

where $n_0 = 1$ amg $= 2.687 \times 10^{25}$ m^{-3} is the Loschmidt constant [22], $p_0 = 1$ atm, and $T_0 = 0$ °C $= 273$ K.

In the K-^{3}He ensemble, the pressure broadening of the K atoms is $\Gamma \simeq 13.2$GHz/amg [23]. The pressure of the vapor cell is 3 atm at room temperature; therefore, the pressured broadened K D1 line width would be $\Gamma_{Pressure} \simeq 39.6$ GHz. For the K magnetometer, the pressure broadening dominates over Doppler broadening ($\Gamma_{Pressure} \gg \Gamma_{Doppler}$). Therefore, Eq (2.19) will be used to describe the absorption spectral line of K atoms.

2.3.4 Absorption cross section

The absorption cross section describes the probability that a photon will be absorbed by an atom. The absorption cross-section of the homogeneous Lorentzian broadening is [15]

$$\sigma_{abs} = \frac{\lambda^2}{2\pi}\frac{2J'+1}{2J+1}\frac{\Gamma_p}{\Gamma_{Tot}}, \tag{2.21}$$

where λ is the wavelength of the transition, Γ_p is the natural line width of the transition, Γ_{Tot} is the total width of the transition including homogeneous broadening, and J and J' are the total electronic angular momenta of the ground and excited states, respectively.

Using Eq (2.21), the pressure broadened absorption cross-section for the K D1 transition in the 3 atm ^{3}He environment is calculated to be

$$\begin{aligned}\sigma_{abs} &= \frac{(770.109\times10^{-7}\text{ cm})^2}{2\pi}\frac{6\text{ MHz}}{39.6\text{ GHz}} \\ &= 1.4\times10^{-13}\text{ cm}^2.\end{aligned} \tag{2.22}$$

The optical depth of the vapor cell is defined as [20]

$$OD = n\sigma(\nu)l \tag{2.23}$$

where n is the density of the atoms in the vapor cell, σ is the absorption cross-section inside the vapor, and l is the length of the vapor cell. As light travels through the vapor cell and is absorbed by the atoms, the light is attenuated as a function of frequency ν according to

$$f(\nu) = f_0 e^{-n\sigma_0 l\frac{\Gamma^2/4}{\Gamma^2/4+(\nu-\nu_0)^2}} \tag{2.24}$$

where σ_0 is the absorption cross-section at the resonance frequency ν_0 and Γ is the broadened width of the absorption.

The density of K vapor as a function of temperature is shown in Figure 2.2. The K vapor density n_K can also be calculated using the empirical formula [20, 24]

$$n_K = \frac{10^{26.2682-(4453\text{K})/T}}{T/(\text{K})}\text{cm}^{-3}, \tag{2.25}$$

where T is the temperature in Kelvin. For this experiment, the atoms are heated to 165° C, which corresponds to a K vapor density of $n_K \sim 3 \times 10^{13}$ cm^{-3}.

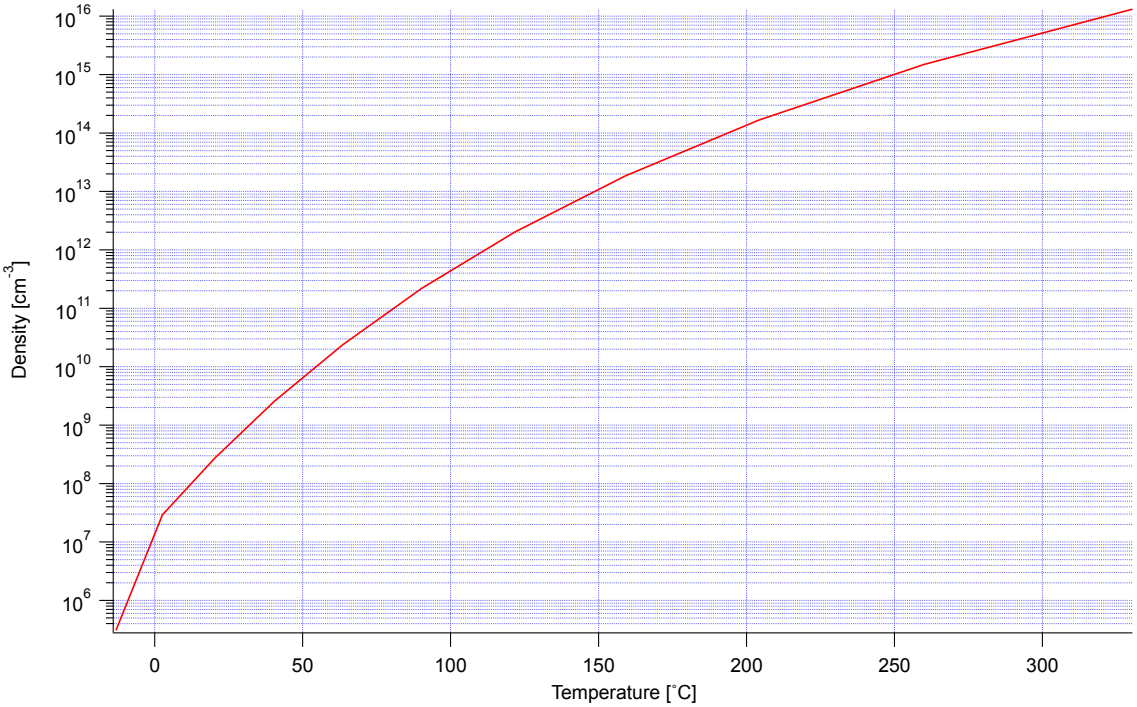

Figure 2.2: The K vapor density as a function of temperature. At 165 °C, the density is on the order of 10^{13} cm^{-3}. The data are from Ref. [25].

2.3.5 Excitation Rate

The excitation rate, or the pumping rate, is the rate at which the light is pumping the atoms into the excited state and is described by [21]

$$\Gamma_{pump} = \frac{d^2\varepsilon^2}{\Gamma}, \tag{2.26}$$

where d is the dipole moment of the transition, ε is the amplitude of the light electric field, Γ is the spontaneous decay rate from $|e\rangle$ to $|g\rangle$, i.e. the homogeneous width of the transition, and $\hbar$ is set to one.

2.3.6 Saturation

The saturation parameter describes how strongly the incident light will perturb the atomic states. The saturation parameter is defined as [15, 26]

$$\kappa \equiv \frac{\text{excitation rate}}{\text{relaxation rate}}. \tag{2.27}$$

In this case, the relaxation rate is Γ; therefore, the saturation parameter becomes

$$\kappa = \frac{d^2\varepsilon^2}{\Gamma^2}. \tag{2.28}$$

The dipole moment of the transition d is related to Γ. This suggests that the excitation rate can be calculated for a transition with a given Γ. The excitation rate can be used to calculate the saturation intensity for a given transition. The saturation intensity I_S for the specific transition at λ is given by [26]

$$I_S = \frac{\pi hc}{3\lambda^3\tau}, \tag{2.29}$$

where h is the Planck's constant, c is the speed of light, and τ is the lifetime of the transition. In the presence of quenching gas, the lifetime of the transition is decreased. Therefore, $I_{S,\text{quenching}} \gg I_{S,\text{no quenching}}$.

For the K D1 transition, using $\lambda = 770.109 \times 10^{-7}$ cm and $\tau = 25$ ns, the saturation intensity I_S is calculated to be $I_S = 1.8$ mW/cm^2. For a beam with a radius of about 0.3 cm, the saturation power P_S is calculated to be $P_S = 510$ μW. However, in the presence of quenching gas, the lifetime τ is a lot shorter. Using the line width of the pressure broadened K D1 transition $\Gamma_{\text{Pressure}} \simeq 39.6$ GHz and Eq (2.14), the lifetime of this broadened transition is calculated to be $\tau_{\text{Pressure}} \sim 4$ ps. The new saturation intensity for the broadened transition is $I_{S,\text{broadened}} = 11$ W/cm^2, and the saturation power for the beam with a radius of 0.3 cm is $P_{S,\text{broadened}} = 3$ W.

2.4 Optical Pumping

In circularly polarized light, all photons have the same spin projection in the direction of the propagation (in our case, the **x**-axis). When the light is σ^+ polarized, the photons in the beam carry angular momentum of $+1$ ($\hbar$) along the **x**-axis. This angular momentum can be transferred to the total angular momentum of the atom.

Optical pumping uses light to polarize both the electron spin S and the nuclear spin I of the atoms. Even though the K atoms have nuclear spin, we can consider only the optical pumping of the electron spin. The conditions under which we can consider the electron spin only are [27]: (1) circularly polarized light is used to excite the atoms in the ground state $S_{1/2}$ to the excited state $P_{1/2}$, (2) the pressure broadened absorption line is large enough that the hyperfine structure is not resolved, and (3) the quenching gas is present to reduce radiation trapping. In our system, we use light resonant with K D1 transition and the hyperfine structure is not resolved due to the pressure broadening. Furthermore, the photons will interact more strongly with the electronic spins than with the nuclear spins. The nuclear spins do interact with the photons, but this interaction can be accounted for by introducing a "slowing down" factor. The slowing down factor describes the reduced rate of the electronic spin polarization due to the loss of photon angular momentum to the nuclear spins in the atoms. Figure 2.3 shows the mechanism of the optical pumping.

In this experiment, the light is σ^+ polarized. Atoms in the $M_J = -1/2$ ground state transition to the $M'_J = +1/2$ excited state to conserve angular momentum. Since only the transitions where $M'_J = M_J + 1$ can occur, the atoms in the $M_J = +1/2$ ground state cannot absorb light and therefore get stuck in that state in the absence of collisions and external fields. The state $M_J = +1/2$ is called the dark state.

The collisions between the buffer gas ^{3}He and the K atoms "mix" the two excited states; in other words, the collisions repopulate the atoms equally between $M'_J = -1/2$ and $M'_J = +1/2$. The K atoms collide with the quenching gas N_2 and relax back to their ground state. Collisions with quenching gas remove the orbital angular momentum of the K atoms by transferring the angular momentum to the N_2 rotational states. The

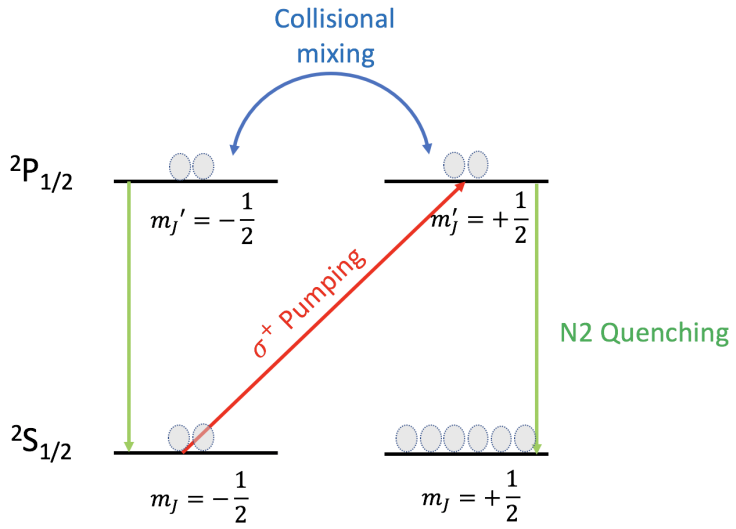

Figure 2.3: The optical pumping of the electron spin in the K atoms. The light with σ^+ polarization optically pumps the atoms from $M_J = -1/2$ into $M_J' = +1/2$. Collisions between the K atoms and the ^{3}He atoms cause collisional mixing of the two excited states and redistribute the population among the two states. Collisions with the quenching gas N_2 relax the excited K atoms back to their ground states without depolarizing the electron spins in other K atoms. Over time, the atoms are polarized into $M_J = +1/2$ called the dark state. Figure is based on Ref. [27]

quenching gas also reduces radiation trapping. Radiation trapping is a process in which the excited K atoms radiate unpolarized light that is reabsorbed by another K atom in the cell. Radiation trapping can be reduced by the presence of the quenching gas because the excited K atoms lose their polarization to the rotational states of N_2 (rather than depolarizing other K atoms) and relax back to the ground state where they can be re-excited via the pump light.

2.5 Spin Relaxation

In this section, we will discuss some fundamental and experimental parameters that will directly affect the sensitivity of the K magnetometer. The vapor cell for the K

magnetometer, which is housed within four layered magnetic shields, contains hybrid rubdium-potassium in a 10:90 ratio, 50 torr of N_2 as quenching gas, and 3 atm (2300 torr) of ^{3}He as buffer gas. The ^{3}He atoms are present in the cell for the planned second-generation comagnetometer, which uses the nuclear spin polarization of ^{3}He. The K atoms are polarized using circularly polarized light. Currents are applied through the magnetic coils in the shields to cancel out any residual magnetic field inside the shields. In the absence of collisions, when there is a magnetic field perpendicular to the **x**-axis, the K electronic spins precess about the magnetic field (see section 2.7). To build a sensitive magnetometer, we want this precession to be as coherent as possible in time. In other words, we want the spins to stay polarized as long as possible. The time over which the spins remain coherent is called the transverse relaxation time, or T_2. However, there are multiple processes that destroy this coherence. For instance, a K atom can collide with another K atom and exchange their spins, resulting in loss of polarization. A K atom can collide and exchange its spin with a ^{3}He atom, losing its polarization. A K atom can also go through a spin-destruction collision during which it collides with another K atom, with a ^{3}He atom, with a Rb atom, with N_2 gas, or with the wall of the vapor cell and loses its polarization. The total relaxation rate therefore becomes [20, 28]

$$R_{Total} = \frac{1}{T_2} = R_{se}^{\text{K-K}} + R_{se}^{\text{K-}^3\text{He}} + R_{sd}^{\text{collisions}} + R_D + R_{Pump} \tag{2.30}$$

where $R_{se}^{\text{K-K}}, R_{se}^{\text{K-}^3\text{He}}$, and $R_{sd}^{\text{collisions}}$ describe the relaxation rates due to the K-K spin-exchange collisions, K-He spin-exchange collisions, and spin-destruction collisions between K and other atoms present in the cell, respectively, R_D describes the relaxation rate due to the diffusion to the walls, and R_{Pump} is the relaxation rate due to the pumping. In the following sections, we will discuss the details of these relaxation rate terms.

2.5.1 Spin-Exchange Collisions

The optically pumped K atoms can go through spin-exchange collisions with each other and transfer polarization between electronic and nuclear spins [27]. The two atoms

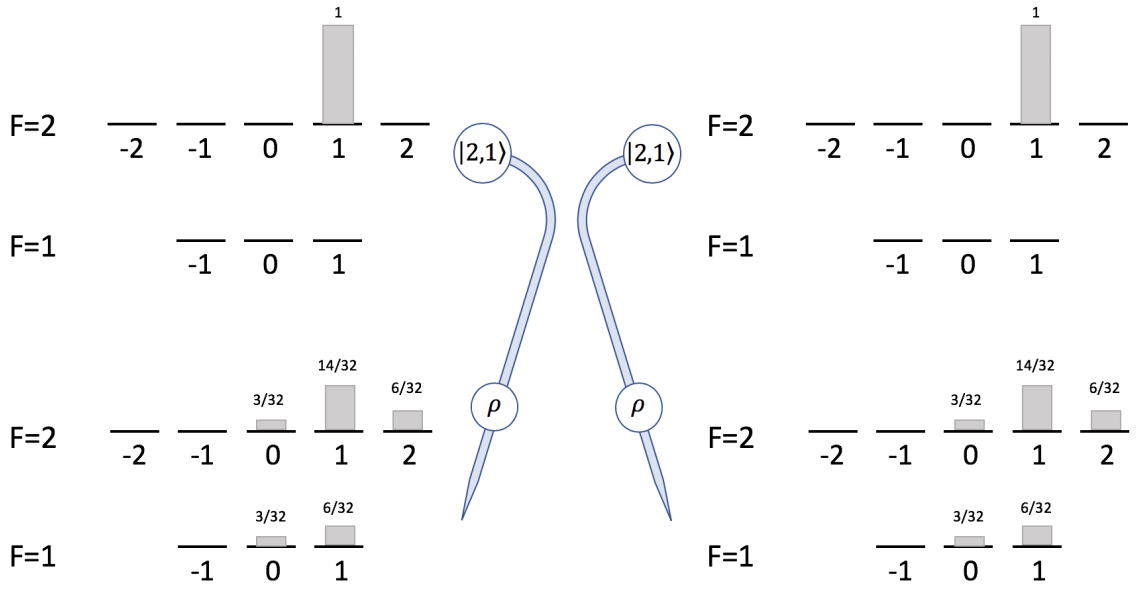

Figure 2.4: Spin-exchange collision between two K atoms. Initially, the two K atoms both in the state $|F, M_F\rangle = |2, 1\rangle$ collide with each other. The F number is conserved upon collision, but N_F is redistributed among different M_F levels. The atoms in the $F = 1$ states and $F = 2$ states precess in opposite directions. Therefore, spin-exchange collisions contribute to the relaxation of the K spins in the magnetometer. Figure is based on Ref. [27]

come together in an intermolecular potential and exchange their angular momentum, a process called a binary collision. The total spin angular momentum of the two colliding K atoms is conserved during a spin-exchange collision; this suggests that such a collision redistributes the angular momentum among the hyperfine sublevels of the ground state. Figure 2.4 shows two colliding K atoms, each with the state $|F, M_F\rangle = |2, 1\rangle$, and how the population of each sublevel is redistributed by the collision. Due to the large splitting of the singlet and triplet intermolecular potentials, the electron spins can rotate many times during a single collision [27]. As a result, the spin-exchange cross sections are large, on the order of 10^{-14} cm^2 [27]. The spin-exchange collisions contribute to the relaxation time T_2 because the collisions can change the F quantum number, and

this results in the change in the directions of the atom precession [28, 27]. Therefore, in a traditional atomic magnetometer, the spin-exchange collision relaxation rate is $R_{se}^{\text{K-K}} \simeq 1/T_{se}$, where T_{se} is the time between spin-exchange collisions. For typical conditions in the type of magnetometer we have (high pressure, presence of buffer gas), $1/T_{se} = 30,000$ 1/s [20].

However, in the regime where there is a very small magnetic field so that $R_{se} \gg \gamma B$, or in other words, when the spin-exchange collisions occur much faster than the precession rate, the spin-exchange relaxation mechanism vanishes [29]. In this regime, the two hyperfine states become "locked together" and precess at the rate given by [28]

$$\omega = \frac{g_e \mu_B B}{Q(P)\hbar} \quad \text{where} \quad Q(P) = 4\left(2 - \frac{4}{3+P^2}\right)^{-1}. \tag{2.31}$$

The factor Q is called the slowing-down factor. It is caused by the nuclear angular momentum [20, 28, 30]. The slowing down factor $Q(P)$ is a function of the polarization of the atomic ensemble. The slowing-down factor Q_0 at complete mixing $P = 0$ is defined as [28]

$$Q_0 = \frac{S(S+1) + I(I+1)}{S(S+1)} = 6. \tag{2.32}$$

For K atoms, $Q_0 = 6$ corresponds to the ensemble with low polarization (P=0). The slowing down factor of $Q = 4$ corresponds to the ensemble with full polarization (P=1). Note that when we fully polarize atoms so that only one particular hyperfine level is populated and $Q(P = 1) = 4$, the atoms precess with the frequency at which the $F = 2$ state does in Eq (2.12). This suggests that the particular state the atoms are polarized into is the $F = 2$ state; this is because there are 5 sublevels for the $F = 2$ state and therefore it has a higher statistical weight than the $F = 1$ state which has three sublevels. Figure 2.5 shows the distribution of atoms at different polarization levels. The ensemble with $Q = 5$ is achieved by many successive collisions, and it is called the "spin-temperature" distribution [27, 31]. Again, the total angular momentum $M_{F_1} + M_{F_2}$ is conserved in spin-exchange collisions. Once the atoms have the $|F, M_F\rangle = |2, 2\rangle$ state, they cannot accommodate the $F = 1$ state. Therefore, in a fully polarized ensemble, all atoms are in the $|F, M_F\rangle = |2, 2\rangle$ and precess at the same

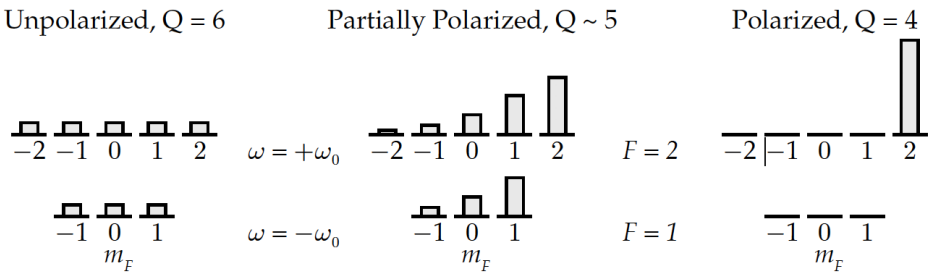

Figure 2.5: The distributions of populations among the hyperfine sublevels at equilibrium for unpolarized ($Q = 6$), partially polarized ($Q = 5$), and fully polarized ($Q = 4$) ensembles of K atoms in the presence of spin-exchange collisions. The partially polarized state is known as the spin-temperature distribution and can be achieved by many spin-exchange collisions in the ensemble. The figure is from Ref. [20].

frequency. As a result, in this regime where $R_{se} \gg \gamma B$, spin-exchange collisions do not contribute to the total relaxation rate; therefore, the $R_{se}^{\text{K-K}}$ disappears in the zero field environment. This regime is called the spin-exchange relaxation free (SERF) regime.

2.5.2 Spin-Destruction Collisions

In the SERF regime, where $R_{se}^{\text{K-K}}$ disappears, the relaxation due to spin-destruction collisions between K atoms and all the other elements in the cell becomes dominant. Upon a spin-destruction collision, the K atom loses its electron spin to translational or rotational degrees of freedom in the system [20]. The terms that contribute to $R_{sd}^{\text{collisions}}$ are [20]

$$R_{sd}^{\text{collisions}} = \sigma_{\text{K}}^{sd}\bar{v}n_{\text{K}} + \sigma_{\text{Rb}}^{sd}\bar{v}n_{\text{Rb}} + \sigma_{\text{He}}^{sd}\bar{v}n_{\text{He}} + \sigma_{\text{N}_2}^{sd}\bar{v}n_{\text{N}_2}, \tag{2.33}$$

where $\bar{v}$ is the average speed of the atoms in the vapor cell ($\bar{v} = \sqrt{8k_BT/\pi M}$), and $n_{\text{K}}, n_{\text{Rb}}, n_{\text{He}}$ and n_{N_2} are the densities of K, Rb, He, and N_2, respectively. The terms $\sigma_{\text{K}}^{sd}, \sigma_{\text{Rb}}^{sd}, \sigma_{\text{He}}^{sd}$, and $\sigma_{\text{N}_2}^{sd}$ are the spin-destruction cross sections of K with K, Rb, He, and N_2, respectively, and they are reported in Table 2.1. As Table 2.1 suggests, potassium was chosen to be the majority species for the electronic spins in our system because it

has a smaller spin-destruction cross section for both K-K collisions and K-He collisions when compared to Rb.

Alkali metal	$\sigma^{\mathrm{SD}}_{\mathrm{Self}}$	$\sigma^{\mathrm{SD}}_{\mathrm{He}}$	$\sigma^{SD}_{\mathrm{N_2}}$
K	1×10^{-18} [cm^2]	8×10^{-25} [cm^2]	7.9×10^{-23} [cm^2]
Rb	9×10^{-18} [cm^2]	9×10^{-24} [cm^2]	1×10^{-22} [cm^2]

Table 2.1: The spin-destruction cross section for the K and Rb atoms. These values were used to calculate the spin-destruction rates for existing collisions in the vapor cell to estimate the total spin-destruction collision rate. The table was adapted from Ref. [28]. The $\sigma^{SD}_{\mathrm{N_2}}$ for K was taken from Ref. [32].

At temperature $T = 165$ °C and $P = 3$ atm, using Eq (2.20) for n_{He} and Eq (2.25) for n_K,

$$R_{sd}^{\text{K-K}} = \sigma_{\mathrm{K}}^{sd} \bar{v} n_{\mathrm{K}} = 1.4 \text{ 1/s}, \tag{2.34}$$

$$R_{sd}^{\text{K-He}} = \sigma_{\mathrm{He}}^{sd} \bar{v} n_{\mathrm{He}} = 10 \text{ 1/s}. \tag{2.35}$$

In typical SERF magnetometer environment, the term $R_{sd}^{\text{K-Rb}}$ can be broken down to [33]

$$R_{sd}^{\text{K-Rb}} = \frac{n_{\mathrm{Rb}}}{n_{\mathrm{K}}} R_{sd}^{\mathrm{Rb}}, \tag{2.36}$$

where

$$R_{sd}^{\mathrm{Rb}} = R_{sd}^{\text{Rb-Rb}} + R_{sd}^{\text{Rb-}^3\text{He}} + R_{sd}^{\text{Rb-N}_2}. \tag{2.37}$$

In Eq (2.37), the terms describe the spin-destruction rate of Rb due to Rb-Rb, Rb-^{3}He, and Rb-N_2 collisions, in order. The terms in Eq (2.37) can be calculated using the

following expressions [33]

$$R_{sd}^{\text{Rb-Rb}} = 4.2 \times 10^{-13} n_{\text{Rb}}$$

$$R_{sd}^{\text{Rb-}^3\text{He}} = 1 \times 10^{-29} T^{4.259} n_{^3\text{He}} \tag{2.38}$$

$$R_{sd}^{\text{Rb-N}_2} = 1.3 \times 10^{-25} T^3 n_{\text{N}_2},$$

where each density is given in the unit of cm^{-3} and T is the temperature of the vapor cell in Kelvin. There are two types of collisions between Rb and ^{3}He that destroy Rb spins: spin-destruction collisions and spin-exchange collisions. During spin-exchange collisions, the Rb spin is transferred to the ^{3}He nuclear spin, leaving the Rb atom depolarized. The middle term in Eq (2.38) describes the spin-destruction rate from both mechanisms. At temperature $T = 165$ °C and using $P = 3$ atm for ^{3}He and $P = 50$ torr $= 0.0658$ atm for N_2,

$$R_{sd}^{\text{K-Rb}} = 16 \text{ 1/s}. \tag{2.39}$$

The spin-destruction rate of K-N_2 is given by [33]

$$R_{sd}^{\text{K-N}_2} = 7.0 \times 10^{-26} T^3 n_{\text{N}_2}, \tag{2.40}$$

and using $T = 165$ °C and $P = 50$ torr $= 0.0658$ atm for N_2,

$$R_{sd}^{\text{K-N}_2} = 10 \text{ 1/s}. \tag{2.41}$$

In conclusion, the total spin-destruction rate $R_{sd}^{\text{collisions}} \approx 37$ 1/s.

2.5.3 Spin-exchange between K and He

This section follows the approach to spin-exchange efficiency found in Ref. [20]. The K atoms not only go through spin-destruction collisions, but also spin-exchange collisions

with the nuclear spin of the ^{3}He gas. The efficiency of this spin-exchange between these two species can be defined as [20, 34]

$$\eta \equiv \frac{R_{se}^{\text{K-He}}}{R_{sd}^{\text{K-He}} + R_{se}^{\text{K-He}}}. \tag{2.42}$$

This efficiency η describes the fraction of collisions that result in spin exchange out of all collisions. For the K-^{3}He ensemble, this efficiency was measured to be $\eta = 0.756 - (0.00109\text{K}^{-1})T$, where T is the temperature of the system [34]. Using this, we can figure out what $R_{se}^{\text{K-He}}$ is

$$R_{se}^{\text{K-He}} = \ R_{sd}^{\text{K-He}} \frac{\eta}{1-\eta} \ \simeq 5 \text{ 1/s}. \tag{2.43}$$

The spin-exchange collisions between K and ^{3}He depolarize the K spins. Therefore, $R_{se}^{\text{K-He}} = 5$ 1/s is added to the total relaxation rate R_{Total} for K.

2.6 Estimates

Table 2.2 shows the calculated and literature experimental parameters. For the transverse relaxation time T_2, Eq (2.30) was used. The longitudinal relaxation time T_1 is usually $T_1 \geq 2T_2$ [35]. Therefore, the value of T_1 was calculated to be $T_1 = 2T_2$.

2.6.1 Excitation Rate

For the K magnetometer described here, the beam has a radius of about 0.3 cm and has a power of about 700 μW. Intensity is given as

$$I = \frac{\text{Power}}{\text{Area}} = \frac{1}{2\mu_0 c}\varepsilon^2 \tag{2.44}$$

where μ_0 is the permeability of free space, c is the speed of light, and ε is the amplitude of the electric field. Using Eq (2.44), the amplitude of the electric field ε is calculated to be $\varepsilon = 0.82$ V/cm. Using these values and Eq (2.26), the pumping rate is calculated

Description	Symbol	Estimated Values
Gyromagnetic ratio for K atoms	γ_K	$2\pi \times 28$ Hz/nT
K-K spin-exchange rate	$R_{se}^{K\text{-}K}$	1/30000 1/s
K-^{3}He spin-exchange rate	$R_{se}^{K\text{-}^3He}$	5 1/s
K-K spin-destruction rate	$R_{sd}^{K\text{-}K}$	1.4 1/s
K-^{3}He spin-destruction rate	$R_{sd}^{K\text{-}^3He}$	10 1/s
K-Rb spin-destruction rate	$R_{sd}^{K\text{-}Rb}$	16 1/s
K-N_2 spin-destruction rate	$R_{sd}^{K\text{-}N_2}$	10 1/s
Spin-destruction collision relaxation rate	$R_{sd}^{\text{collisions}}$	37 1/s
K pumping rate	R_{Pump}	260 1/s
Total relaxation rate	R_{Total}	302 1/s
Transverse relaxation time	T_2	3.3 ms
Longitudinal relaxation time	T_1	6.6 ms
Natural K D1 line width	Γ_0	6 MHz
Doppler broadened K D1 line width	$\Gamma_{Doppler}$	470 MHz
Pressure broadened K D1 line width	Γ_{Tot}	39.6 GHz
Pressure broadened absorption cross section	σ_{abs}	1.4×10^{-13} cm^2
K D1 pressure broadened saturation power (with beam radius 0.3 cm)	$P_{S,\text{broadened}}$	3 W
Density of K vapor at 165 °C	n_K	3×10^{13} cm^{-3}
Density of ^{3}He at 165 °C, at 3 atm	n_{He}	8×10^{19} cm^{-3}
Density of N_2 at 165 °C, at 50 torr	n_{N_2}	2×10^{18} cm^{-3}

Table 2.2: Summary of estimated and literature values for experimental parameters.

to be

$$\begin{aligned} R_{Pump} &= \frac{(3 \times 1.3 \text{ MHz/V/cm})^2 (0.82 \text{ V/cm})^2}{39.6 \text{ GHz}} \\ &\simeq 260 \text{ Hz} \end{aligned} \tag{2.45}$$

where $d = 3 \text{ ea}_0 = 3 \times 1.3 \text{ MHz}/(\text{V/cm})$.

2.7 Magnetic Field Dependence of Transmission

Qualitatively, we can think of the K magnetometer system as spin-1/2 system because the hyperfine structure is not resolved due to pressure broadening (see section 2.4). The Hamiltonian describing the interaction between the magnetic moment $\boldsymbol{\mu}$ and magnetic field $\mathbf{B}$ is [36]:

$$\hat{H} = -\hat{\boldsymbol{\mu}} \cdot \mathbf{B}. \tag{2.46}$$

The Hamiltonian for the coupling of the electron spin $\mathbf{S}$ to the magnetic field $\mathbf{B}$ is therefore:

$$\begin{aligned} \hat{H} &= \frac{ge}{2m_e c} \hat{\mathbf{S}} \cdot \mathbf{B} \\ &= \gamma \hat{\mathbf{S}} \cdot \mathbf{B}, \end{aligned} \tag{2.47}$$

where g is the g-factor of the electron ($g = 2.00$), e is the charge of the electron, m_e is the mass of the electron, c is the speed of light, and $\gamma = \frac{ge}{2m_e c}$ is the gyromagnetic ratio of the electron. If $\mathbf{B}$ is only in the z direction, Eq (2.47) reduces to:

$$\hat{H} = \gamma B_0 \hat{S}_z = \omega_0 \hat{S}_z, \tag{2.48}$$

where $\omega_0 = \gamma B_0$. As we can see, in spin 1/2 systems with $\mathbf{B} = B_0 \hat{\mathbf{z}}$, the stationary states for this Hamiltonian are $|+\mathbf{z}\rangle$ and $|-\mathbf{z}\rangle$:

$$\begin{aligned} \hat{H} |+\mathbf{z}\rangle &= \frac{\hbar\omega_0}{2} |+\mathbf{z}\rangle = E_+ |+\mathbf{z}\rangle , \\ \hat{H} |-\mathbf{z}\rangle &= -\frac{\hbar\omega_0}{2} |-\mathbf{z}\rangle = E_- |-\mathbf{z}\rangle . \end{aligned} \tag{2.49}$$

The two energy eigenvalues are: $E_+ = \frac{\hbar\omega_0}{2}$ and $E_- = -\frac{\hbar\omega_0}{2}$. Because the spin of the electron $\mathbf{S}$ points in the opposite direction as the magnetic moment $\boldsymbol{\mu}$, the state with E_+ has spin-up configuration and the state with E_- has spin-down configuration.

The time evolution of a state $|\psi\rangle$ with the Hamiltonian $\hat{H}$ is described by [36]:

$$|\psi(t)\rangle = e^{\frac{-i\hat{H}t}{\hbar}} |\psi(t=0)\rangle . \tag{2.50}$$

In the energy eigenstate $|E\rangle$, Eq (2.50) reduces to:

$$|\psi(t)\rangle = e^{\frac{-i\hat{H}t}{\hbar}} |E\rangle = e^{\frac{-iEt}{\hbar}} |E\rangle , \tag{2.51}$$

where E is the energy eigenvalue for the state $|E\rangle$. In this equation, the term $e^{\frac{-iEt}{\hbar}}$ is just an overall phase and does not have any physical significance. We can see that the energy eigenstate $|E\rangle$ is a stationary state which does not change in time. Any state that is not an energy eigenstate of the Hamiltonian in the system will change in time.

The K atoms that are polarized by circularly polarized light along $+\mathbf{x}$ direction have the wavefunction of $|\psi\rangle = |+\mathbf{x}\rangle$. In the presence of a magnetic field along the perpendicular axis to the $\mathbf{x}$ axis, say $\mathbf{B} = B\hat{\mathbf{z}}$, the state $|+\mathbf{x}\rangle$ is no longer an energy eigenstate, and as a result, the wavefunction would change in time. Classically, the atoms in the $|+\mathbf{x}\rangle$ feel torque from the magnetic field $\mathbf{B} = B\hat{\mathbf{z}}$ and precess about $\mathbf{B}$.

The K spin dynamics in this system can be described using a set of Bloch equations. Discovered by Felix Bloch, the Bloch equations describe the spin evolution of the atomic ensemble in the system using rate equations [37]. The net magnetization of the spins in the system $\mathbf{M}$ can be written as [20, 37, 38]:

$$\frac{d\mathbf{M}}{dt} = \gamma[\mathbf{M} \times \mathbf{B}] - \mathbf{M}R_{Relaxation}, \tag{2.52}$$

where γ is the potassium gyromagnetic ratio and $R_{Relaxation}$ is the corresponding relaxation terms. With the magnetic field $\mathbf{B} = B\hat{\mathbf{z}}$ and with the optical pumping rate term

along the $+\mathbf{x}$ axis, Eq (2.52) becomes:

$$\frac{dM_x}{dt} = \gamma[M_y B_z] - \frac{M_x}{T_2} + R_{Pump},$$

$$\frac{dM_y}{dt} = -\gamma[M_x B_z] - \frac{M_y}{T_2}, \tag{2.53}$$

$$\frac{dM_z}{dt} = \frac{M_z^0 - M_z}{T_1}.$$

where R_{Pump} is the pumping rate, and T_1 and T_2 are the longitudinal relaxation time and transverse relaxation time, respectively. We can solve Eq (2.53) for the steady state solutions, i.e. $\frac{d\mathbf{M}}{dt} = 0$. Figure 2.6 shows the magnetization along the x and y axes, M_x and M_y, as a function of the external magnetic field $\mathbf{B} = B\hat{\mathbf{z}}$ using the expected values for T_1, T_2, and Γ for K atoms from Table 2.2.

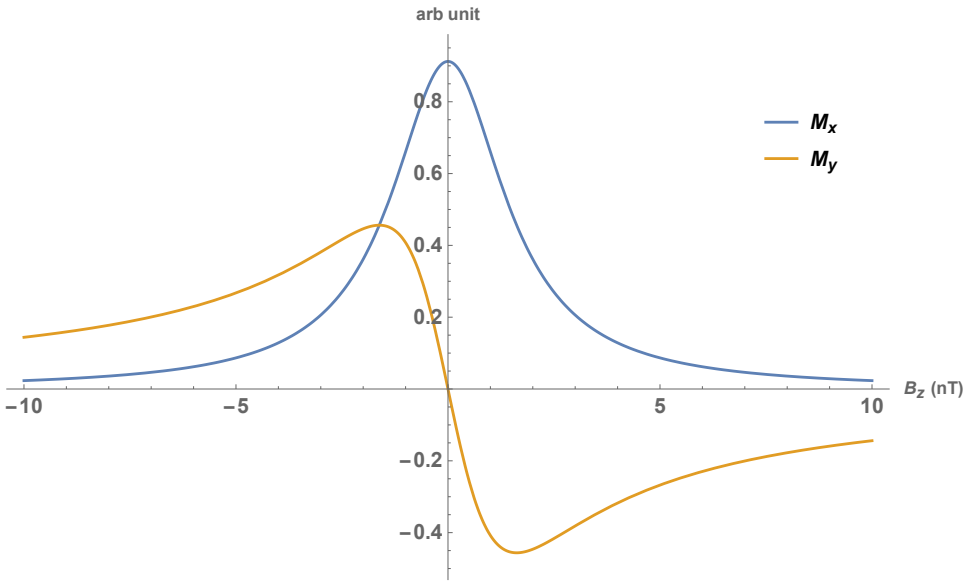

Figure 2.6: The expected M_x and M_y as a function of B_z. B_x and B_y are set to zero. The M_x is showing a magnetic resonance peak, as expected. The estimated values in Table 2.2 were used to generate the plot.

As shown in Figure 2.6, the magnetic resonance of B_z shows a peak around $B_z = 0$. Since we are monitoring the K laser beam along the **x**-axis, M_x reflects the transmission signal through the vapor cell. In the absence of a magnetic field along the **z**-axis (and assuming $B_y = 0$), all the atoms are in the dark state and the transmission signal is maximized. As we have some magnetic field along the **z**-axis, the state $|+\mathbf{x}\rangle$ is no longer an energy eigenstate, and the atoms evolve in time, enabling them to re-absorb light. As B_z is increased, the atoms precess much faster than the pumping rate. Therefore, they have no component in the **x** direction.

In the presence of a magnetic field along the **x**-axis, the magnetization along the **x**-axis shows a different behavior. If all the fields are perfectly zeroed, we would expect all the atoms to be in the dark state, and varying B_x does not change the state. However, in the presence of some magnetic fields along the perdendicular axes, we would expect to see a "dip" in the M_x. In the case where $B_x = 0$ but $B_z, B_y \neq 0$, the atoms that have been optically pumped into the dark state by the circular light precess out of the dark state. This causes the transmission signal to decrease as the atoms not in the dark state can absorb photons. As we increase B_x, atoms precess about the net magnetic field. As B_x gets larger and larger compared to B_y and B_z, the net magnetic field would be closer and closer to the **x**-axis. If we say this net magnetization has a state $|+\mathbf{n}\rangle$, the x-component of this state is [36]

$$|+\mathbf{n}\rangle = \cos\frac{\theta}{2}\,|+\mathbf{x}\rangle + \sin\frac{\theta}{2}\,|-\mathbf{x}\rangle\,, \tag{2.54}$$

where θ is the angle between the $+\mathbf{n}$ and $+\mathbf{x}$ axes. As the angle θ decreases, the state has a bigger and bigger $+\mathbf{x}$ component. Therefore, we expect the projection of this state onto the $+\mathbf{x}$ to increase as B_x is increased.

If we apply a magnetic field along the pumping axis, the **x** axis, Eq (2.52) becomes

$$\frac{dM_x}{dt} = \gamma[M_y B_z - M_z B_y] - \frac{M_x}{T_1} + R_{Pump},$$

$$\frac{dM_y}{dt} = -\gamma[M_x B_z - M_z B_x] - \frac{M_y}{T_2}, \tag{2.55}$$

$$\frac{dM_z}{dt} = \gamma[M_y B_z - M_z B_y] - \frac{M_z}{T_2}.$$

Here, I have left the terms B_y and B_z in the equations. Figure 2.7 shows the plot of M_x as a function of the external magnetic field $\mathbf{B} = B\hat{\mathbf{x}}$ with different values of some residual magnetic field along the y and z axes. As we can see in Figure 2.7, when there

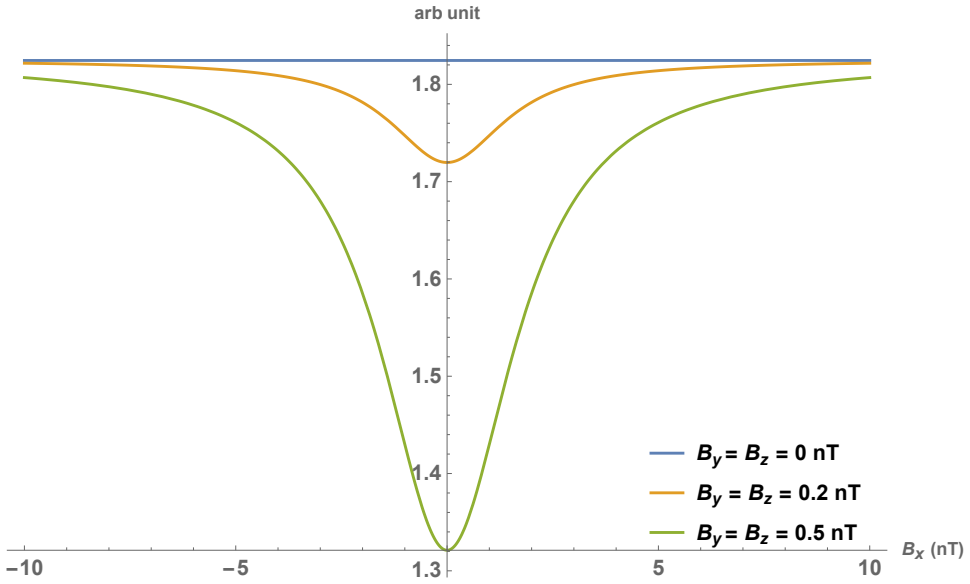

Figure 2.7: M_x as a function of B_x at different values of residual fields along the y and z axes. In the presence of transverse residual fields, the M_x shows a "dip", as expected. The estimated values in Table 2.2 were used to generate the plot.

are no residual magnetic fields along the y and z axes, the M_x is a constant. In the

presence of some residual fields along the y and z axes, the M_x has a "dip", and the width of this dip broadens as the residual fields increase.

The magnetic resonance also depends on the pumping rate R_{Pump} and the relaxation times T_1 and T_2. Figure 2.8 shows the plot of M_x as a function of the external magnetic field $\mathbf{B} = B\hat{\mathbf{z}}$ for three different pumping rate 260 Hz, 500 Hz, and 1000Hz. As we can see in Figure 2.8, higher pumping rate results in a larger amplitude. This is to be expected because the polarization increases with higher pumping rate. As a result, more K atoms are put into the dark state, and at $B_z = 0$, the transmitted light through the vapor cell is increased. Since the pressure broadening is so much larger than the power broadening, the widths remain the same for all pumping rates.

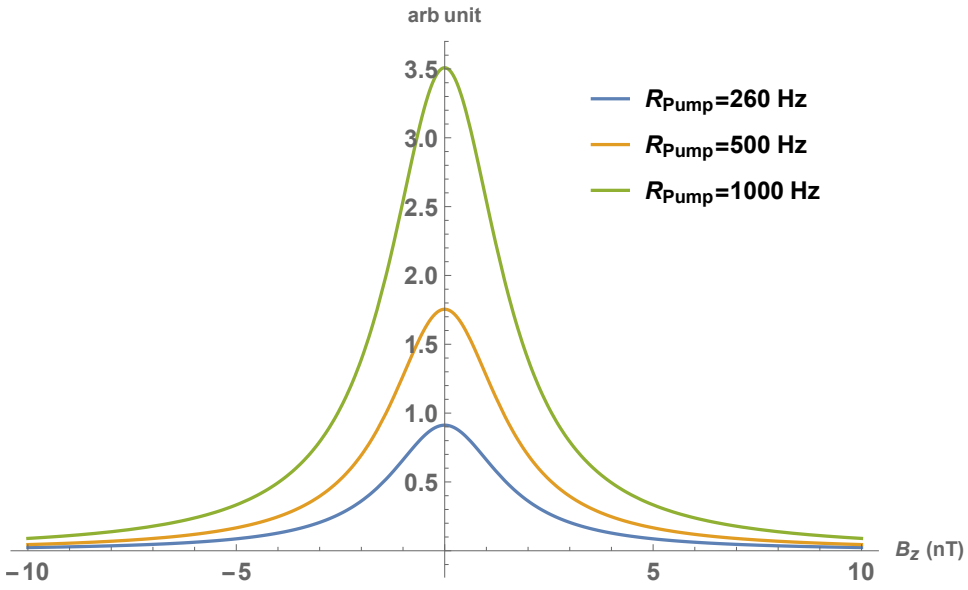

Figure 2.8: M_x as a function of B_z at different values of pumping rate. As pumping rate is increased, the amplitude of the peak is also increased and the width remains the same, as expected. The estimated values in Table 2.2 were used to generate the plot.

Figure 2.9 shows the plot of M_x as a function of the external magnetic field $\mathbf{B} = B\hat{\mathbf{z}}$ for three different T_2 values 3.5 ms, 7 ms, and 10 ms. Figure 2.9 suggests that higher T_2 value results in a narrower, taller peak. This is to be expected because as T_2 value is increased, we expect the spins to be coherent for a longer time, resulting in a narrower,

taller peak. The width of the magnetic resonance δB is related to the T_2 by [28]

$$\delta B = (2\pi Q T_2 \mu_0)^{-1}, \tag{2.56}$$

where μ_0 is the permeability of free space and Q is the slowing-down factor described earlier.

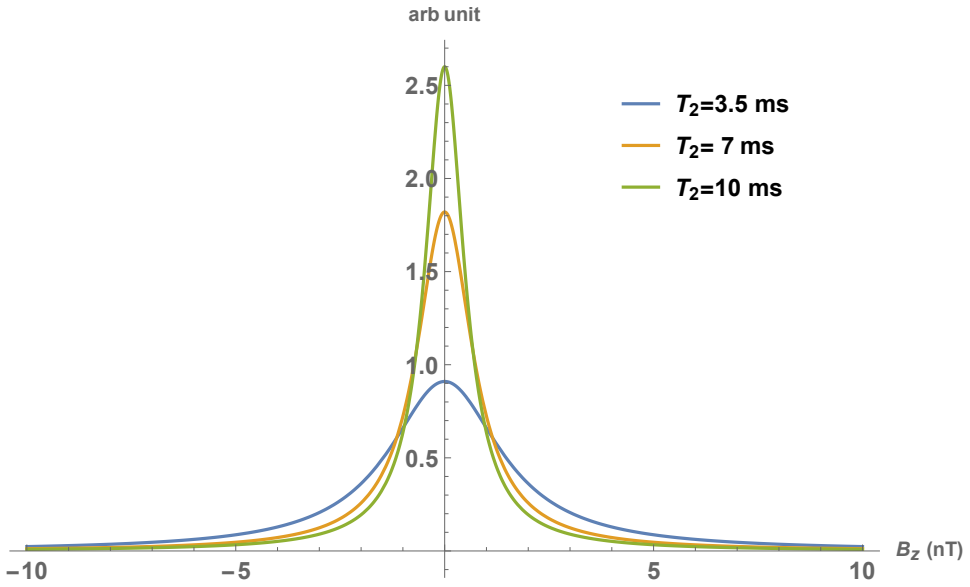

Figure 2.9: M_x as a function of B_z at different values of T_2 times. As T_2 time is increased, the width of the peak gets narrower, as expected. The estimated values in Table 2.2 were used to generate the plot.

2.8 Fundamental Magnetometer Sensitivity

The fundamental sensitivity of a magnetometer due to shot-noise is given by [28]

$$\delta B = \frac{1}{\gamma\sqrt{nT_2Vt}} \tag{2.57}$$

where γ is the K atom gyromagnetic ratio, n is the density of atoms, T_2 is the transverse spin relaxation time, V is the volume of the beam light inside the vapor cell, and t is the

measurement time. The beam is about 0.3 cm in radius. The depth of the vapor cell is about 1 cm. Therefore, the volume $V = \pi(0.3)^2 1$ cm^3 = 0.085 cm^3. The bandwidth of the magnetometer is around 100 Hz; therefore the value of t is $t = \frac{1}{2\pi 100}$ s. Using estimated values from Table 2.2, the fundamental magnetometer sensitivity is calculated to be $\delta B = 1.5$ fT$/\sqrt{\text{Hz}}$.

Chapter 3

Experimental Setup

3.1 K Magnetometer

The magnetometer is a single-beam, spin-exchange-relaxation-free (SERF) magnetometer using potassium (K) atoms. The vapor cell contains K atoms, and helium (^{3}He) buffer gas, and N_2 as quenching gas. It also contains rubidium (Rb) for the second generation magnetometer. The vapor cell is housed within four magnetic shields to reduce any external magnetic fields. Circularly polarized light, resonant with the K D1 transition (770 nm), optically pumps the atoms into a dark state, leading to increased transmission of the light through the cell. In the presence of a magnetic field, the atoms will precess into a bright state, resulting in reduced transmission. We apply currents through the coils inside the shields to compensate residual magnetization of the shields and create a region of zero magnetic field. We monitor the transmission and adjust the current to maintain the zero magnetic field. The amount of current needed to zero the magnetic field inside the shields provides a measurement of the residual magnetic field. The schematic of the magnetometer is shown in Figure 3.1.

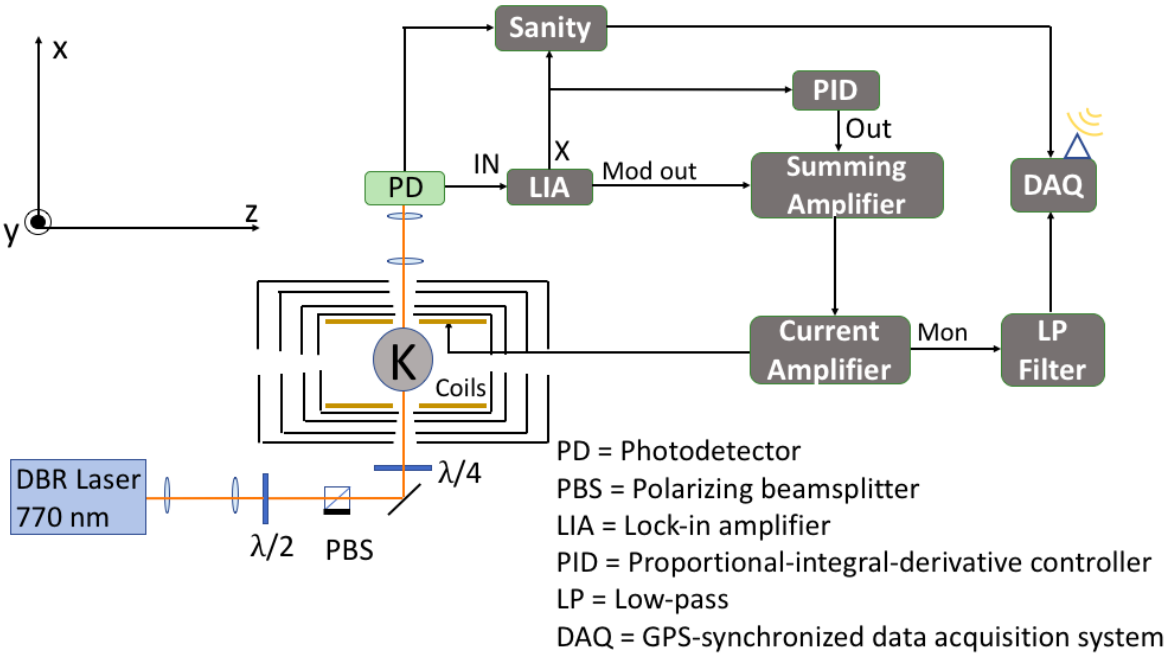

Figure 3.1: Schematic of the magnetometer. The magnetometer uses K atoms in the vapor cell that is housed in the four layered magnetic shields. The magnetometer operates in the zero magnetic field environment. The magnetic coils are inside the shields to provide control over the internal magnetic field. The DBR laser is tuned to the K D1 transition and is used to probe and pump the K atoms. The laser is circularly polarized by the quarter waveplate and is directed onto the PD. The PD signal (the transmission signal) is modulated by modulating the B field along the **z**-axis for lock-in detection. The lock-in amplifier takes in the transmission signal as the input and outputs the error signal that goes into the PID. The PID provides negative feedback that controls the current source to maintain zero magnetic field. The monitor output of the current source goes through a low-pass filter. The output of the low-pass filter is recorded as magnetic field measurements in the DAQ with GPS timestamps. The setup also includes a sanity box which has an external magnetometer, accelerometer, and a thermometer. The sanity box also monitors the PD, lock-in, and the current source outputs–if a signal falls out of a specific range, the sanity box flags the data as "insane".

3.1.1 Probe/Pump Beam

The K magnetometer uses a single beam for both pumping and probing of K atoms. The probe/pump beam is generated by a DBR laser (Photodigm PH770DBR040T8) resonant with the K D1 transition at 770 nm and is free-running. The current and temperature of the diode are controlled with a current controller (ILX Lightwave LDX-3207B Precession Current Source) and a temperature controller (ILX Lightwave LDT-5525), respectively. A quarter waveplate, $\lambda/4$, is placed just before the magnetic shields and circularly polarizes the light entering the cell.

3.1.2 Vapor Cell

The K atoms are contained in the vapor cell, shown in Figure 3.2a, was manufactured by TwinLeaf LLC; it is about 1 cm diameter and contains hybrid rubdium-potassium in a 10:90 ratio, 50 torr of N_2 as quenching gas, and 3 atm ($\sim$2300 torr) of ^{3}He as buffer gas. This combination of atoms was chosen for the future generation magnetometer which is explained in Chapter 5. The buffer gas reduces depolarization of the K atoms resulting from the collisions with the glass walls of the cell by increasing the diffusion time. The vapor cell is inside a resistively heated oven enclosed in a Teflon housing with glass window and is shown in Figure 3.2b. The temperature of the vapor cell is controlled by a TwinLeaf heater driver and by a LabView program. The heating of the oven is done at 50 kHz, which is much faster than the bandwidth of the magnetometer. Therefore, any magnetic fields induced by the heater are not detected.

3.1.3 Magnetic Shields and Coils

Figure 3.3 shows the four layered magnetic shields (MS1) manufactured by TwinLeaf LLC. The vapor cell is housed within these magnetic shields to reduce magnetic background noise. The internal magnetic field coils provide control of the field components B_x, B_y, and B_z, five first-order gradients dB_z/dz, dB_y/dy, dB_z/dx, dB_y/dx, and dB_z/dy, and one second-order gradient d^2B_z/dz^2. The nine magnetic coils provide complete

(a) The vapor cell used in the experiment. It is spherical, with an inner diameter is about 1 cm.

(b) The resistive Teflon oven (TwinLeaf LLC) containing the vapor cell.

Figure 3.2: The vapor cell (a) and the oven (b) that houses the vapor cell.

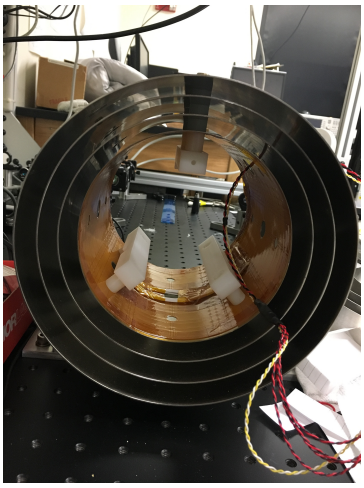

(a)

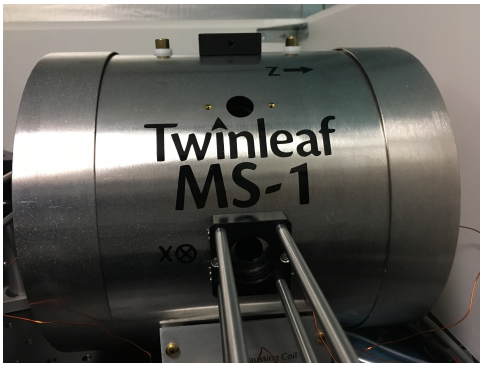

(b)

Figure 3.3: The side view (a) and the front view (b) of the four layered magnetic shields. The shields house the vapor cell and are used to reduce magnetic background noise. There are 9 sets of coils in the shields to provide control over the internal magnetic field. The shields provide a shielding factor of 10^6.

control over the magnetic field inside the shields and first order gradients. Maxwell's equation for the divergence of a magnetic field is [39]

$$\begin{aligned} \nabla \cdot \mathbf{B} &= 0 \\ \frac{\partial B_x}{\partial x} + \frac{\partial B_y}{\partial y} + \frac{\partial B_z}{\partial z} &= 0. \end{aligned} \tag{3.1}$$

Eq (3.1) suggests that if we have control over dB_z/dz and dB_y/dy, we also have control over dB_x/dx. Similarly, the curl of a magnetic field is described by [39]

$$\begin{aligned} \nabla \times \mathbf{B} &= \mu_0 \mathbf{J}, \\ &= \left(\frac{\partial B_z}{\partial y} - \frac{\partial B_y}{\partial z} \right) \hat{\mathbf{x}} + \left(\frac{\partial B_x}{\partial z} - \frac{\partial B_z}{\partial x} \right) \hat{\mathbf{y}} + \left(\frac{\partial B_y}{\partial x} - \frac{\partial B_x}{\partial y} \right) \hat{\mathbf{z}}, \end{aligned} \tag{3.2}$$

where μ_0 is the permeability of free space and $\mathbf{J}$ is the electric current density. Equation (3.2) suggests that if we can control $dB_z/dx, dB_y/dx$, and dB_z/dy, we have full control over the first-order gradients of the magnetic field.

The field B_z is supplied by a voltage controlled current source (SRS CS580). The fields B_x and B_y are controlled by the TwinLeaf CSB low-noise current supply. The remaining fields are controlled by a homemade low-noise current supply. The schematic of the current supply is included in the appendix.

To isolate the system better, the whole apparatus is enclosed inside insulation foams as shown in Figure 3.4.

3.1.4 Detection

The quarter waveplate just before the vapor cell circularly polarizes the beam in the $\mathbf{x}$ direction. The beam radius is about 0.3 cm and has power of about 700 μW. The beam travels through the center of the vapor cell and is directed onto a photodetector (Thorlabs PDA36A). The circularly polarized light optically pumps the K atoms into a dark state along the $+\mathbf{x}$ direction as discussed in section 2.4. In the presence of a magnetic field orthogonal to the polarized axis, the atoms come out of the dark state resulting in decreased transmission. A change in transmission indicates a magnetic field

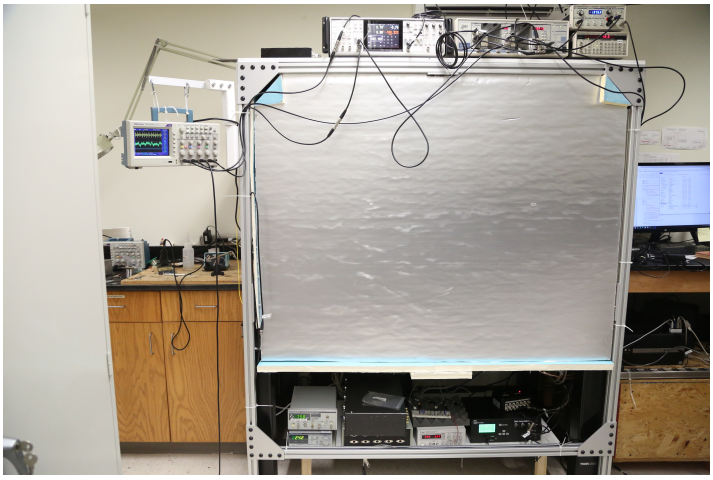

Figure 3.4: Insulation was installed to isolate the system from factors such as external temperature. This will be discussed in more detail in section 4.9.

along the **y** or the **z** directions. A small change in the magnetic field can be detected using a lock-in amplifier. The transmission signal from the photodetector is modulated at 763 Hz with 1.5-nT rms amplitude along the **z** direction. The modulated signal is detected by a lock-in amplifier (SRS SR860). The output of the lock-in amplifier is sent to a proportional-integral-differential (PID) controller (SRS SIM960) to provide negative feedback. The feedback signal is summed with the modulation signal by a summing amplifier (SRS SIM980). The output of the summing amplifier is sent to a voltage-controlled current source (SRS CS580), which provides current to the B_z coils. The current applied to the coils is filtered with a Butterworth low-pass filter (SRS SIM965) with a cutoff frequency at 100 Hz and 48 dB/oct slope to obtain a bandwidth around 100 Hz.

We monitor the current that is applied to compensate for the change in the magnetic field along the **z**-axis. Therefore, an increase of the magnetic field in the $-\mathbf{z}$ direction will correspond to an increase in the current applied to the coils. The sensitive axis of the magnetometer is in the $-\mathbf{z}$ direction, which has an azimuth of 300° relative to North.

3.1.5 Data Acquisition

The signals from the current source, the photodetector, and the lock-in amplifier are sent to the data acquisition box (DAQ), built by the GNOME collaborator in Krakow, Poland. The DAQ which records data at a sampling rate of 512 Hz with GPS timestamps and uploads them onto the GNOME server in Mainz, Germany. The sanity box, made by the GNOME collaborator in Fribourg, Switzerland, is a device located near the magnetometer. It has an accelerometer and a thermometer. It also takes the photodetector signal and the lock-in signal as inputs. When any signal is out of the established range, it flags the data as "insane".

3.2 Calibrating magnetic fields

The magnetometer monitors the current applied to the magnetic coils in the feedback. For the calibration between the current and the magnetic field, we placed flux-gate magnetometers along the $\mathbf{x}, \mathbf{y}$, and $\mathbf{z}$ directions and measured the induced magnetic field as a function of the applied current. Figure 3.5 shows the plots for the calibrations of the $\mathbf{x}, \mathbf{y}$, and $\mathbf{z}$ directions. A linear regression analysis was carried out for each direction. The calibrations between the applied current and the induced magnetic field along the $\mathbf{x}, \mathbf{y}$, and $\mathbf{z}$ directions are:

$$\begin{aligned} B_x[\mathrm{nT}] &= 65.68(2)\ [\mathrm{nT/mA}] * I_x[\mathrm{mA}] - 16.35(4)\ [\mathrm{nT}], \\ B_y[\mathrm{nT}] &= 65.571(3)\ [\mathrm{nT/mA}] * I_y[\mathrm{mA}] - 92.72(2)\ [\mathrm{nT}], \\ B_z[\mathrm{nT}] &= 92.60(1)\ [\mathrm{nT/mA}] * I_z[\mathrm{mA}] - 59.81(4)\ [\mathrm{nT}]. \end{aligned} \tag{3.3}$$

Using Eq (3.3), the currents through the magnetic coils are converted into magnetic field measurements.

3.3 Additional $\mathbf{B}_Z$ Coils

The magnetometer operates by monitoring the current applied to the B_z coils to compensate any magnetic field change inside the shields. If the same B_z coils were used

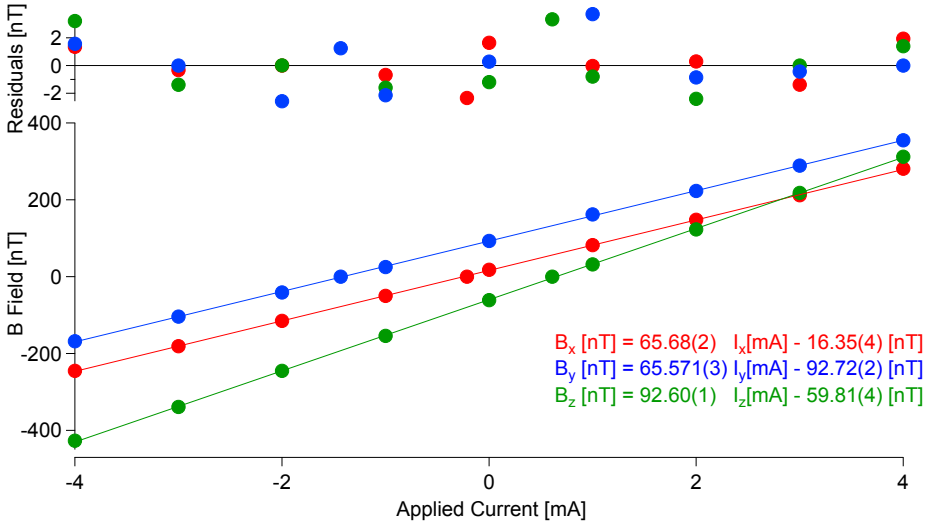

Figure 3.5: Calibration curve of magnetic field and current of the coils inside the shields along the **x**, **y**, and **z** axes. For each axis, the current was applied to the coils, and the induced magnetic field was measured with flux-gate magnetometers. Linear regressions were performed to calculate the slopes.

both to apply a test pulse or sinusoidal wave *and* to monitor the compensating magnetic field, they would cancel each other out. This would result in no change in the magnetic field measurement. Therefore, a second set of B_z coils is required to apply a test pulse or to measure the bandwidth of the magnetometer. We made a set of B_z coils using copper wire. A piece of poster board was shaped into a cylinder with a diameter of about 15 cm. Three holes of about 1-inch diameter were cut to line up with the windows of the oven. The copper wire was looped around the paper cylinder. Five turns were looped around the cylinder with about an inch of separation between each turn. The coils were placed inside the innermost magnetic shield. According to Ampere's law for the magnetic field generated inside a solenoid is [39],

$$B = \mu_0 n i = \mu_0 \frac{N}{L} i, \tag{3.4}$$

where μ_0 is the permeability of free space, $n = N/L$ is the number of turns per unit length, and i is the current. Using $L = 5$ inch and $N = 5$ turns, the value $B/i = 49$ nT/mA.

The coils were connected to a power supply in series with a 30 kΩ resistor (1 % precision). The coils were calibrated by applying voltage and measuring the resulting magnetic field along the **z** axis with a Gauss meter. Fig 3.6 shows the calibration curve

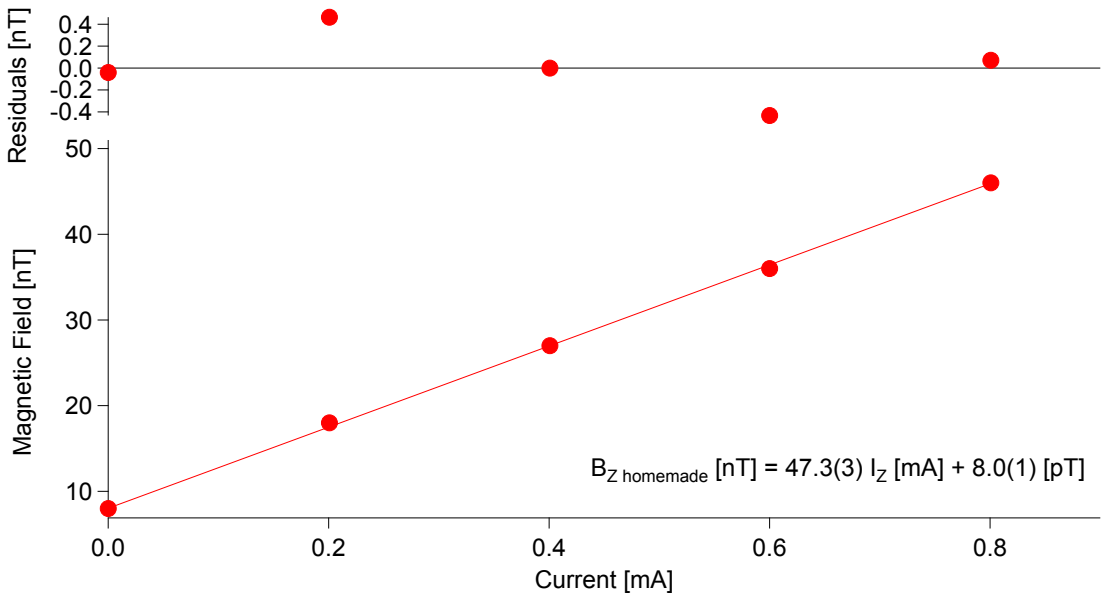

Figure 3.6: Calibration curve of magnetic field and current of the homemade B_z coils. The homemade coils were connected to a power source in series with a 30 kΩ resistor. Voltage was applied to the coils, and the induced magnetic field was measured with a Gauss meter. A linear regression was performed to calculate the slope shown in the figure.

for the homemade B_z coils. A linear regression was carried out (the last point was excluded) and gave a slope of

$$B_z[\mathrm{nT}] = 47.3(3)[\mathrm{nT/mA}] * I_z[\mathrm{mA}], \tag{3.5}$$

which is in good agreement with the calculated value from Eq (3.4).

Chapter 4

Characterization of the Magnetometer

4.1 Linear and Circular polarization

As mentioned in section 2.4, the circularly polarized light optically pumps the atoms into the dark state. Once they are in the dark state, they cannot absorb photons anymore, resulting in increased transmission. On the other hand, if the light was linearly polarized, the atoms can absorb the light until they reach the saturation point described in section 2.3.6. Figure 4.1 shows the fractional transmission through the cell as a function of laser power for both linearly (open blue) and circularly (filled red) polarized light. For both measurements, the beam radius was about 0.3 cm. Figure 4.1 shows that for the linearly polarized light, the fractional transmission does not change as the laser power is increased up to ~ 700 μW. This makes sense because 700 μW is still below the saturation power for the pressure broadened transition; therefore, the atoms continue to absorb more photons as the laser power is increased. On the other hand, for the circularly polarized light, the fractional transmission increases as the laser power increases. This is consistent with the expected result; in the system, the pumping rate competes with the relaxation processes described in section 2.5. As the laser power is increased, the pumping rate is increased, and as a result more atoms are put into the

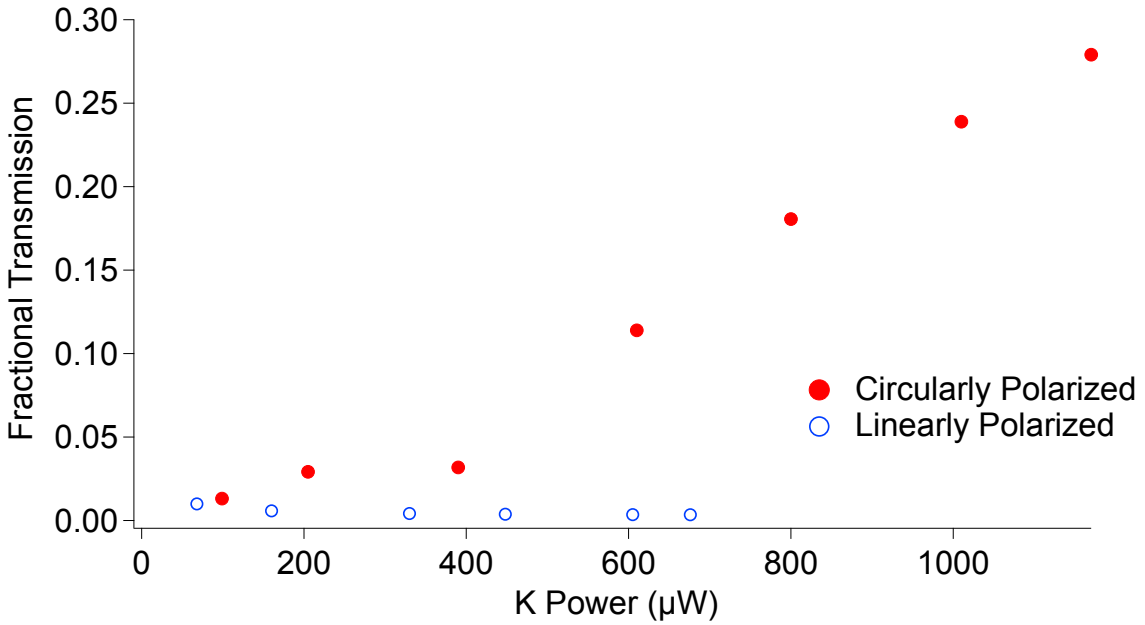

Figure 4.1: The fractional transmission as a function of laser power for the linearly (open blue) and circularly (filled red) polarized light. As the laser power is increased, the fractional transmission remains constant for the linear polarization but increases for the circular polarization, which is expected.

dark state. Therefore, the fractional transmission is expected to increase with higher laser power.

4.2 K Absorption

The line shape of the broadened spectral line is described by Eq (2.24). The width of the spectral line depends on the number of atoms, and consequently on the temperature of the vapor cell. Figure 4.2 shows the absorption spectral line of the K D1 transition through the vapor cell at three different temperatures: 100°C, 120°C, and 150°C. The probe laser was linearly polarized and was set at a low intensity ($\sim$ 5 μW) to avoid saturation. The wavelength of the laser was controlled by changing the temperature of the diode, and the current was kept constant. At each temperature, the wavelength of

the laser was measured using a wavemeter and the transmission signal was recorded. We

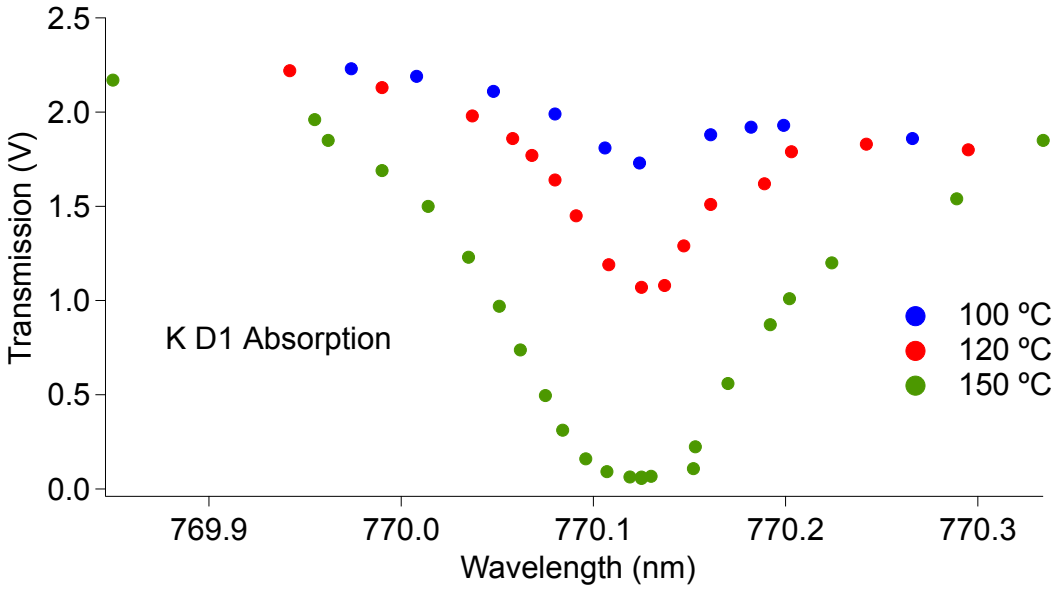

Figure 4.2: The absorption spectral line of the K D1 transmission through the vapor cell at three different temperatures. As expected, both the width and depth of the absorption increases with the K vapor density in the vapor cell, and thus with the temperature (see Eq (2.19)). The wavelength of the laser is increased by increasing the temperature of the diode. The laser power decreases as the diode temperature increases, which leads to data points taken at higher wavelengths having lower transmission signal, even when absorption is not taken into account.

can see that as the temperature increases, the width and the depth of the spectral line increase. Moving away from the point of minimum transmission (maximum absorption), the transmission increases more slowly as the wavelength is increased than it does as the wavelength is decreased. This is due to the decrease in the laser power as the temperature is increased to produce longer wavelengths.

To account for the laser power variation with temperature, we measured the power of the laser at the rejection port of the polarizing beamsplitter with a homemade photodetector. Figure 4.3 shows the fractional transmission of the laser beam as a function of frequency. The vapor cell was set at 165 °C. The data in the figure were

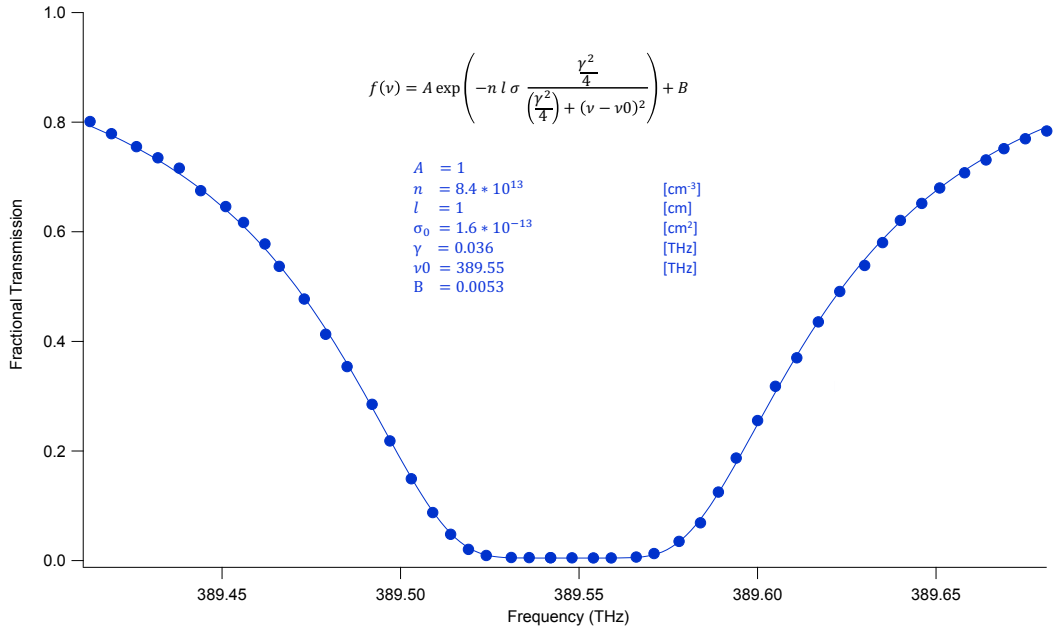

Figure 4.3: The fractional transmission as a function of frequency for the K D1 absorption. The temperature of the vapor cell was set at 165 °C. The absorption line was fitted to Eq (2.19). The K vapor density from the fit is $n_{\mathrm{K}} = 8.4 \times 10^{13}$ cm^{-3}, which suggests that the actual vapor cell temperature is about 185 °C.

normalized using the relation between the temperature and the laser power. Figure 4.3 was fitted to Eq (2.19). The fit suggests that the density of potassium vapor is $n_{\mathrm{K}} = 8.4 \times 10^{13}$ cm^{-3}. This value disagrees with the potassium vapor density at 165 °C, $n_{\mathrm{K},165\ ^\circ C} = 2.2 \times 10^{13}$ cm^{-3}, that was calculated using Eq (2.25). Using the n_{K} from the fit and Eq (2.25), we calculate the actual temperature of the vapor cell to be $T \approx 185$ °C. The discrepancy between the set temperature and the actual temperature may come from the LabView temperature control program. After connecting the oven to the computer, calibration is required. This calibration assumes whatever the tem-

perature is at that time to be 20 °C. We conclude that when calibrating the program, the cell was not completely at room temperature. Therefore, the temperature 165 °C on the LabView program corresponds to the actual temperature $T \approx 185$ °C.

The fit in Figure 4.3 suggests that the pressure broadened absorption cross section is $\sigma = 1.6 \times 10^{-13}$ cm^2.

4.2.1 K Absorption with Linear and Circular light

Circularly polarized light optically pumps the K atoms into the dark state. When comparing the absorption of circularly polarized and linearly polarized light, we would expect that the circular light would be absorbed less than the linear light under the same conditions. Figure 4.4 shows the absorption spectral line for the K D1 transition with both linearly and circularly polarized light. A large leading field in the **x**-axis was applied to ensure that the absorption is due to the polarization of the light and not because of the non-zero transverse magnetic field components.

As we see in Figure 4.4, the absorption for the circularly polarized light dips less and is narrower. This is to be expected because as the circularly polarized light optically pumps the atoms into the dark state, more light is transmitted through the vapor cell.

4.3 Magnetic Resonance

As described in section 2.4, the circularly polarized light optically pumps the K atoms into the dark state, $M_x = +1/2$ as shown in Figure 2.3. When the atoms are in the dark state along the **x** direction, the transmission signal is maximized because atoms in the dark state cannot absorb photons. In the presence of a magnetic field perpendicular to the polarizing axis **x**, the atoms feel torque and precess out of the dark state. In Figure 4.5, the magnetization **M** represents the net magnetization of the atoms, and it is along the $+\mathbf{x}$ direction because the atoms are polarized by the circularly polarized light **k**. When the perpendicular magnetic field B_z is introduced, the atoms experience torque and precess out of the $M_x = +1/2$ state as denoted by ω in Figure 4.5. Once

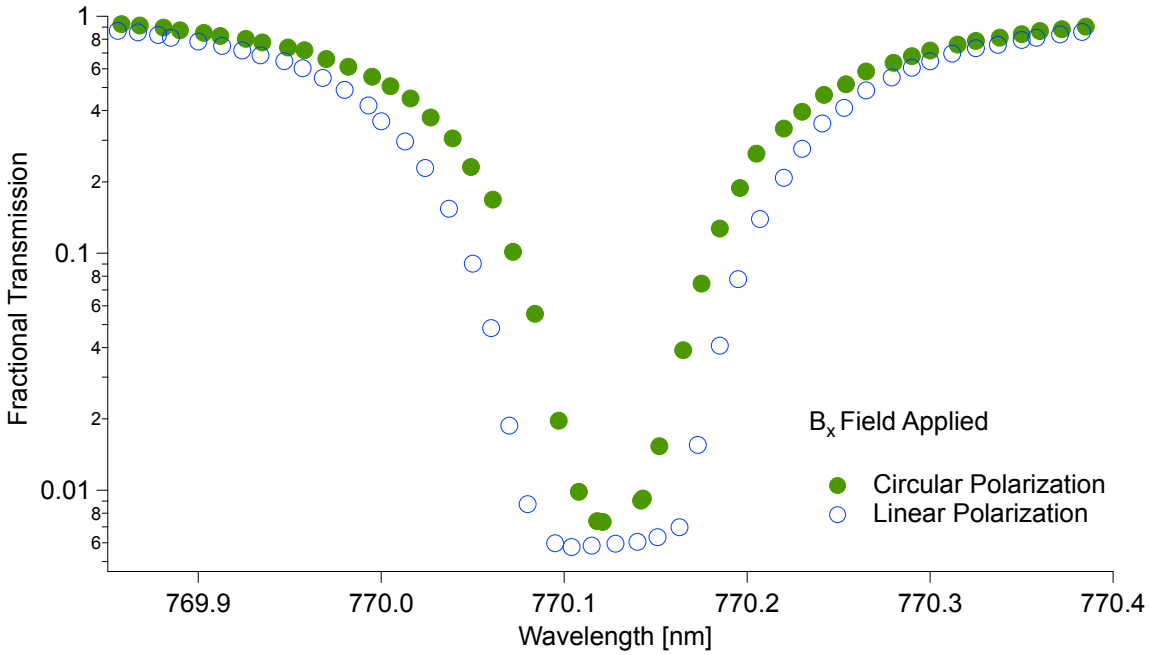

Figure 4.4: Fractional transmission as a function of frequency for the K D1 transition for linearly polarized light (open blue) and circularly polarized light (filled green). A large B_x leading field was applied. The power of the laser for both measurements was around 5 μW. The absorption dips less and is narrower for the circularly polarized light, as expected.

they are out of the dark state, the atoms can absorb photons again, and as a result the transmission signal decreases.

Figure 4.6 shows the transmission signal of the K atoms through the vapor cell as B_z is scanned. Note that since the transmission through the vapor cell is along the $+\mathbf{x}$ direction, the transmission signal reflects M_x. The profile in Figure 4.6 is in good agreement with the M_x in Figure 2.6, which was generated by using a set of Bloch equations. When there is no external magnetization $\mathbf{B} = \mathbf{0}$, all the atoms will stay in the dark state, leading to a maximum in the transmission signal. As $|B_z|$ increases, the transmission signal decreases because the atoms absorb photons again. B_z is modulated by the lock-in amplifier. This transmission signal is sent to the lock-in amplifier. Figure 4.7 shows the output of the lock-in signal which is used as an error

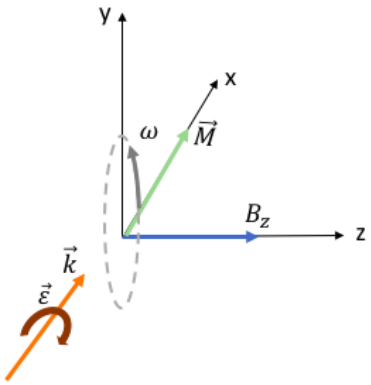

Figure 4.5: Cartoon showing the precession of the magnetization **M**. The circularly polarized light **k** polarizes the net magnetization **M** is along the +**x** direction, the dark state. In the presence of the magnetic field B_z, the magnetization feels torque and precesses out of the dark state, as denoted by ω.

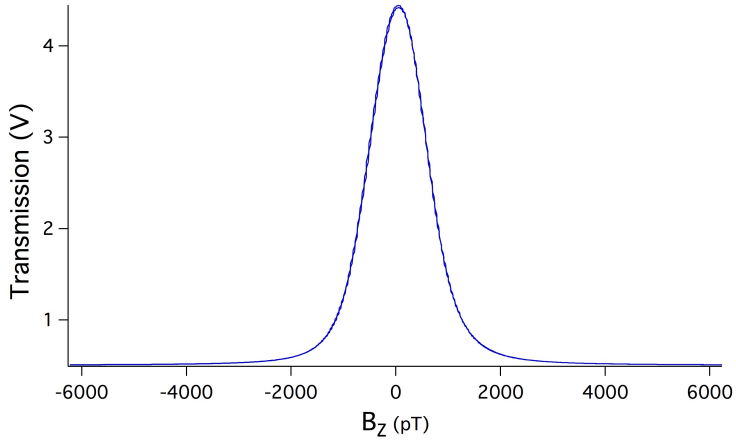

Figure 4.6: Transmission of the K atoms as B_z is scanned. At $B_z = 0$, the transmission is maximized as the atoms are pumped into the dark state. In the presence of B_z, the atoms precess out of the dark state resulting in reduced transmission.

signal for the PID.

As we saw in section 2.7, the fundamental width of this magnetic resonance depends on T_1 and T_2. In practice, the width of the resonance is limited by how close to zero the fields are. In Figure 4.6, the width is estimated to be $\delta B \sim 1000$ pT. Using Eq (2.56),

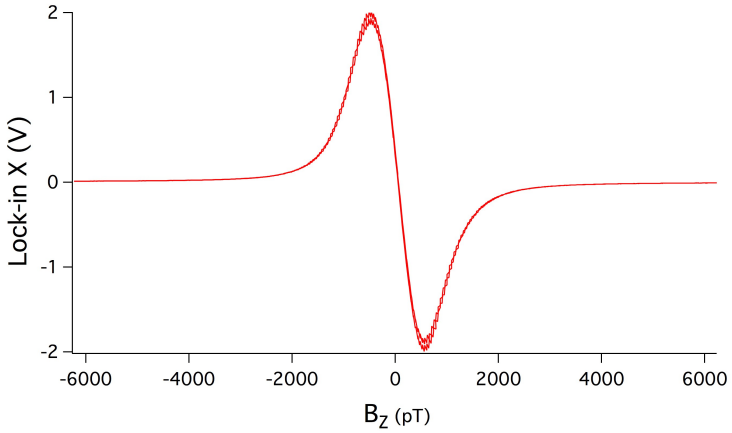

Figure 4.7: The error signal from the output of the lock-in amplifier. The magnetic field along the **z** direction is kept at zero, and the amount of current applied to B_z coils is monitored and calibrated into the magnetic field.

we can estimate the T_2 from the width of the resonance. The value of T_2 is estimated to be $T_2 \sim 3$ ms, which agrees with the estimated T_2. Table 4.1 shows the estimated values and the measured values of the experimental parameters.

In the following sections, we describe the effect on the magnetic resonance of applied field, i.e. different values of residual fields inside the shields, to examine how each component of the residual field affects the magnetic resonance.

Parameter	Estimated Value	Measured Value
Γ_{Tot}	39.6 GHz	36 GHz
σ_{abs}	1.4×10^{-13} cm^2	1.6×10^{-13} cm^2
n_K (at actual temperature 185 °C)		8.4×10^{13} cm^{-3}
T_2	3.3 ms	3 ms

Table 4.1: Comparison of the estimated experimental parameters from Chapter 2 and measured experimental parameters.

4.3.1 Dependence on Gradients

This section investigates how the first-order gradients ($dB_z/dz, dB_y/dy, dB_z/dx, dB_y/dx$, and dB_z/dy) and the second-order gradient (d^2B_z/dz^2) affect the amplitude and the width of the magnetic resonance. Figure 4.8 shows the magnetic resonance as B_z is scanned with different applied currents for dB_z/dz, dB_y/dy, dB_z/dy, dB_z/dx, and dB_y/dx, respectively. The current through each coil was applied using the TwinLeaf CSB low-noise current supply.

Figures 4.8 shows that the amplitude and the width of the magnetic resonance change with different values of applied current through each set of gradient coils. For each gradient, the current value which maximizes the amplitude and minimizes the width of the magnetic resonance generates the magnetic field that cancels out the residual field present in the shields and therefore is used.

4.3.2 Dependence on B_y

In this section, the effect of B_y is investigated. Figure 4.9 shows the amplitude of the magnetic resonance as a function of B_x for the two values of B_y, $B_y = -53$ nT and $B_y = -13$ nT. For all the points, B_z was kept constant at -0.38 nT. According to Figure 4.9, the magnetic resonance M_x shows a "dip" as B_x is scanned. The profile in Figure 4.9 agrees well with Figure 2.7 and suggests that the perpendicular components B_y and B_z of the residual magnetic field are non zero. At some value of applied B_x (in this figure, when $B_x \approx -80$ nT), the residual B_x is minimized, resulting in a minimum in the transmission signal because the atoms precess out of the dark state due to the perpendicular magnetic field components. As mentioned in section 2.7, in the presence of larger $|B_x|$, the angle between the net magnetic field inside the shields and the $+\mathbf{x}$ axis gets smaller and smaller, and the atoms precess about this new axis, whose largest component is the x component, and the atoms are "held" in the dark state.

The width of the "dip" is affected by the perpendicular components of the residual field. Since B_z was constant, Figure 4.9 suggests that $B_y = -13$ nT results in a smaller residual B_y field because the "dip" is narrower.

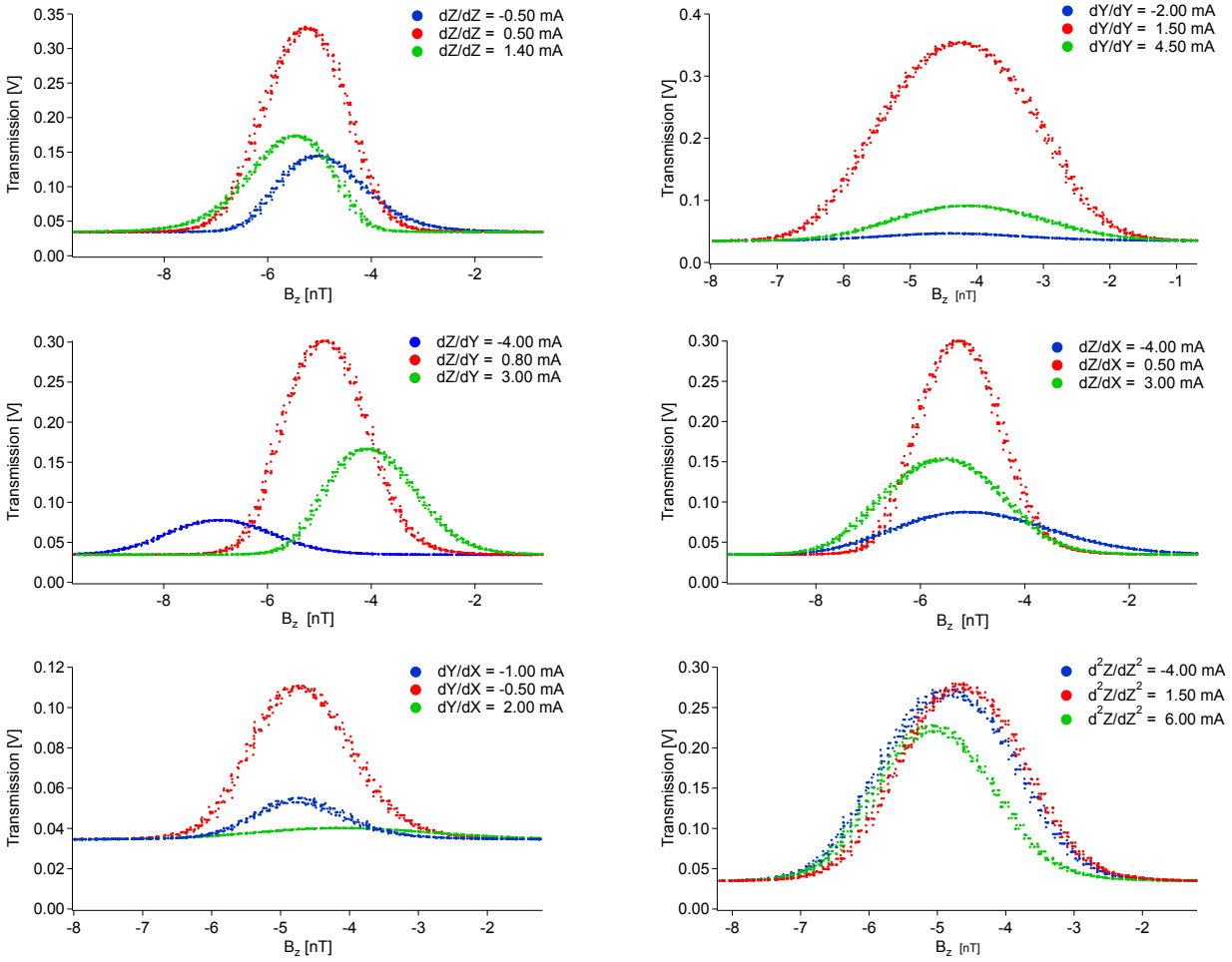

Figure 4.8: The magnetic resonances of the K atoms as B_z is scanned. From left to right and top to bottom, different values of current were applied for dB_z/dz, dB_y/dy, dB_z/dy, dB_z/dx, dB_y/dx, and d^2B_z/dz^2, respectively.

4.3.3 Dependence on B_z

Like B_y, the residual field along the **z** direction results in a "dip" in M_x as B_x is scanned. The transmission signal was recorded as a function of B_x at $B_z = -0.38$ nT and $B_z = -0.25$ nT. For all the points, B_y was kept constant at -13 nT. Figure 4.10 shows the amplitude of the magnetic resonance as a function of B_x for the two values

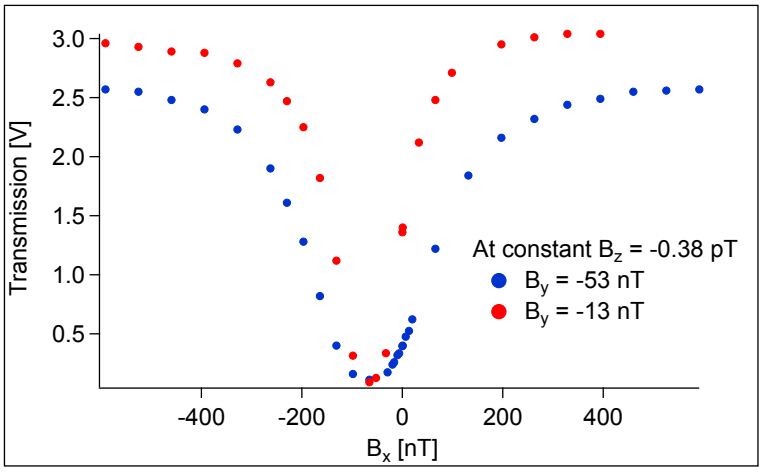

Figure 4.9: The magnetic resonance for B_x for two different values of B_y with constant B_z. The "dip" in the magnetic resonance suggests that the residual fields are not properly zeroed. Since residual fields closer to zero result in a narrower width of the dip, $B_y = -13$ nT was used for future measurements.

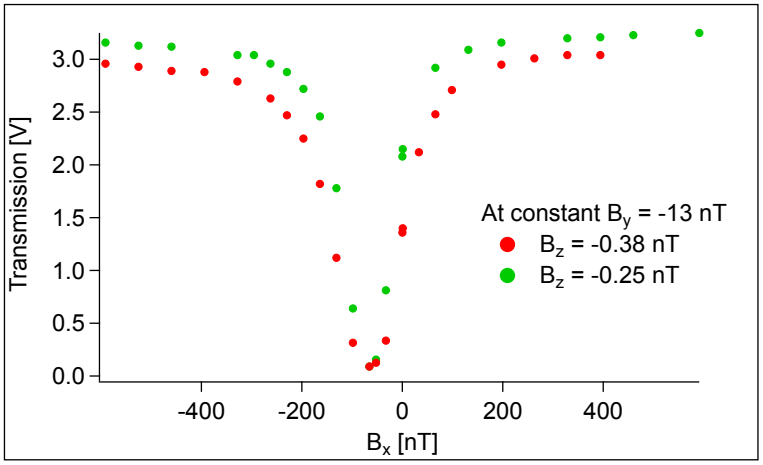

Figure 4.10: The magnetic resonance for B_x for two different values of B_z with constant B_y from the previous measurement (Figure 4.9). The "dip" in the magnetic resonance suggests that the residual fields are not properly zeroed. Since residual fields closer to zero result in a narrower width of the dip, $B_z = -0.25$ nT was used for future measurements.

of B_z.

Figure 4.10 suggests that the perpendicular components of the residual magnetic field are non zero. Similar to B_y, at some value of applied B_x, the residual B_x is minimized resulting in a minimum in the transmission signal. The figure suggests that $B_z = -0.25$ nT results in a smaller residual B_z field because the "dip" is narrower.

4.3.4 Near Zero Fields

In the previous sections, the effects of each component of the magnetic field on the magnetic resonance were investigated. Here, we investigate the magnetic resonances of B_x near the zero field region. As discussed earlier, the magnetic resonance as B_x is scanned shows a "dip" in amplitude when the fields are not properly zeroed, and the width of the magnetic resonance becomes smaller the closer to zeroed the fields are. Figure 4.11 shows the amplitude (red) and the width (blue) of the magnetic resonance as B_x is scanned at $B_y = -79$ pT, $B_y = -62$ pT, $B_y = -33$ pT, and $B_y = -13$ pT. For each B_y value, B_x was varied from -45 pT to $+45$ pT. For each combination of B_x and B_y, B_z was scanned to get a magnetic resonance. The amplitude and the width of each magnetic resonance were measured manually.

At $B_y = -79$ pT, the magnetic resonance shows a "dip" which suggests that the fields are not zeroed. When the width is minimized, the amplitude of the magnetic resonance is almost zero. At $B_y = -62$ pT, the width of the magnetic resonance is narrower, but the amplitude is still near zero when the width is minimized. At $B_y = -33$ pT, however, as the width decreases, the amplitude stays nearly constant. When the width is minimized, the amplitude is ~ 6 V. At $B_y = -13$ pT, the minimum width results in zero amplitude. From these measurements, we can conclude that the zero field is near $B_y = -33$ pT and $B_x = -10$ pT.

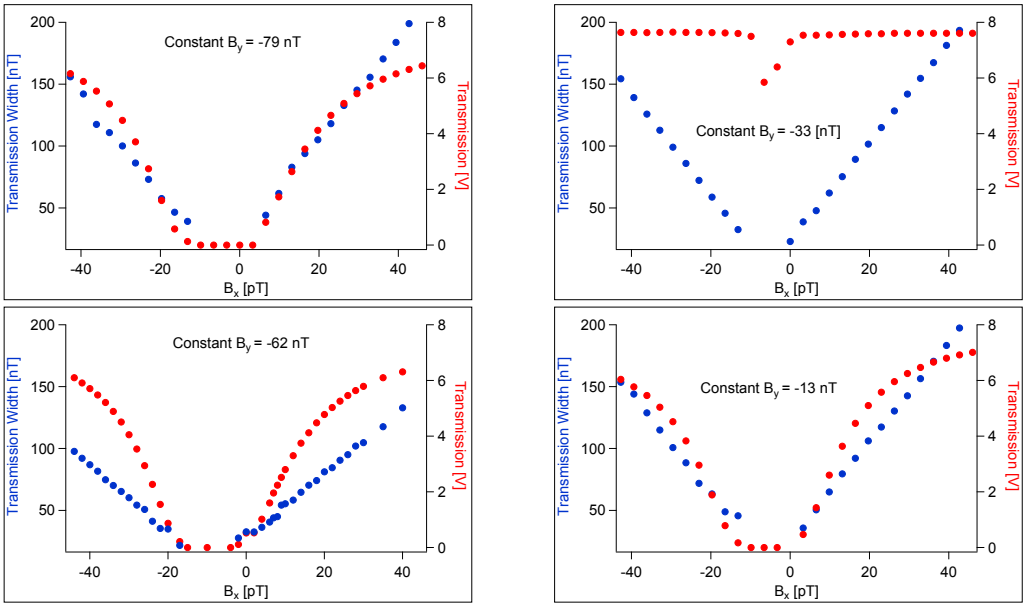

Figure 4.11: The magnetic resonance in B_x at four different values of $B_y = -79$ pT, $B_y = -62$ pT, $B_y = -33$ pT, and $B_y = -13$ pT from top to bottom and left to right. For each combination of B_x and B_y, B_z was scanned to get a magnetic resonance. The amplitude (red) and the width (blue) of the B_z resonance was measured manually, and the amplitude and width were plotted as a function of B_x. When the residual fields are close to zero, the width of the resonance is minimized. For $B_y = -79$ pT, $B_y = -62$ pT, and $B_y = -13$ pT, the minimum width results in almost zero amplitude. However, at $B_y = -33$ pT, the amplitude remains almost constant as the width decreases, and the minimum width results in a 6 V amplitude. Therefore, it is concluded that $B_y = -33$ pT produces residual fields that are closest to zero.

4.4 Zeroing Fields

Zeroing the residual fields inside the magnetic shield is essential because it directly affects the sensitivity of the K magnetometer. In the previous section, the amplitude and the width of the magnetic resonance were determined by scanning B_z for every change in the applied field. However, it takes a lot of time to scan B_z after changing one field. Here, we present a method to zero the fields by monitoring the transmission

signal.

1. First, we scan B_x by hand to see where the magnetic "dip" occurs. We adjust B_x so the transmission signal is about 10-20% of the maximum value. This is to put the atoms into the dark state by applying a small amount of leading field,

2. We change B_y and B_z and maximize the transmission signal. By doing this, we make sure we are cancelling any residual fields along the **y** and **z** directions and putting more atoms into the dark state.

3. We change all the gradients and maximize the transmission signal. This is to cancel out any gradient fields that are introduced in the shields due to the change in optical depth and due to the imperfect B_x, B_y, and B_z coils.

4. We go back to B_x and change it to *minimize* the transmission signal. This is to reduce the leading field.

5. Since the magnetic fields are related through Eq (3.1) and Eq (3.2), changing one field will change all the other fields. Therefore, we iterate Steps 2 through 4 until the values of the applied fields stay constant.

4.5 Unexpected Power Broadening

As discussed in section 2.7, the pumping power is not expected to broaden the magnetic resonance, because the pressure broadening is so much larger than the power broadening. However, when we scanned B_z, we observed the magnetic resonance getting broader as the pumping power increased as shown in Figure 4.12. We do not understand this power broadening. Since the width of the resonance is directly proportional to the sensitivity of the magnetometer, the K power of ~ 700 μW was chosen to be used in the experiment.

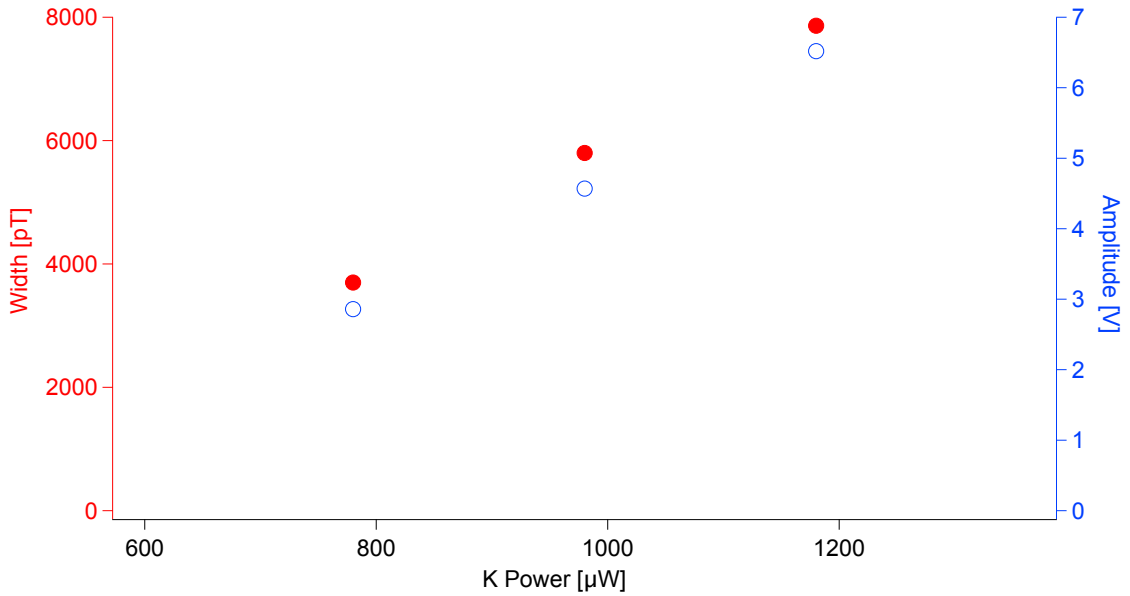

Figure 4.12: The width (filled red) and the amplitude (open blue) of the magnetic resonance in B_z at different K powers. As discussed in section 2.7, the pumping power does not broaden the magnetic resonance. However, we see broadening in the magnetic resonance with increased K power. Since the width of the resonance directly affects the magnetometer sensitivity, the K power around 700 μW was chosen to be used for the experiment.

4.6 Magnetic Field Data

4.6.1 Filters

To reduce the noise in the data that originate from artificial effects, we apply two types of post-acquisition, digital filters. Since we are only interested in the transient signals that occur over a 40-second period (see section 1.1.2), we apply a high-pass filter (1^{st} order Butterworth) with a corner frequency $f_c = 0.01$ Hz. The high-pass filter removes the low-frequency noise ($< f_c$), therefore eliminating the magnetic drifts that occur at a long time scale. We also apply a 4^{th} order Butterworth notch filter centered around $f = 60$ Hz to remove noise that comes from line signals.

4.6.2 Magnetic Field Data

Figure 4.13 shows the time series of the magnetometer data for one hour (EDT 20:00:00 to 21:00:00 on August 08, 2019). The data were taken at a sampling rate of $f_{sample} = 512$ Hz. The data were downsampled so that one in every 100 data points is displayed. The left (red) and right (blue) plots show the time series of the raw data and the filtered data (see 4.6.1), respectively.

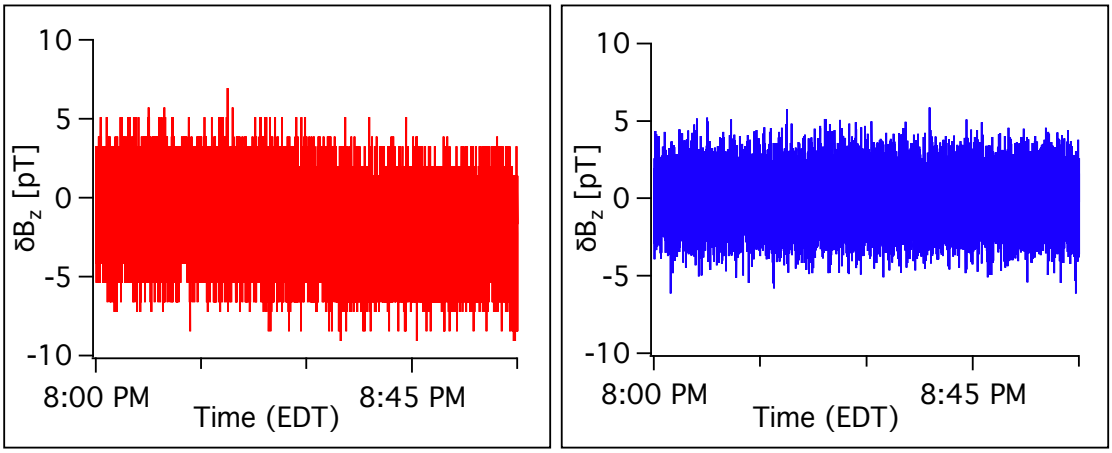

Figure 4.13: The time series from EDT 20:00:00 to 21:00:00 on August 08, 2019. The left (red) and right (blue) represent the raw data and the filtered data, respectively. The scales are the same in both plots. In the filtered data, the magnetic drift and the signals at 60 Hz are reduced, resulting in less noise.

Figure 4.14 shows the square-root of the power spectral density (PSD) of the time series shown in Figure 4.13. The red represents the PSD of the raw data, and the blue represents the PSD of the filtered data.

There are some notable features of the raw magnetometer data shown in Figure 4.14. First, there is a relatively large peak at 60 Hz (line frequency). The signals at this frequency originate from electronic noise, rather than from magnetic noise. Second, there is a rise of the PSD at low frequencies, which suggests the presence magnetic

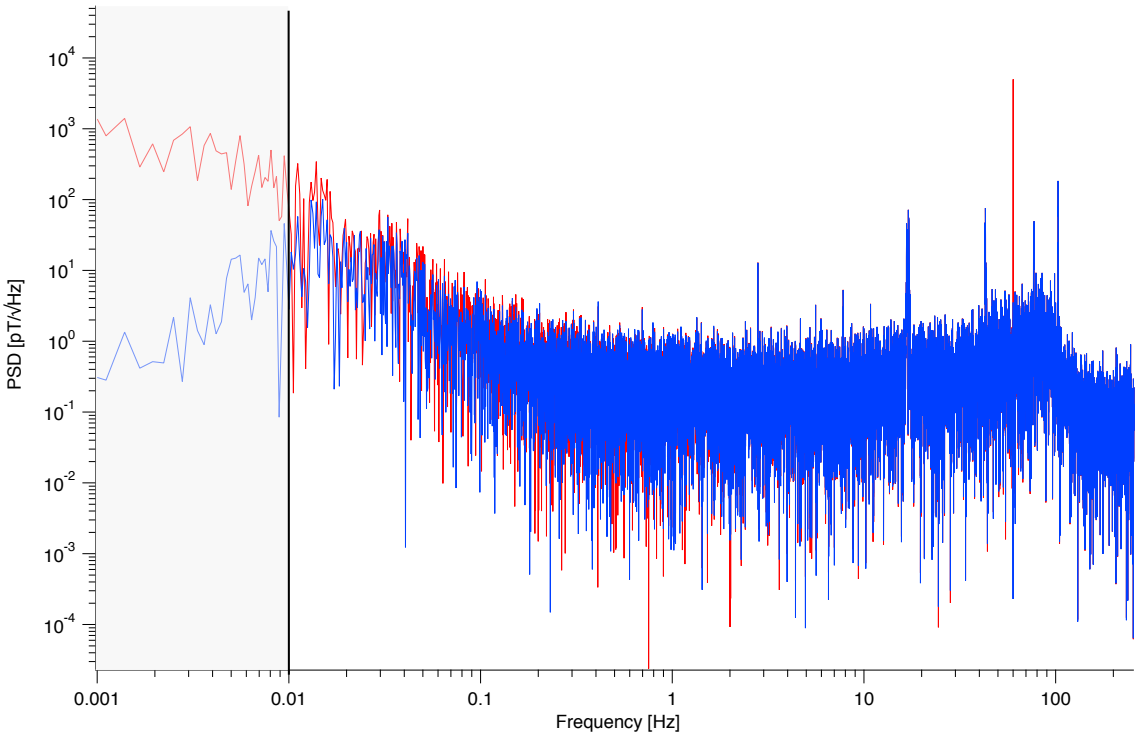

Figure 4.14: The square-root of the power spectral density (PSD) of the one-hour time series shown in Figure 4.13. The red and the blue represent the raw and the filtered data, respectively. The black horizontal line indicates the cutoff frequency of the high-pass filter (mentioned in section 4.6.1). The rise in the low-frequency region is removed by the high-pass filter, and the peak at 60 Hz is removed by the notch filter in the filtered PSD.

drifts at long time scales (> 100 s). Therefore, to reduce such noise, we apply filters described in section 4.6.1.

In Figure 4.14, the noise is a few 100 fT/$\sqrt{\text{Hz}}$ over the 0.5-100 Hz range. This is significantly higher than the 1.5 fT/$\sqrt{\text{Hz}}$ estimated in section 2.8. We attribute additional noise to imperfect alignment of the laser with respect to the B field generated inside the shields and imperfections in the circular polarization of the light.

4.6.3 Histograms

The approaches to the analysis of the GNOME magnetometer data for finding the transient signals with exotic physics origins are built on the assumption that the magnetic field data exhibits a Gaussian distribution [14]. Histograms provide a good way to represent the distribution of the data.

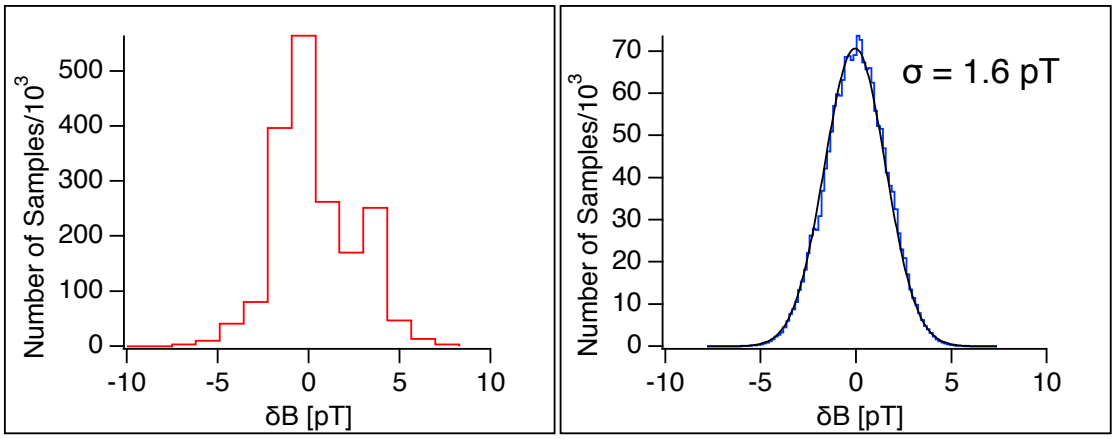

Figure 4.15: The histograms for the raw (red) data and the filtered (blue) data of the one-hour time series shown in Figure 4.13. The histogram for the filtered data follows a Gaussian distribution and was fitted to a Gaussian function (black), yielding a standard deviation of $\sigma = 1.6$ pT.

Figure 4.15 shows the histograms of the same data used in Figure 4.13. The left (red) represents the histogram of the raw data, and the right (blue) represents the histogram of the data after the two filters described in section 4.6.1. The histogram of the filtered data was fitted to a Gaussian function, and the fit is represented by the black curve. The fit resulted in a standard deviation of $\sigma = 1.6$ pT. We can see that with the filters used the data follow a Gaussian distribution, which suggests the filters used are appropriate for the preparation of data for analysis.

4.6.4 Long Term Characteristics

Here, we look at longer term characteristics of the magnetometer data. Figure 4.16 shows the time series of the magnetometer data for one day (EDT 20:00:00 to 19:59:59 on August 08 to August 09, 2019). Here, we can see more clearly the effect of the post-acquisition, digital filtering. The magnetic drift over the course of one day is removed by the high-pass filter, and the overall noise level is reduced by the notch filter.

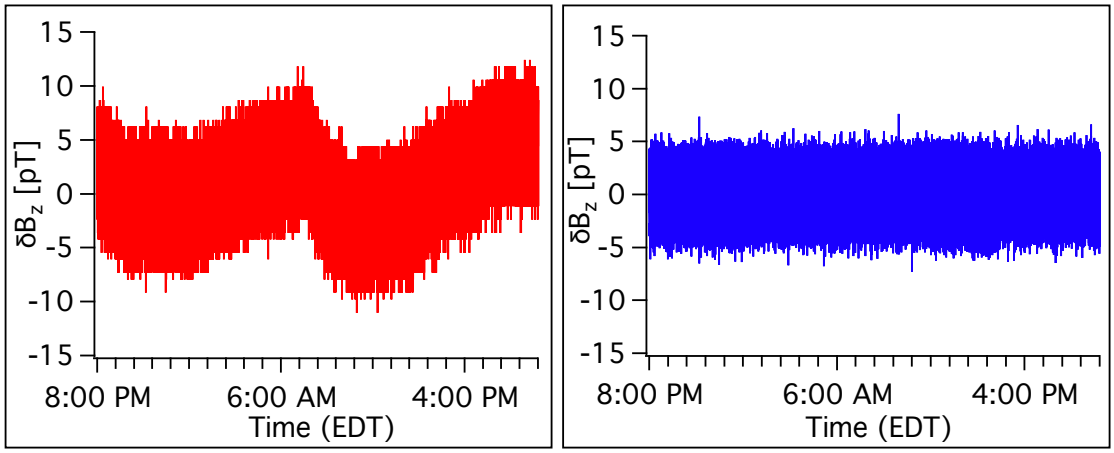

Figure 4.16: The time series from EDT 20:00:00 on August 08 to 19:59:59 on August 09, 2019. The left (red) and right (blue) represent the raw data and the filtered data, respectively. The scales are the same in both plots. In the filtered data, the magnetic drift and the signals at 60 Hz are reduced, resulting in less noise.

Figure 4.17 shows the histograms of the time series of one day shown in Figure 4.16. The red and blue represent the histograms of the raw and filtered data, respectively. The filtered histogram was fitted to a Gaussian distribution and yielded a standard deviation of $\sigma = 1.6$ pT. Similar to the short-term data, the long-term data follow a Gaussian distribution after filtering.

Figure 4.18 shows the time series of the magnetometer signals for five days (EDT 20:00:00 to 20:00:00 from August 7-12, 2018) of uninterrupted data. The red and the blue represent the raw and the filtered data, respectively.

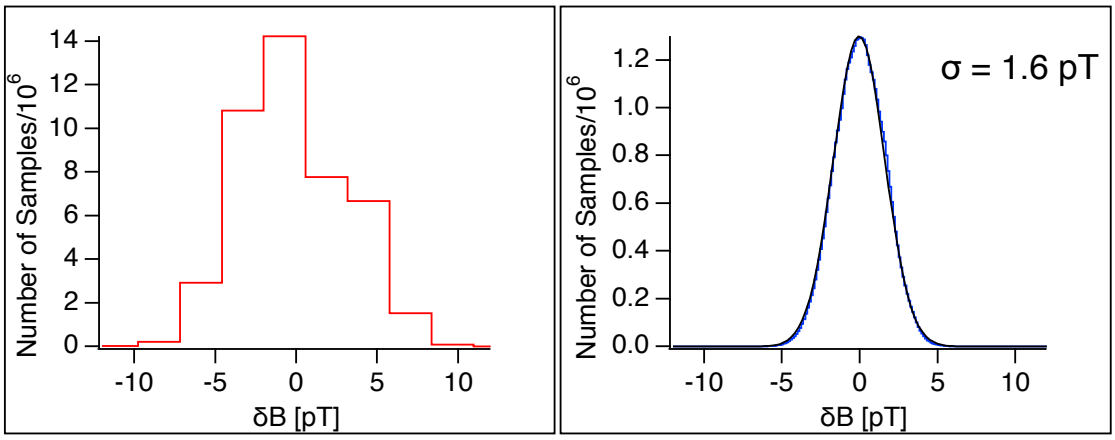

Figure 4.17: The histograms for the raw (red) data and the filtered (blue) data of the one-day time series shown in Figure 4.16. The histogram for the filtered data follows a Gaussian distribution and was fitted to a Gaussian function (black), yielding a standard deviation of $\sigma = 1.6$ pT.

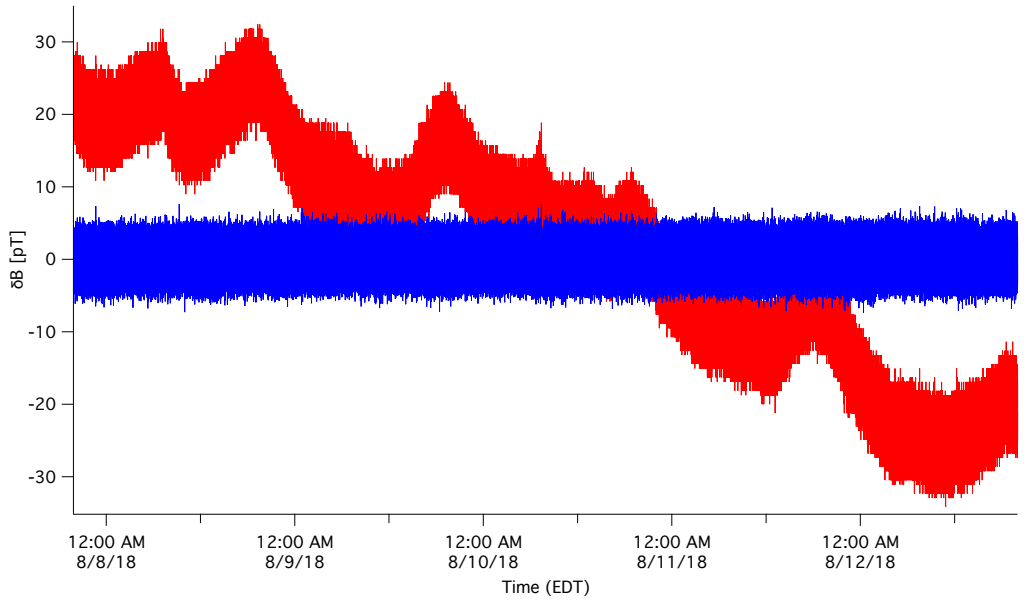

Figure 4.18: The time series from EDT 20:00:00 on August 08 to 19:59:59 on August 12, 2019. The red and blue represent the raw data and the filtered data, respectively. In the longer time series, the effects of filtering are more apparent; in the filtered data, the magnetic drift and the signals at 60 Hz are reduced, resulting in less noise.

4.7 Magnetic Bandwidth and pulses

4.7.1 Bandwidth Response

To measure the bandwidth of the magnetometer, a sinusoidally oscillating current with 50-pT rms amplitude was applied to the additional, homemade B_z coils. The frequencies of the sine wave were varied, and the rms amplitudes of the corresponding magnetic field data were recorded. The results in Figure 4.19 show the 3 dB point at 100 Hz.

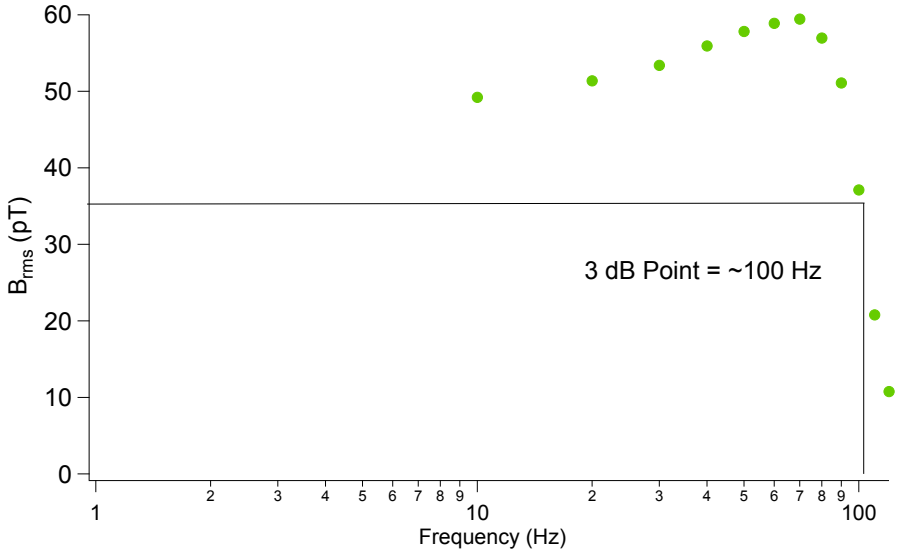

Figure 4.19: The bandwidth measurement of the magnetometer. A sinusoidally oscillating current with 50-pT rms amplitude was applied to the homemade coils along the **z** direction to measure the magnetometer response.

4.8 Test Pulse

To investigate the time resolution of the magnetometer data between stations around the world, the GNOME collaboration performs test pulses during which a fake pulse is injected into the data that are timestamped with GPS.

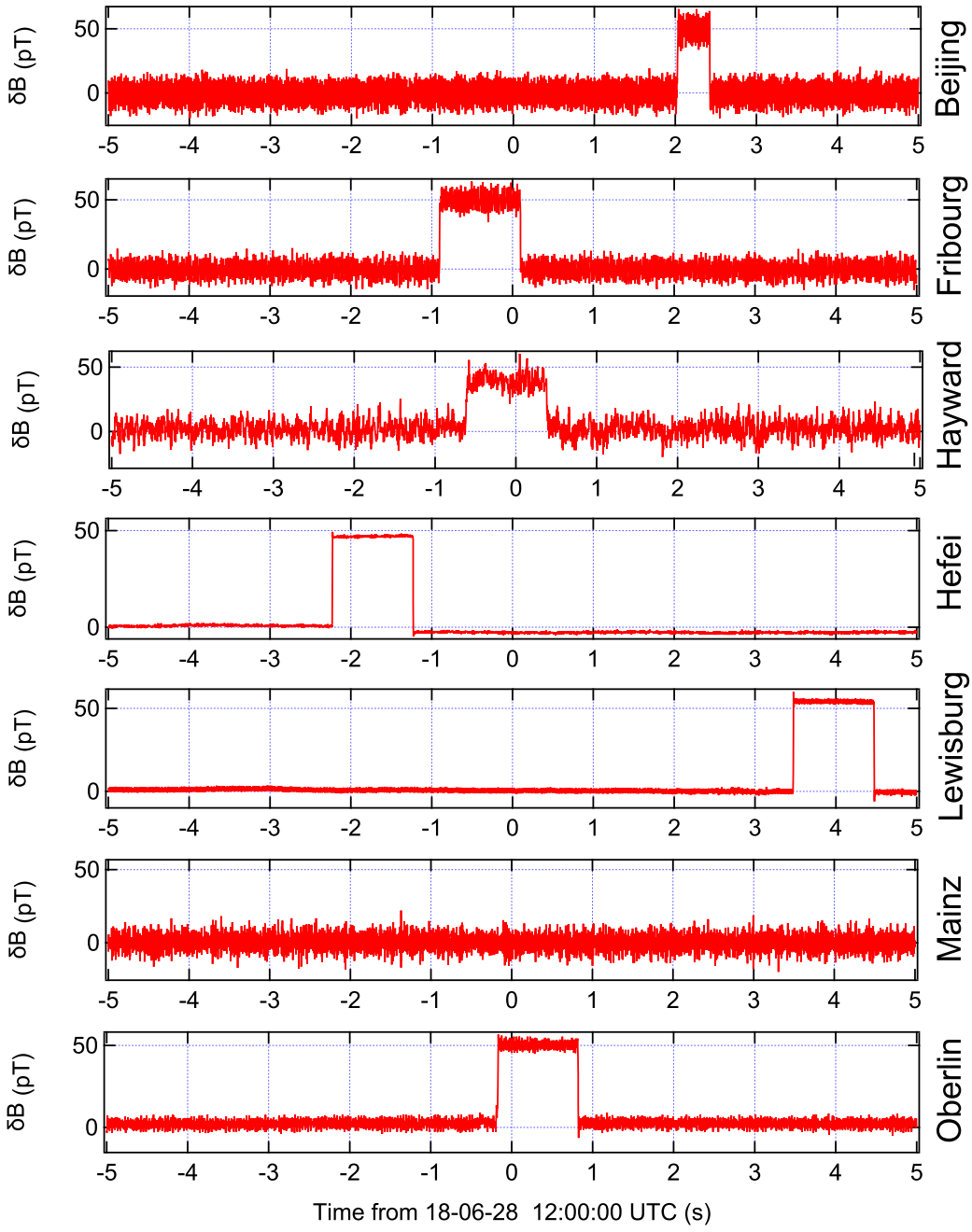

Figure 4.20: The result of the GNOME test pulse performed on June 28, 2018. The pulse was intended to occur at UTC 12:00:00. The pulses from the six stations had a time window on the order of a few seconds due to the insufficient time resolution of computer clocks and due to the latency of the hardware.

A total of six stations participated in the test pulse during June of 2018. Figure 4.20 shows the result of the June 2018 test pulse. The pulses from the six stations had a time window on the order of a few seconds. It was concluded that this was due to the insufficient time resolution of computer clocks, even when synchronized via the internet time service provided by NIST, and due to the latency of the internet, computer, and the function generator.

4.8.1 Test Pulse with GPS Time

In this section, a simple circuit that we developed at Oberlin College is described to achieve better pulse timing using an Arduino Uno, a GPS Logger Shield with the GP3906-TLP GPS Module (SparkFun), and an AND gate. The motivation of this experiment was to develop a circuit, costing under $100, that would provide sufficient time resolution for the future test pulses. Using this circuit, we were able to generate a pulse within 2 milliseconds of the PPS (pulse-per-second) signal at the desired time.

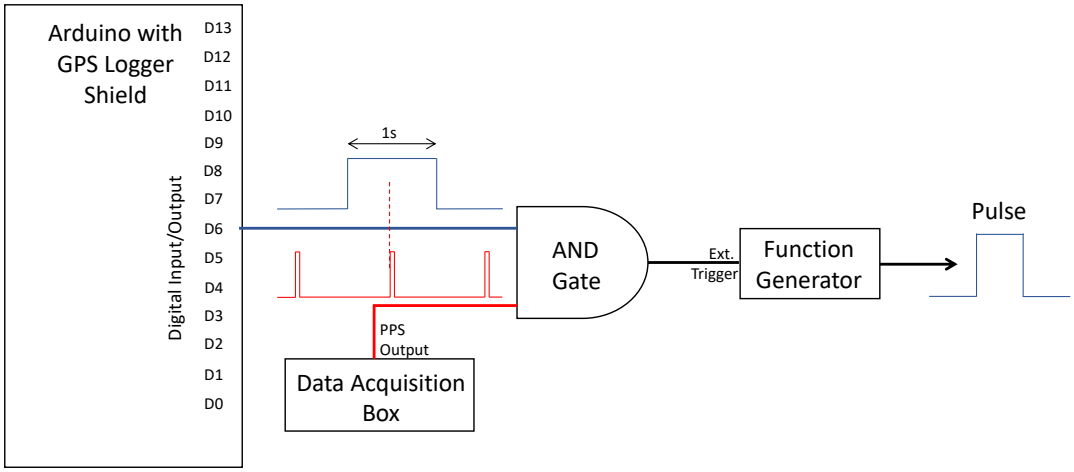

Figure 4.21: Schematic for the GPS Timing device. The Arduino unit outputs a 1-second pulse at the specified time after a 0.5-second delay and provides a window for the desired pulse time. At the desired time, the AND gate goes high and the function generator sends out a pulse.

The schematic of the circuit is shown in Figure 4.21. For our application, we have modified the Arduino sketch provided by SparkFun. The Arduino sketch uses *TinyGPS++* library which parses NMEA strings. The time received by the GPS module is read using *Serial Monitor*. Using an *If* statement, a 1-second pulse is generated by the GPS Logger Arduino unit at a specified time with a 0.5-second delay. This output goes through an AND gate, along with the PPS output from the Data Acquisition Box. The output of the GPS Logger sets up a window that contains the pulse time of interest. As the PPS signal goes high at the desired time, the output of the AND gate goes high. This is then used for *External Trigger* for the function generator. We used *Arbitrary Waveform Generator* software to generate a pulse with the desired width and amplitude for our function generator (SRS DS 345).

The response of the pulse is shown in Figure 4.22. We have generated a pulse within 2 milliseconds of the desired time as shown in Figure 4.23. We were also able to include a delay on the pulse using *Arbitrary Waveform Generator*.

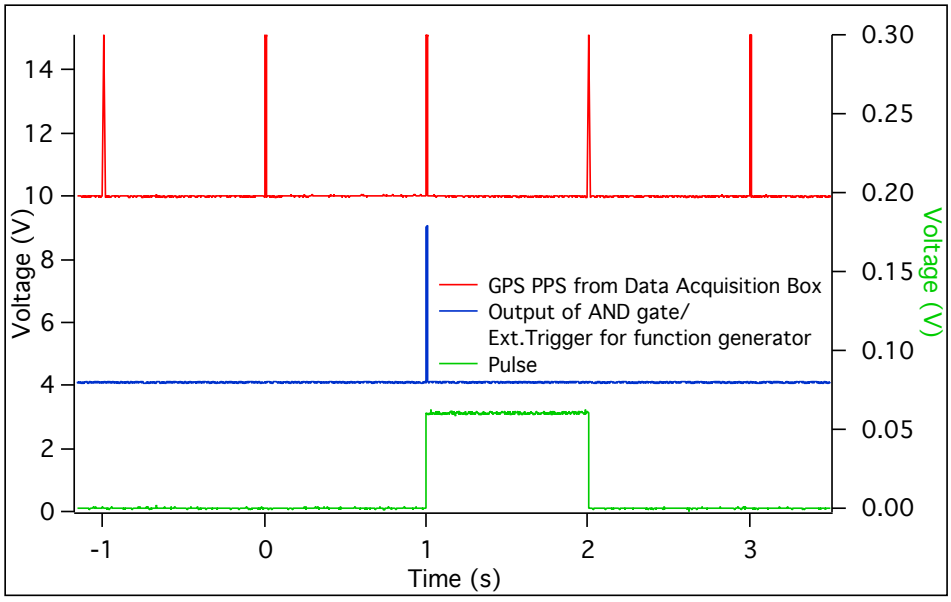

[h!]

Figure 4.22: Response of the pulse with no built-in delay. Vertical offsets were added to the GPS PPS signal (red) and the output of the AND gate (blue).

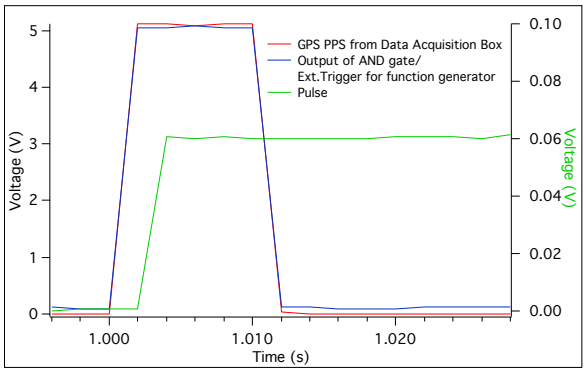

Figure 4.23: A zoomed-in version of Figure 4.22. As shown in the figure, there is a 2-millisecond delay between the output of the AND gate and the pulse, even with no built-in delay on the pulse.

4.8.2 Test Pulse in March, 2019

The scheme described in section 4.8.1 was implemented for the GNOME test pulse in March, 2019. Six stations participated. Figure 4.24 shows the pulses from three stations (Oberlin, Mainz, and Hefei) that appropriately applied the pulse at the scheduled time of 12:00:00 UTC. The other participating stations made errors in setting up the Arduino pulse described in section 4.8.1.

The timing of the applied pulses agree within the sampling time ($1/512$ s $= 0.0019$ ms). Even though only three of the stations were able to implement the scheme correctly, this shows its potential for use in future test pulses.

4.9 Magnetometer Dependence on External Temperature

We realized the correlation between the external temperature and the magnetic drift. Figure 4.25 shows the magnetometer data and the external temperature. Within a day, the temperature fluctuation of 0.8 °C resulted in the magnetic fluctuation of $\sim$ 250 pT

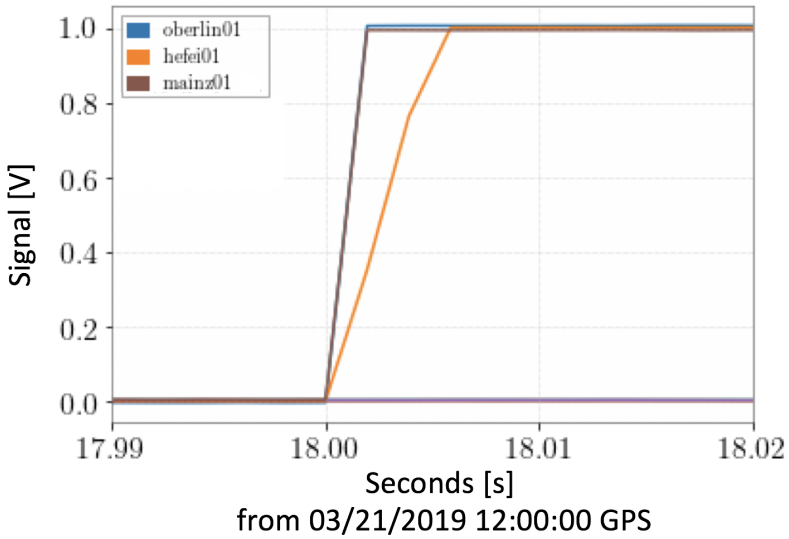

Figure 4.24: Result of the GNOME test pulse performed in March, 2019. The scheme described in section 4.8.1 was implemented. The pulses from the three stations that applied the pulse at the scheduled time (12:00:00 UTC) are shown. Note that the plot is in GPS time, which is 18 seconds ahead of UTC time. The pulses from these three stations agree within 2 ms. The plot was generated by Hector Masia at Johannes Gutenberg University, Mainz.

(red). We installed insulation as discussed in section 3.1.3, and the magnetic drift due to temperature change was reduced significantly (blue). It is possible that the shielding factor of the shields changes with temperature.

4.10 Precession of ^{3}He

When trimming the fields according to the procedure mentioned in section 4.4, we occasionally observe oscillations with long periods. To investigate these long-term oscillations, we took data at different values of B_y and constant B_x and B_z. Fast Fourier Transform (FFT) was performed for each data set. Figure 4.26 shows the frequency with the highest amplitude in the FFT as a function of B_y.

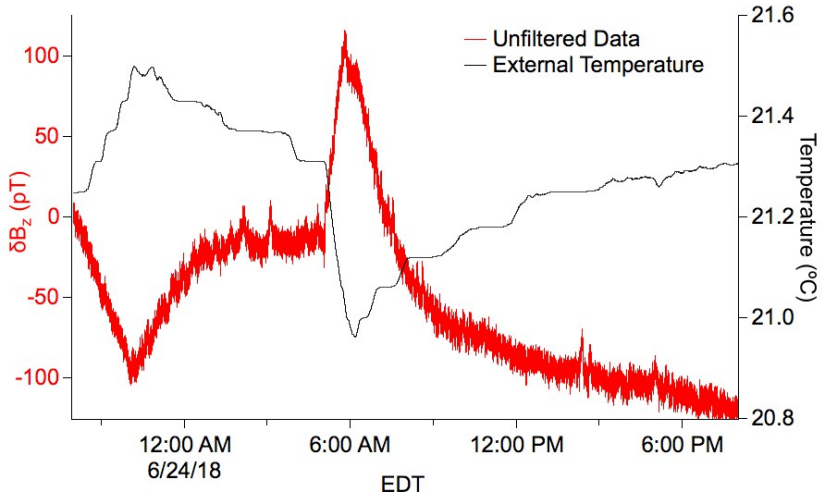

(a)

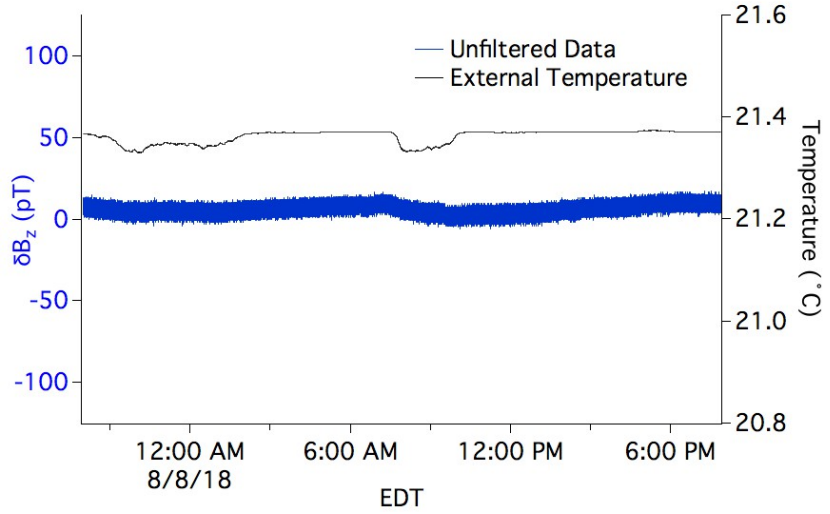

(b)

Figure 4.25: The red (a) and the blue (b) represent the magnetometer data (left axis) and the external temperature (right axis) before and after insulation was installed. Before insulation, the external temperature fluctuated about 0.8 °C, resulting in magnetic fluctuation of $\sim$ 250 pT. After insulation was installed, the fluctuations in both the external temperature and the magnetic data were reduced significantly.

The value of B_y that resulted in the smallest frequency was chosen, and the same procedure was carried out for different values of B_z at constant B_x and at this B_y value. The oscillation frequency as a function of B_z is shown in Figure 4.27.

The linear sections of Figure 4.26 and Figure 4.27 were fitted to a line to get the relation between the oscillation frequency and the magnetic field. The slopes for B_y and B_z were: 2.3×10^{-5} [Hz/pT] and 3.2×10^{-5} [Hz/pT], respectively. The gyromagnetic ratio of ^{3}He is $\gamma_{^3\mathrm{He}}/2\pi = 32.4$ [MHz/T] $= 3.2 \times 10^{-5}$ [Hz/pT] [22]. These measurements suggest that the oscillations are from ^{3}He atoms in the vapor cell. Since the B_y measurement (Figure 4.26) was done prior to the B_z measurement (Figure 4.27), it can be concluded that when the B_y measurements were carried out, the other perpendicular component B_z was not zeroed perfectly, resulting in the measured gyromagnetic ratio being slightly different from the literature value. A value of B_y that minimized the oscillation frequency was chosen for the B_z measurement, resulting in the measured gyromagnetic ratio being closer to the actual value.

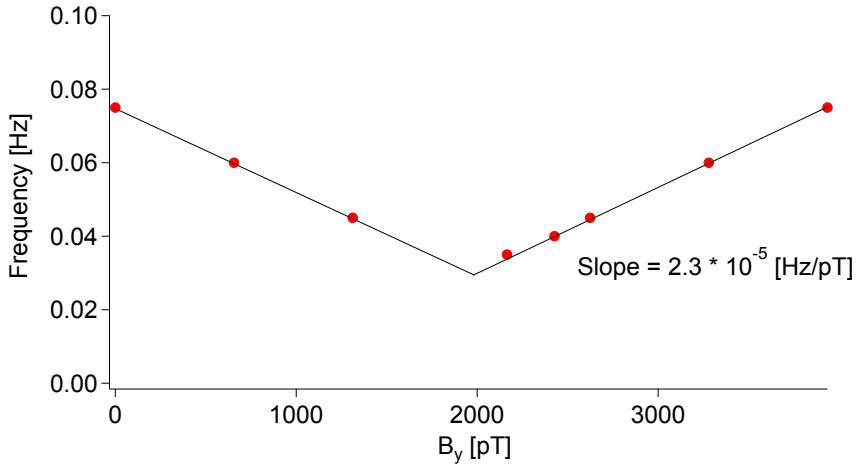

Figure 4.26: The frequency of long-term oscillations in the transmission signal as a function of applied B_y. B_x and B_z were kept constant. The linear part was fitted to a line and gave a slope of 2.3×10^{-5} [Hz/pT]. The B_y value that resulted in the smallest frequency was used for future measurements.

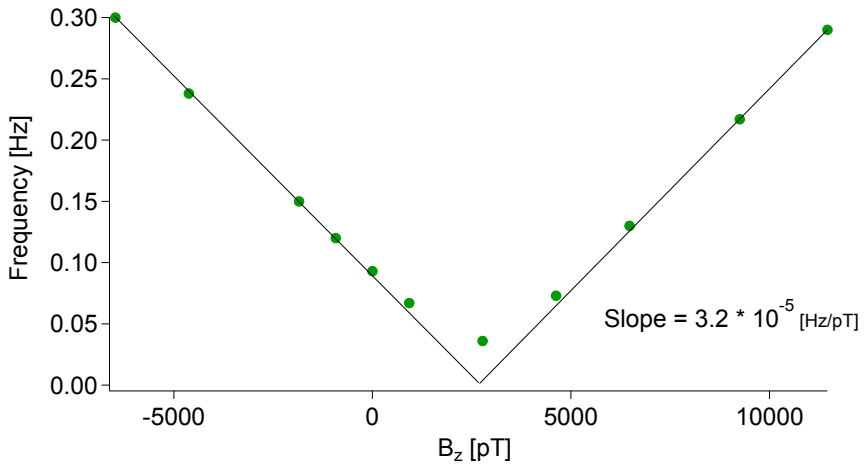

Figure 4.27: The frequency of long-term oscillations in the transmission signal as a function of applied B_z. B_x and B_y were kept constant. The linear part was fitted to a line and gave a slope of 3.2×10^{-5} [Hz/pT]. This slope agrees with the gyromagnetic ratio of ^{3}He, $\gamma_{^3\mathrm{He}}/2\pi = 3.2 \times 10^{-5}$ [Hz/pT] [22].

Chapter 5

Towards the Development of the Comagnetometer

Before implementing the Rb-K-^{3}He comagnetometer, we investigated the effects of hybrid pumping. The Rb laser tuned at the Rb D1 transition was added as the pump beam in the K magnetometer system described in Chapter 3. The Rb laser is along the axis of the probe beam, which is tuned to the K D1 transition. In the following sections, basic concepts of hybrid pumping and the nuclear-electronic spin-coupling, the experimental setup, and some characterization, of the co-linear Rb-K hybrid pumping magnetometer are discussed.

5.1 Theory of Rb-K-^{3}He Comagnetometer

Ultimately, we want to build a Rb-K-^{3}He comagnetometer which has a higher estimated sensitivity than the current K magnetometer. For the comagnetometer, the ensemble of the Rb and K atoms is used for the hybrid pumping effect. A combination of K and ^{3}He atoms is also used, which makes the comagnetometer insensitive to magnetic fields, but still sensitive to anomalous spin-coupling.

In the comagnetometer, two laser systems will be used: one for pumping and the other for probing. In our system, we would be pumping the Rb atoms and probing

the K atoms. The Rb atoms are polarized along the **z**-axis. The polarized Rb atoms go through spin-exchange collisions to polarize the K atoms along the **z**-axis. Then, the K atoms polarize the ^{3}He atoms via spin exchange. The polarized ^{3}He atoms produce a uniform magnetic field throughout the spherical cell. An external magnetic field is applied to cancel the field from the ^{3}He atoms so that the K atoms do not feel any magnetic field inside the vapor cell. At this point, the electronic spins in the K atoms are strongly coupled to the nuclear spins in the ^{3}He atoms. This coupling results in a self-compensating comagnetometer which has higher sensitivity than the K magnetometer and which can reduce the effects of magnetic drifts. The rotation of the K probe light polarization through the vapor cell along the **x**-axis is measured as a magnetic field measurement.

The K-Rb spin-exchange cross section is large (roughly 200 Å^2) [40]. In a high density environment ($\sim 10^{14}$ cm^{-3}), this cross section results in a K-Rb spin-exchange rate of about 10^5 1/s. This is much greater than the K-^{3}He spin-exchange rate, which is typically 500 1/s [41]. As a result, the Rb and K atoms are in spin-temperature equilibrium with the same electron spin polarization.

5.1.1 Hybrid Pumping

Both Rb and K atoms are alkali atoms with $S = 1/2$. When a Rb atom and a K atom go through a binary collision, it is possible for them to exchange their spin angular momentum. Higher sensitivity can be achieved by pumping Rb atoms and probing K atoms. The K and Rb come together in an intermolecular potential and exchange their angular momenta. This mechanism of spin-exchange collisions between the K and Rb atoms is shown in Figure 5.1.

In the comagnetometer, the spin-exchange efficiency is defined as [33]

$$\eta_A = \frac{\gamma_{se}^{\mathrm{A}} n_{^3\mathrm{He}}}{\Gamma_{\mathrm{A}} n_{\mathrm{A}}}, \tag{5.1}$$

where $\gamma_{se}^{\mathrm{A}} = k_{se}^{\mathrm{A}} n_{\mathrm{A}}$ is the spin-exchange rate from the alkali metals (A = Rb or K) to the ^{3}He atoms, k_{se}^{A} is the spin-exchange rate constant for the alkali metal atom, n_{A} is

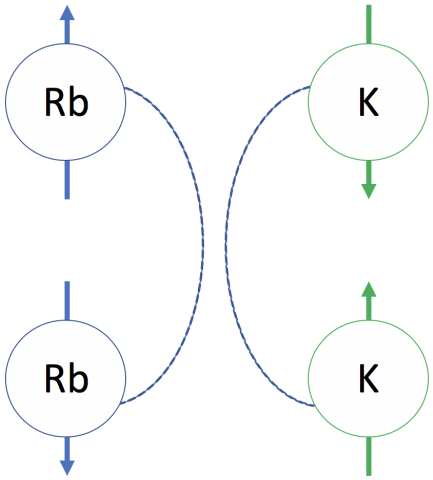

Figure 5.1: Cartoon picturing a spin-exchange collision between a Rb atom and a K atom. The Rb and K atoms come together in an intermolecular potential and exchange angular momenta. By pumping the Rb atoms to have spin-up configuration, we polarize the K atoms to have the same spin-up configuration via spin-exchange collisions. The picture was adapted from Ref. [20].

the density of the alkali metal atoms, $n_{^3\mathrm{He}}$ is the density of ^{3}He atoms, and Γ_A is the electronic spin-destruction rate for the alkali atoms. The spin-exchange rate between the Rb and K atoms in the cell is [33]

$$\gamma_{se}^{\text{Rb-K}} = k_{se}^{\mathrm{Rb}} n_{\mathrm{Rb}} + k_{se}^{\mathrm{K}} n_{\mathrm{K}}. \tag{5.2}$$

If we pump on the Rb atoms, the effective spin-destruction rate in Eq (5.1) is

$$\Gamma'_{\mathrm{Rb}} = \Gamma_{\mathrm{Rb}} + D\Gamma_{\mathrm{K}} + q_{\mathrm{KRb}} n_{\mathrm{K}}, \tag{5.3}$$

where $D = n_{\mathrm{K}}/n_{\mathrm{Rb}}$ is the ratio of the vapor densities and q_{KRb} is the spin-destruction rate constant for Rb-K collisions, which is small in typical comagnetometer operating conditions [41].

We want to increase the spin-exchange efficiency because increased efficiency allows [33]: (1) increased number of polarized atoms that can be produced for a given pumping power of the laser, (2) increased production rate of polarized atoms by operating at a

higher temperature and increasing the density (and ultimately the spin-exchange rate), and (3) ability to polarize the same number of atoms with reduced laser power. In the following sections, we will look at each term in Eq (5.1.1).

5.1.1.1 Spin-exchange Rate Constants for Rb and K

The spin-exchange rate constants for Rb and K are $k_{se}^{\mathrm{Rb}} = 6.8 \times 10^{-20}$ cm^3/s and $k_{se}^{\mathrm{K}} = 5.5 \times 10^{-20}$ cm^3/s, respectively [42]. The spin-exchange rate constants for Rb and K are comparable. Therefore, the spin-exchange rates γ_{se}^{A} for Rb and K atoms are about the same at a given density. This suggests that for the γ_{se}^{A} term, it does not make a big difference in the spin-exchange efficiency given in Eq (5.1) whether K or Rb atoms are used to polarize ^{3}He atoms.

5.1.1.2 Spin-destruction Rate for Rb and K

The term Γ_{A} in Eq (5.1.1) describes the total alkali metal spin-destruction rate. This term can be broken down into

$$\Gamma_{\mathrm{A}} = \Gamma_{\mathrm{A\text{-}A}} + \Gamma_{\mathrm{A\text{-}^3He}} + \Gamma_{\mathrm{A\text{-}N_2}}, \tag{5.4}$$

where the terms describe the spin-destruction rates from A-A, A-^{3}He, and A-N_2 collisions in order. For experimentally determined spin-destruction rates for all of these combinations of species, see Refs. [34, 32, 43]. From section 2.5.2, we know that the spin-destruction rates depend on the spin-destruction cross section (reported in Table 2.1), the density, and the thermal velocity of the atoms.

From Table 2.1, we can see that the K atoms have smaller spin-destruction cross sections for all K-K, K-^{3}He, and K-N_2 collisions than the the spin-destruction cross sections for all Rb-Rb, Rb-^{3}He, and Rb-N_2 collisions. From these values, we expect $\Gamma_{\mathrm{K}} \ll \Gamma_{\mathrm{Rb}}$. Therefore, the efficiency given by Eq (5.1.1) is increased by using the ensemble of Rb and K atoms and pumping on the Rb atoms. In conclusion, we can see that the use of hybrid pumping of the Rb-K ensemble, in which the Rb atoms are pumped, increases the spin-exchange efficiency, and ultimately, the magnetometer

sensitivity. In addition, since Rb is the minority species in the vapor cell, this means that we can use a large pumping rate without increasing radiation trapping. The excited Rb atoms emit radiation from spontaneous emission in random directions. However, since the wavelength of the Rb D1 transition is very different from that of the K D1 transition, the emitted radiation does not get absorbed by the K atoms; therefore, the K atoms are not depolarized.

5.1.2 Optical Pumping of ^{3}He

In the co-magnetometer, the polarized electronic spins of the K atoms polarize the ^{3}He atoms via spin-exchange collisions. The term $R_{se}^{^3\text{He-K}}$ describes the spin-exchange collision rate experienced by ^{3}He and is related to the spin-exchange collision rate experienced by the K, $R_{se}^{\text{K-}^3\text{He}}$, by [20]

$$R_{se}^{^3\text{He-K}} = R_{se}^{\text{K-}^3\text{He}} \frac{n_{\text{K}}}{n_{^3\text{He}}}, \tag{5.5}$$

where n_{K} is the density of the K vapor, and $n_{^3\text{He}}$ is the density of the ^{3}He atoms. Using the values from Table 2.2, $R_{se}^{^3\text{He-K}} \simeq \frac{1}{160}\ \frac{1}{\text{Hour}}$. The polarization of ^{3}He $P^{^3\text{He}}$ is defined as

$$P^{^3\text{He}} = P^{\text{K}} \frac{R_{se}^{^3\text{He-K}}}{R_{se}^{^3\text{He-K}} + 1/T_1^{^3\text{He}}}, \tag{5.6}$$

where P^{K} is the polarization of K atoms and $T_1^{^3\text{He}}$ is the longitudinal relaxation time of ^{3}He.

For a perfectly spherical cell, the field inside the cell is uniform. However, if the cell is not perfectly spherical, gradient fields are introduced. Practically, the term $T_1^{^3\text{He}}$ is limited by the decoherence in spin precession caused by the gradient field and due to the diffusion of the ^{3}He atoms in the vapor cell. To increase the polarization of the ^{3}He atoms $P^{^3\text{He}}$, we can increase the number of polarized K atoms, to increase the term $R_{se}^{^3\text{He-K}}$. Therefore, increasing the spin-exchange efficiency given in Eq (5.1) increases the sensitivity of the magnetometer.

5.1.3 Nuclear-electronic Spin Coupling

The spins of the two species in the K-^{3}He ensemble are strongly coupled due to the spin-exchange interactions. Since the field inside a perfect sphere is uniform, we can express the effective magnetic field experienced by one species from the magnetization of the other species as [44]

$$\mathbf{B} = \lambda M \mathbf{P} = \frac{8\pi\kappa_0}{3} M\mathbf{P}, \tag{5.7}$$

where $\lambda = 8\pi\kappa_0/3$ [45], κ_0 is the enhancement factor due to the attraction of the K electron wavefunction to the ^{3}He nucleus, and $\mathbf{P}$ is the polarization. The value of $M = \mu n$ is the magnetization density where μ is the magnetic moment and n is the number of atoms. At $T = 165$ °C, for the K-^{3}He spin-exchange $\kappa_0 = 5.7$ [34]. The Bloch equations describing the spin polarizations in the ensemble are [20, 44]

$$\begin{aligned}\frac{\partial \mathbf{P}^e}{\partial t} &= \mathbf{\Omega} \times \mathbf{P}^e + \frac{\gamma_e}{Q(P^e)}(\mathbf{B} + \lambda M_0^n \mathbf{P}^n + \mathbf{L} + \mathbf{b}^e) \times \mathbf{P}^e + \\ &\quad (R_{Pump}\mathbf{s_p} + R_{se}^e \mathbf{P}^n + R_m \mathbf{s_m} - R_{Total}\mathbf{P}^e)/Q(P^e), \\ \frac{\partial \mathbf{P}^n}{\partial t} &= \mathbf{\Omega} \times \mathbf{P}^n + \gamma_n(\mathbf{B} + \lambda M_0^e \mathbf{P}^e \mathbf{b}^n) \times \mathbf{P}^n + R_{se}^n(\mathbf{P}^e - \mathbf{P}^n) - R_{sd}^n \mathbf{P}^n.\end{aligned} \tag{5.8}$$

The term $\mathbf{\Omega}$ is the inertial rotation rate of the surroundings that the spins experience. The terms γ_e and γ_n are the K gyromagnetic ratio and the ^{3}He gyromagnetic ratio, respectively. The terms M_0^e and M_0^n describe the the magnetizations of the K and the ^{3}He atoms at full polarization (P=1). For the first equation in Eq (5.8), which is the rate equation for the K polarization, the total effective magnetic field that the electron spins experience is the sum of the ambient magnetic field $\mathbf{B}$, the magnetic field generated by the ^{3}He atoms $\lambda M_0^n \mathbf{P}^n$, the light shift from the beams $\mathbf{L}$, and an anomalous field $\mathbf{b^e}$. The terms R_m and R_{Pump} are the pumping rate of the probe beam and pumping beam, respectively. The terms $\mathbf{s_p}$ and $\mathbf{s_m}$ describe the directions and the magnitudes of the photon spin polarizations of the pump and probe beams. For circularly polarized light, $s_p = 1$ and the polarization of the electron spins is: $(s_p - P^e)R_{pump}$ [20]. The probe beam can also polarize the K atoms when the probe beam has some circular

polarization (i.e. $s_m \neq 0$); this polarization of the K atoms is $(s_m - P^e)R_m$, and this term is only considered in the absence of the pump beam [20]. The electron spins relax at a rate R_{Total} described in section 2.5. The term $Q(P^e)$ is the electron slowing-down factor discussed in section 2.5. For the second equation in Eq (5.8), which is the rate equation for the ^{3}He polarization, the total effective magnetic field that the nuclear spins experience is the sum of the ambient magnetic field $\mathbf{B}$, the magnetic field generated by the K atoms $\lambda M_0^e \mathbf{P}^e$, and an anomalous field $\mathbf{b^n}$.

For the transient spin dynamics, Eq (5.8) can be simplified. For the system with $\mathbf{B} = B\hat{\mathbf{z}}$, the Bloch equations become [20, 46]

$$\begin{aligned}\frac{\partial \mathbf{M}^e}{\partial t} &= \frac{\gamma_e}{Q(P^e)}(\mathbf{B} + \lambda \mathbf{M}^n) \times \mathbf{M}^e + R_{Total}\frac{M_0^e \hat{z} - \mathbf{M}^e}{Q(P^e)} \\ \frac{\partial \mathbf{M}^n}{\partial t} &= \gamma_n(\mathbf{B} + \lambda \mathbf{M}^e) \times \mathbf{M}^n + R_{sd}^n(M_0^n \hat{z} - \mathbf{M}^n).\end{aligned} \tag{5.9}$$

Here, the polarization terms in Eq (5.8) are absorbed into the terms $\mathbf{M}^e$ and $\mathbf{M}^n$. The light shift $\mathbf{L}$ can be minimized because the resonance frequency of the Rb D1 transition is not near the resonance frequency of the K D1 transition, and the linearly polarized probe beam does not contribute to the term. The terms R_{Total} and R_{sd}^n are generalized relaxation rates for the K and the ^{3}He atoms, respectively. We can solve Eq (5.9) for separate components of $\mathbf{M}^e$

$$\begin{aligned}\frac{\partial M_x^e}{\partial t} &= -R_{Total}\frac{M_x^e}{Q(P^e)} + \frac{\gamma_e}{Q(P^e)}((B_y + \lambda M_y^n)M_z^e - (B_z + \lambda M_z^n)M_y^e) \\ \frac{\partial M_y^e}{\partial t} &= -R_{Total}\frac{M_y^e}{Q(P^e)} + \frac{\gamma_e}{Q(P^e)}((B_z + \lambda M_z^n)M_x^e - (B_x + \lambda M_x^n)M_z^e) \\ \frac{\partial M_z^e}{\partial t} &= R_{Total}\frac{M_0^e - M_z^e}{Q(P^e)} + \frac{\gamma_e}{Q(P^e)}((B_x + \lambda M_x^n)M_y^e - (B_y + \lambda M_y^n)M_x^e).\end{aligned} \tag{5.10}$$

If we let $M_\perp^e = M_x^e + iM_y^e$, Eq (5.10) can be simplified even further into the transverse component $\partial M_\perp^e / \partial t$.

A similar procedure can be done for $\frac{\partial \mathbf{M}^n}{\partial t}$. The results for both the electron and nuclear spins are

$$\begin{aligned}\frac{\partial M_\perp^e}{\partial t} &= -R_{Total}\frac{M_\perp^e}{Q(P^e)} - \frac{\gamma_e}{Q(P^e)} i(\lambda M_z^e M_\perp^n - (B_z + \lambda M_z^n) M_\perp^e) \\ \frac{\partial M_\perp^n}{\partial t} &= -R_{sd}^n M_\perp^n - \gamma_n i(\lambda M_z^n M_\perp^e - (B_z + \lambda M_z^e) M_\perp^n),\end{aligned} \tag{5.11}$$

where I have set $B_x = B_y = 0$.

Because the amount of the magnetic field exerted by the K and ^{3}He atoms are different, the amount of the magnetic fields experienced by the electron spins B_z^e and experienced by the nuclear spins B_z^n are

$$\begin{aligned}B_z^e &= B_{ext,z} + \lambda M^n P_z^n \\ B_z^n &= B_{ext,z} + \lambda M^e P_z^e\end{aligned} \tag{5.12}$$

where $B_{ext,z}$ is the external magnetic field. Strongly coupled spin dynamics occur when the external field $B_{ext,z}$ is set to make $B_z^e = 0$. This point is called the "compensation point" and at this point, the magnetic field that K atoms experience from ^{3}He becomes zero [20]. In other words

$$B_{z,ext,comp} = -\lambda M^n P_z^n - \lambda M^e P_z^e. \tag{5.13}$$

Near this compensation point, even though the γ_e and γ_n are many orders of magnitude different, the electron and nuclear spins are "locked" and precess in resonance. This is because the fields that the K and ^{3}He experience are different in such a way that their precession frequencies are similar. The use of the nuclear polarization of ^{3}He atoms is of interest because ^{3}He has a very long coherent spin precession time. The reported transverse and longitudinal relaxation times of ^{3}He are 1000 seconds and 2 hours, respectively [46]. On the other hand, the relaxation time for electron spins (such as in the system with K atoms) is on the order of 5-10 milliseconds [28]. At this compensation point, the character of the ^{3}He long coherent spin precession gets "mapped" onto the K spin precession.

5.1.4 Comagnetometer Transient Response

At the compensation point in Eq (5.13) and setting **B** and **L** to be zero in Eq (5.8), the steady state P_x^e is calculated to be [20]

$$P_x^e = \frac{P_z^e \gamma_e}{R_{Total}}(b_y^n - b_y^e). \tag{5.14}$$

Here, we can see that the comagnetometer signal P_x^e is proportional to the difference between the fields that couple to the nuclear and the electron spins. For a normal magnetic field, the couplings to the nuclear and the electron spins are the same; as a result, the comagnetometer signal does not change. However, if this coupling is due to some anomalous effect, the couplings would be different, and the comagnetometer signal would change.

As Eq (5.14) suggests, the comagnetometer is insensitive to the transverse magnetic fields. Figure 5.2 shows the mechanism of this effect. In Figure 5.2, the external magnetic field $B_{ext,z}$ is applied in the **z** direction to cancel out the field generated by the ^{3}He atoms on the K atoms, so the K atoms feel no magnetic field. When a small field perpendicular to the **z** axis is introduced, the ^{3}He polarization adiabatically follows the total magnetic field and cancels out the new transverse field to first order [46]. In other words, as long as $B_x, B_y \ll B_z$, the ^{3}He spins re-align themselves to cancel out the magnetic field, and the K atoms remain unaffected by it. This effect is very beneficial in reducing low-frequency noise from the magnetic shields or other slow external magnetic drifts [20].

5.1.5 Response to a Transverse Excitation

We modeled the comagnetometer's response to a transverse excitation. As discussed in section 5.1.3, at the compensation point, the K and ^{3}He are "locked" together, and they precess in resonance frequency. In other words, the coherent spin precession time for the K atoms increases, and the coherent spin precession time for the ^{3}He atoms decreases. We solved Eq (5.10) numerically using experimental parameters that are reported in Ref. [20]. The solutions are shown in Figure 5.3.

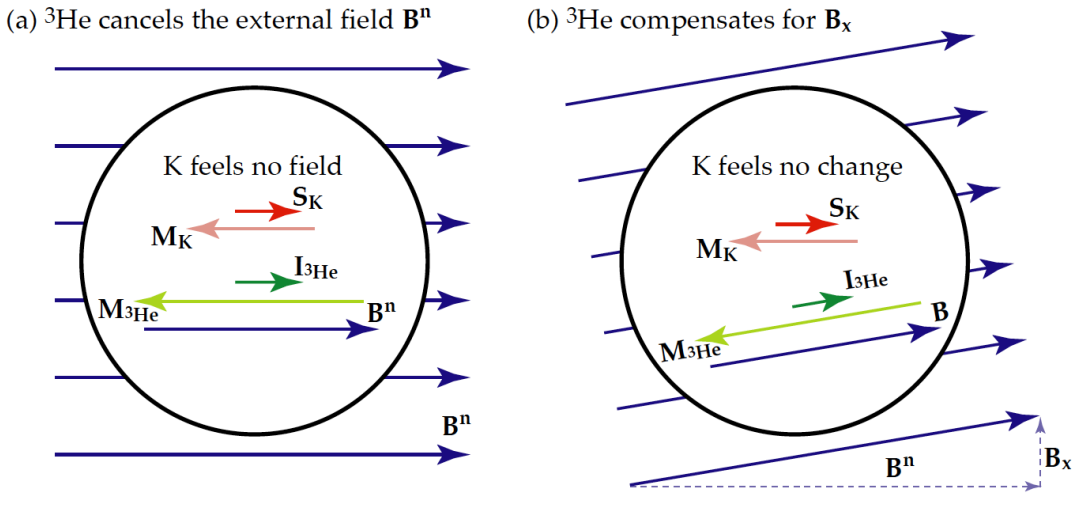

Figure 5.2: Cartoons which represent the mechanism through which the comagnetometer becomes insensitive to a magnetic field that is transverse to the polarizing axis. (a) The external magnetic field (denoted as $\mathbf{B^n}$ in the figure) is applied in such a way that electronic spins of the K atoms feel no magnetic field. (b) When some magnetic field that is transverse to the polarizing axis is introduced, the ^{3}He polarization adiabatically follows the magnetic field. The K electronic spins remain unaffected by the magnetic drift. The figure is directly from Ref. [20].

For each plot, a different amount of the external magnetic field was applied. Some of the plots have both high-frequency and low-frequency oscillations–this suggests that the applied magnetic field is not at the compensation point for those plots. However, near $B_{z,ext} = -0.001076$ mG (third from the top in the right column), we only see one frequency response–this suggests that the applied magnetic field is at the compensation point and the spins of the K and ^{3}He atoms have been properly coupled.

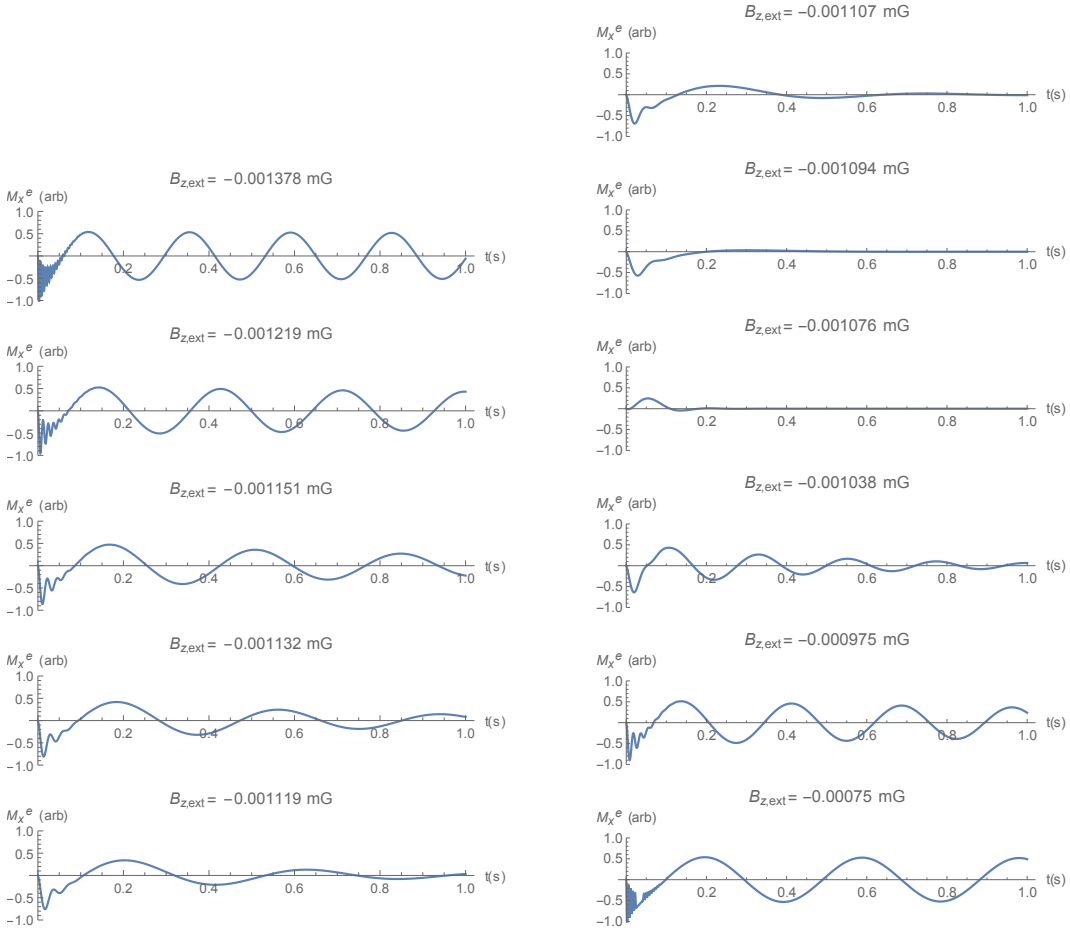

Figure 5.3: Numerically solved solutions to Eq (5.10). A transverse excitation of the magnetization M_y was added at $t = 0$. Different amounts of $B_{ext,z}$ were applied to investigate the behaviors at and away from the compensation point described by Eq (5.13). At the compensation point, the electronic and the nuclear spins precess in resonance as shown in the plot with $B_{ext,z} = -0.001076$ mG (third from the top in the right column). If $B_{ext,z} \neq$ compensating point, the electronic and nuclear spin precessions appear independently. The high frequency oscillation is due to the electronic spin precession, and the lower frequency oscillation is due to the nuclear spin precession. The parameters used in the model were from Ref. [20].

5.2 Experimental Setup

The schematic of the magnetometer is shown in Figure 5.4. It is a double-beam spin exchange relaxation-free (SERF) magnetometer using hybrid pumping of Rb and K atoms. The same K laser, vapor cell, magnetic shields, and electronics were used as the K magnetometer described in Chapter 3.

The pump beam is generated by a tampered amplified diode laser system at the Rb D1 transition (795 nm). The Rb laser system has primary and secondary lasers. The current and the temperature of the primary laser are used to tune the wavelength of the Rb laser, and the current of the secondary laser is used to control the power of the laser, which can be up to 3 W.

The pump beam is circularly polarized and propagates along the **x**-axis. Similar to the K magnetometer, the optical pumping of only the electronic spins of the Rb and K atoms can be considered because the hyperfine structure is not resolved in the homogeneous broadening. The pump beam puts the Rb atoms into the Rb dark state $M_x = +1/2$ by the same mechanism shown in Figure 2.3. The Rb atoms polarize the K atoms and put the K atoms into the K dark state $M_x = +1/2$ via spin-exchange collisions.

The hybrid pumping works under the assumption that the spin states of Rb and K atoms are exactly the same. This means that both beams should have the same light profile. In addition, both beams should be perfectly aligned to each other; this is because if there is a small angle difference $d\theta$ between the pump and the probe laser beams, the spin states for the Rb and K atoms are M_θ and $M_{\theta+d\theta}$. This would result in the broadening of the magnetic resonance. To obtain pump and probe beams that are perfectly aligned with respect to each other, the pump and the probe lasers are fiber-coupled together. A waveplate, which was used in the K magnetometer to circularly polarize the K laser, is wavelength-specific. In the hybrid pumping magnetometer, a Fresnel-Rhomb polarizer, which has a weaker wavelength dependence, is used to circularly polarize both the Rb and K lasers.

After the light travels through the vapor cell, we only want to monitor the probe

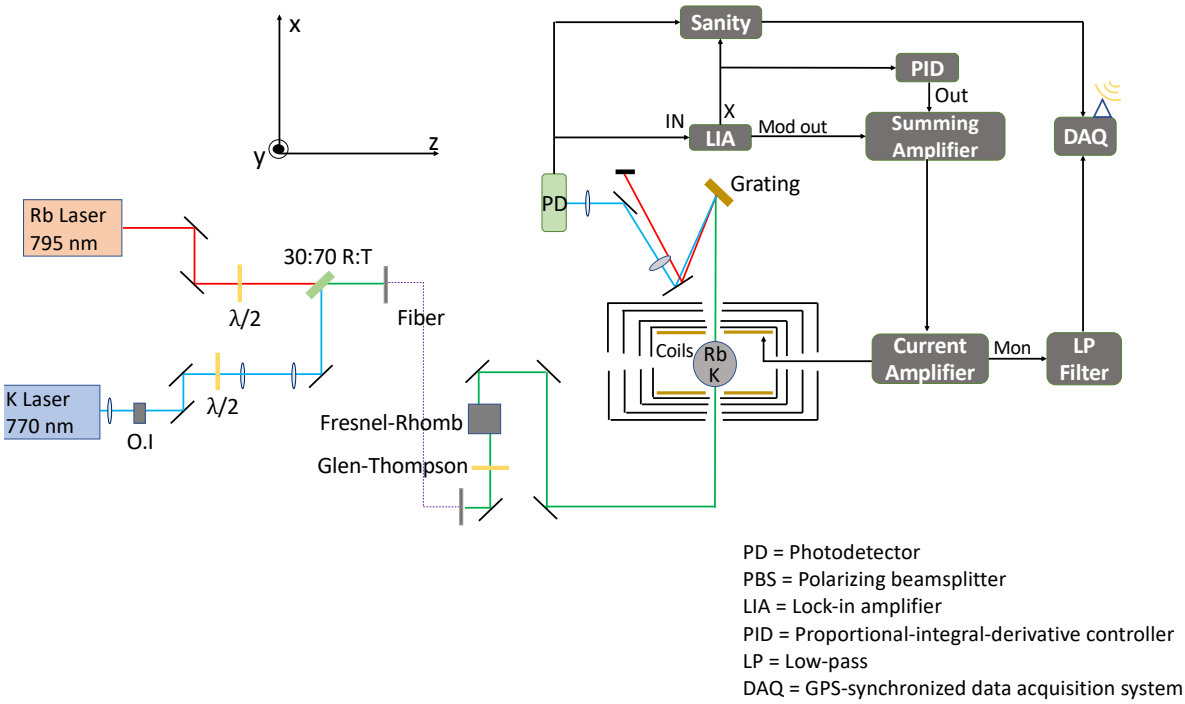

Figure 5.4: Schematic of the upgraded K magnetometer with Rb-K hybrid pumping. Basic principles of the upgraded K magnetometer are the same as the K magnetometer described in Chapter 3. A pump beam tuned at the Rb D1 transition was added co-linearly to the existing K D1 transition. The two beams are combined at the 30:70 R:T beamsplitter. The combined beam is fiber coupled with a polarization maintaining fiber to ensure the spatial overlap of the two beams. Both beams are circularly polarized by the Fresnel-Rhomb polarizer. The pump beam polarizes the Rb atoms in the vapor cell. The Rb atoms polarize the K atoms via spin-exchange collisions. This mechanism of hybrid pumping is used to increase the polarization of the K atoms in the vapor cell and ultimately to increase the sensitivity of the magnetometer.

beam. Since the pump and the probe beams are spatially overlapped, a diffraction grating was placed after the shields to separate the beams.

Detection is done in exactly the same way as the K magnetometer: the probe beam

is also circular and travels through the center of the vapor cell and is directed onto a photodetector. The circularly polarized probe beam will probe the K dark state. In the presence of a magnetic field orthogonal to the polarized axis, the K atoms will come out of the dark state, resulting in decreased transmission. The relation between the transmission and the magnetic field is used to detect a magnetic field.

5.3 K and Rb Absorption

As discussed in section 2.3.3 and 4.2, the line shape of the broadened spectral line depends on the number of atoms. Figure 5.5 shows the absorption spectral line of the K D1 transition and the Rb D1 transition through the vapor cell. The temperature of the vapor cell was set at 165 °C. The K D1 transition in Figure 5.5 is the same as shown in Figure 4.3. The y-scale of the plot is in a log scale, and x offsets were added to both the K and Rb spectral lines for visual comparison. The power of the K and the Rb lasers were 5 μW and 8 μW, respectively. Both beams were linearly polarized.

The pressure broadened spectral lines of the K and the Rb atoms were fitted to Eq (2.24). The densities of the K and Rb atoms from the fits are $n_{\mathrm{K}} = 8.4 \times 10^{13}$ cm^{-3} and
$n_{\mathrm{Rb}} = 1.2 \times 10^{13}$ cm^{-3}, respectively. The vapor cell was designed to have Rb-K in a 1:9 ratio. However, the measured densities suggest that Rb-K are in a 1:7 ratio. The density of $n_{\mathrm{K}} = 8.4 \times 10^{13}$ cm^{-3} suggests that the actual temperature of the vapor cell is $\sim$ 185 °C, as discussed in section 4.2.

5.4 Hybrid Pumping with Rb Pump Beam

As discussed in section 5.1.2, the hybrid pumping of the Rb-K ensemble results in a better polarization of the K atoms. Therefore, we expect the fraction of atoms that are in the dark state to increase with increased Rb pump power.

Figure 5.6 shows the fractional transmission of the probe beam as a function of Rb pump power. The power of the K probe beam was kept constant at $\sim$ 600 μW. The

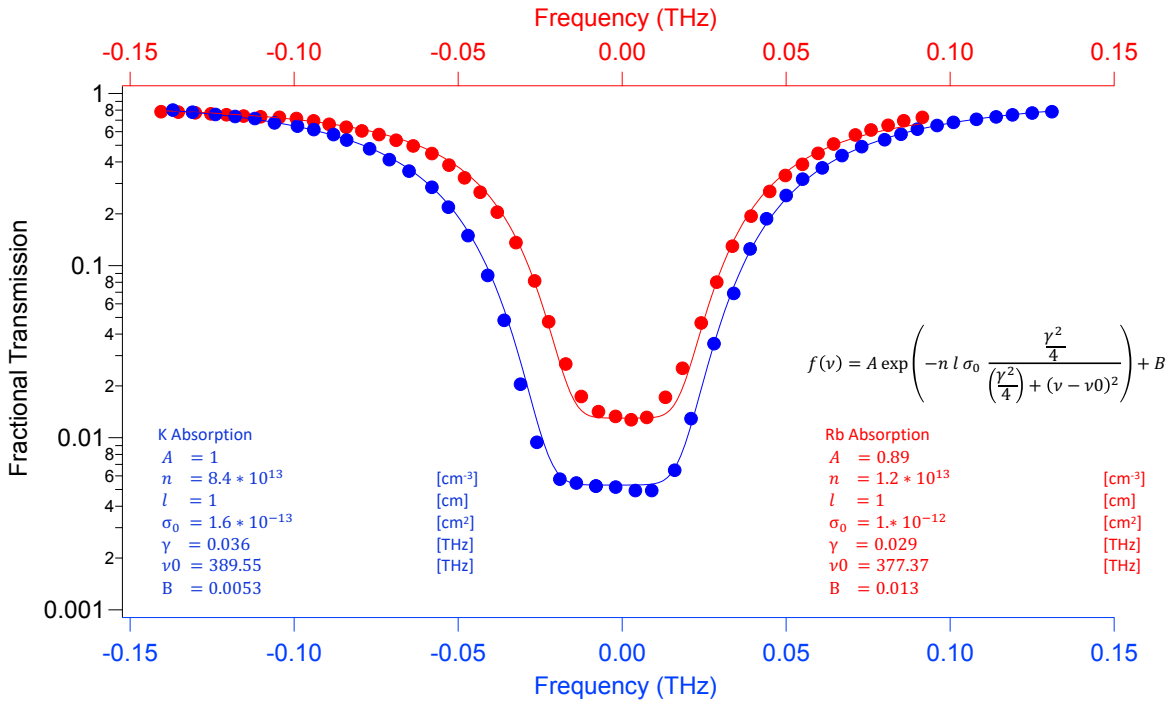

Figure 5.5: The fractional transmission of the K and Rb atoms as a function of frequency for the K D1 absorption (blue) and the Rb D1 absorption (red). For both, x offsets were added for comparison. The temperature of the vapor cell was set at 165 °C for both measurements. The power of the K and Rb lasers were 5 μW and 8 μW, respectively. Each absorption line was fitted to Eq (2.24). The ratio of the densities of the Rb to K atoms is determined to be 1:7.

power of the Rb pump laser was varied by changing the current of the secondary laser.

As expected, the fractional transmission of the probe beam increases as a function of Rb pump power in Figure 5.6. The fractional transmission jumps up with the addition of the Rb laser, even at low power. This suggests that hybrid pumping does improve the polarization of the K atoms. After the Rb power is about 50 mW, the increase in the fractional transmission becomes more gradual.

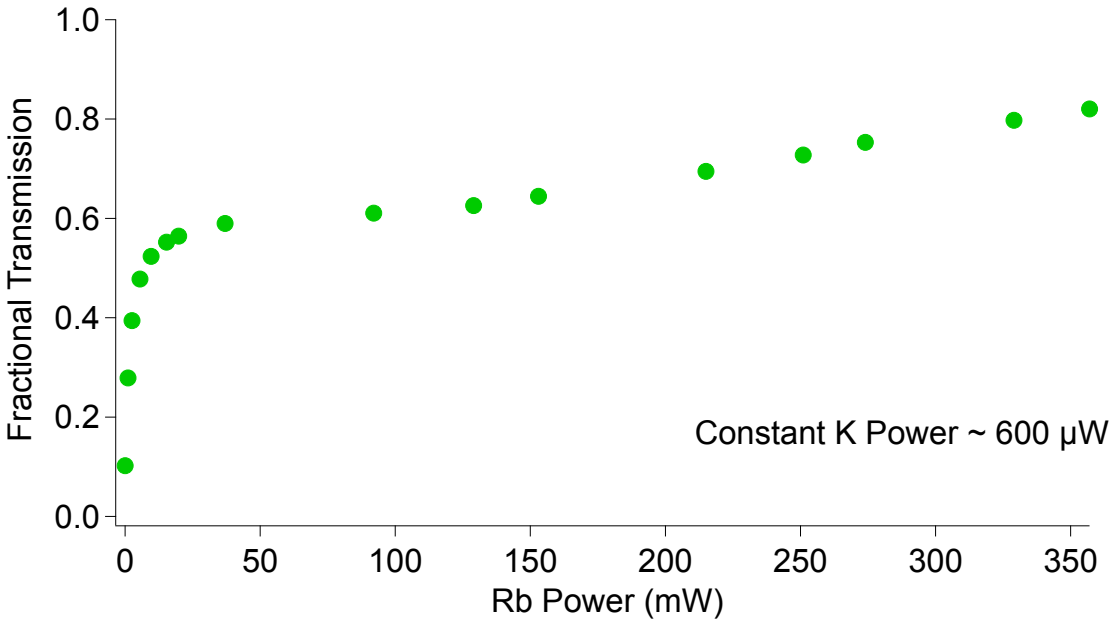

Figure 5.6: Fractional transmission of the K probe beam as a function of the Rb pump beam power. The power of the K probe beam was kept at 600 μW. The higher fractional transmission corresponds to a higher number of polarized K atoms in the vapor cell. We can clearly see the effect of hybrid pumping as soon as the Rb pump beam is added to the system. After about 50 mW of the pump beam, the increase in the fractional transmission is more gradual.

5.5 Unexpected Power Broadening

In section 4.5, we observed the broadening of the magnetic resonance in B_z with increasing K pump beam power. We observed similar broadening with the Rb pump power. Figure 5.7 shows the width and the amplitude of the magnetic resonance as a function of the Rb laser current. Higher Rb secondary current corresponds to higher Rb beam power. The power of the K probe beam was kept constant at ~ 780 μW.

As we can see in Figure 5.7, the amplitude of the magnetic resonance increases as the Rb current increases–this is to be expected because as we are pumping more and more K atoms into the dark state, the transmission of light on the peak of the magnetic

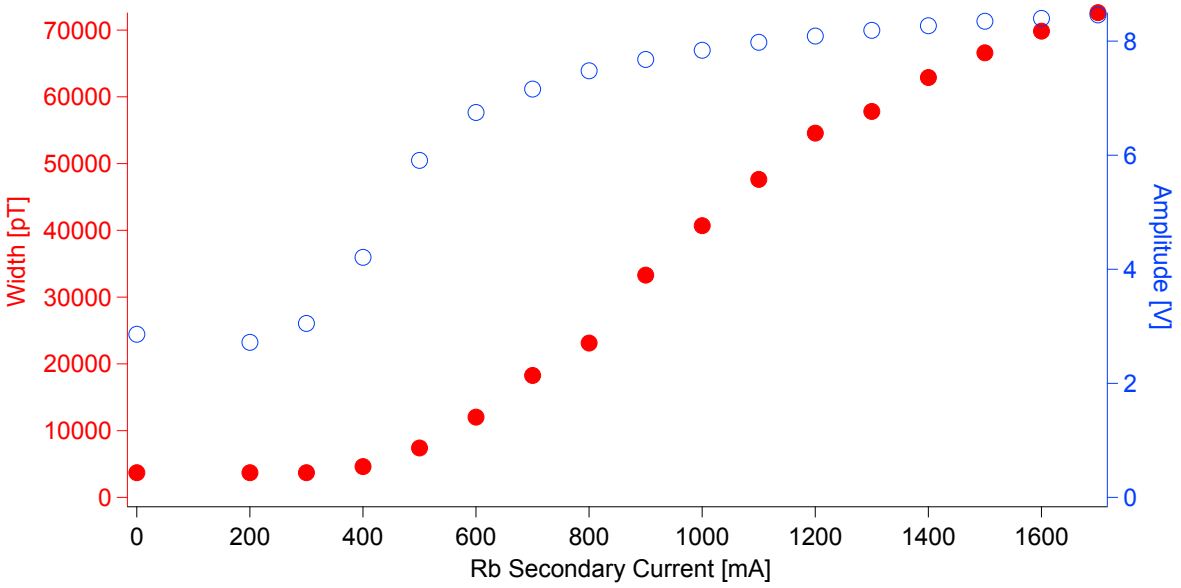

Figure 5.7: The width (filled red) and the amplitude (open blue) of the magnetic resonance in B_z as a function of the Rb secondary current, where higher secondary current corresponds to higher power. The power of the K probe beam was kept constant at ~ 780 μW. The amplitude of the magnetic resonance increases with higher power, as expected. The width also increases with power.

resonance should increase (see section 2.7). However, the width of the magnetic resonance also increases as a function of the Rb laser power. This is unexpected, and we do not understand this apparent power broadening of the magnetic resonance. There are possible reasons that may explain this power broadening. For instance, it could be that both Rb and K lasers are not aligned with respect to the axes of the shields; when we scan the B_z field, the **z**-axis may not be the **z**-axis of the polarized atoms, and this would result in broadening of the magnetic resonance.

Chapter 6

Conclusion

The construction and the characterization of the K magnetometer were presented in this thesis. Some investigations of the hybrid pumping effect have also been conducted.

Several future projects are planned for the Oberlin station. The power broadening of the magnetic resonance will be explored in more detail. More careful measurements will be carried out for factors such as the densities of the atoms in the vapor cell, the relaxation times, etc. The most significant future project is the construction of the Rb-K-^{3}He comagnetometer which will have higher sensitivity.

The GNOME collaboration continuously works to improve the sensitivity of our magnetometers. Higher sensitivity will allow us to put tighter constraints on the mass and the coupling constants of exotic particles. Most magnetometers in the network have lower sensitivities than expected for optical atomic magnetometers. In the future, improvements will be made to bring the actual sensitivities closer to the fundamental sensitivities. Additionally, four stations in GNOME are planning to implement comagnetometers. The stations in Mainz, Germany and Oberlin, USA will build Rb-K-^{3}He comagnetometers with K as the majority species and Rb as the minority species. The stations in Krakow, Poland and Hayward, USA will build Rb-K-^{3}He comagnetometers with Rb as the majority species and K as the minority species.

Because we are taking data continuously from several stations at a sampling rate of 512 Hz, the collaboration has a large quantity of data. In addition, the analysis of

the data is not trivial; each magnetometer has its own sensitive axis, which changes as the earth rotates. When we do coincident analyses, all of the sensitive axes must be accounted for. The magnetometers at each station use different atomic species, which may couple differently to exotic particles, causing different signal amplitudes. In addition, we do not know what the signal would look like. The collaboration is working on two main types of data analysis. In one, which is model-specific, we fit the data to a specific type of signal (i.e. Gaussian) and check to see if we can find any such signals among the stations within a timeframe that would be consistent with the model. The other type is model-independent. Some examples of model-independent data analysis methods that the collaboration is using include excess power and machine learning techniques. These methods are being implemented to search for any abnormalities within the data.

While our current efforts have been aimed at detecting ALP domain walls, it is possible that our magnetometers could detect other exotic spin-coupling interactions that are not predicted by the Standard Model. Therefore, the collaboration explores other models that the network would be sensitive to.

GNOME can also be used as an ELF (Exotic Light Field) telescope. It is possible that cosmological events such as supernovae or neutron-star mergers release enough energy to produce exotic particles. The collaboration looks at reports on such events by LIGO or other telescopes to see if the magnetometers were operating at the time during which such events occurred. If we do have data during those time periods, we go back and try to see if there are any abnormalities in our data that could correspond to exotic particles.

As mentioned in the Introduction, the GNOME experiment is unique in the sense that it is probing the ultralight regime of the ALPs, which has not been explored extensively by other experiments. This allows us to put constraints on exotic particles in the lower mass regime in the parameter space. In combination with other experiments that search for dark matter, this allows physicists to further narrow down the remaining possibilities for what dark matter could consist of. Even if no signals are ever detected, we will still be closer to uncovering the nature of dark matter.

Appendix A

The homemade low-noise current supply is used to apply currents to the five first-order gradients coils $dB_z/dz, dB_y/dy, dB_z/dx, dB_y/dx$, and dB_z/dy, and the second-order gradient d^2B_z/dz^2. The schematic of the current supply is shown in Figure A.1.

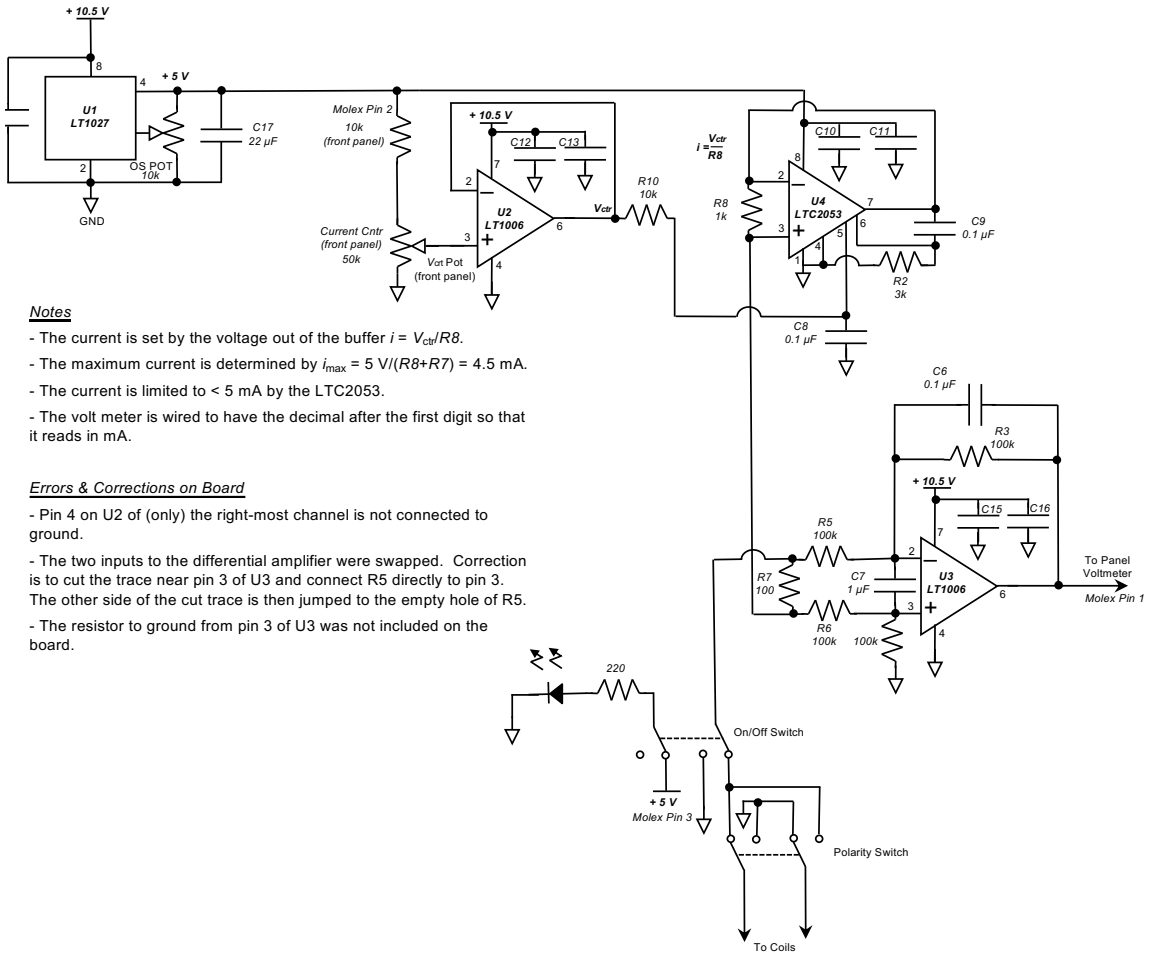

Figure A.1: The schematic of the homemade low-noise current supply used to apply currents to the magnetic coils.

Bibliography

[1] Lars Bergström. "Dark matter candidates". In: *New Journal of Physics* 11.10 (Oct. 2009), p. 105006. DOI: 10.1088/1367-2630/11/10/105006. URL: https://doi.org/10.1088%2F1367-2630%2F11%2F10%2F105006.

[2] Gianfranco Bertone, Dan Hooper, and Joseph Silk. "Particle dark matter: evidence, candidates and constraints". In: *Physics Reports* 405.5 (2005), pp. 279–390. ISSN: 0370-1573. DOI: https://doi.org/10.1016/j.physrep.2004.08.031. URL: http://www.sciencedirect.com/science/article/pii/S0370157304003515.

[3] R. D. Peccei and Helen R. Quinn. "Constraints imposed by CP conservation in the presence of pseudoparticles". In: *Phys. Rev. D* 16 (6 Sept. 1977), pp. 1791–1797. DOI: 10.1103/PhysRevD.16.1791. URL: https://link.aps.org/doi/10.1103/PhysRevD.16.1791.

[4] Asimina Arvanitaki et al. "String axiverse". In: *Phys. Rev. D* 81 (12 June 2010), p. 123530. DOI: 10.1103/PhysRevD.81.123530. URL: https://link.aps.org/doi/10.1103/PhysRevD.81.123530.

[5] Peter W. Graham, David E. Kaplan, and Surjeet Rajendran. "Cosmological Relaxation of the Electroweak Scale". In: *Phys. Rev. Lett.* 115 (22 Nov. 2015), p. 221801. DOI: 10.1103/PhysRevLett.115.221801. URL: https://link.aps.org/doi/10.1103/PhysRevLett.115.221801.

[6] Peter W. Graham et al. "Experimental Searches for the Axion and Axion-Like Particles". In: *Annual Review of Nuclear and Particle Science* 65.1 (2015), pp. 485–

514. DOI: 10.1146/annurev-nucl-102014-022120. eprint: https://doi.org/10.1146/annurev-nucl-102014-022120. URL: https://doi.org/10.1146/annurev-nucl-102014-022120.

[7] C. Hagmann et al. "Results from a search for cosmic axions". In: *Phys. Rev. D* 42 (4 Aug. 1990), pp. 1297–1300. DOI: 10.1103/PhysRevD.42.1297. URL: https://link.aps.org/doi/10.1103/PhysRevD.42.1297.

[8] S. Al Kenany et al. "Design and operational experience of a microwave cavity axion detector for the 20–100 μeV range". In: *Nucl. Instrum. Meth.* A854 (2017), pp. 11–24.

[9] Andreas Ringwald. "Exploring the role of axions and other WISPs in the dark universe". In: *Physics of the Dark Universe* 1.1 (2012). Next Decade in Dark Matter and Dark Energy, pp. 116–135. ISSN: 2212-6864. DOI: https://doi.org/10.1016/j.dark.2012.10.008. URL: http://www.sciencedirect.com/science/article/pii/S221268641200012X.

[10] Dmitry Budker et al. "Proposal for a Cosmic Axion Spin Precession Experiment (CASPEr)". In: *Phys. Rev. X* 4 (2 May 2014), p. 021030. DOI: 10.1103/PhysRevX.4.021030. URL: https://link.aps.org/doi/10.1103/PhysRevX.4.021030.

[11] Igor G. Irastorza and Javier Redondo. "New experimental approaches in the search for axion-like particles". In: *Progress in Particle and Nuclear Physics* 102 (2018), pp. 89–159. ISSN: 0146-6410. DOI: https://doi.org/10.1016/j.ppnp.2018.05.003. URL: http://www.sciencedirect.com/science/article/pii/S014664101830036X.

[12] M. Pospelov et al. "Detecting Domain Walls of Axionlike Models Using Terrestrial Experiments". In: *Phys. Rev. Lett.* 110 (2 Jan. 2013), p. 021803. DOI: 10.1103/PhysRevLett.110.021803. URL: https://link.aps.org/doi/10.1103/PhysRevLett.110.021803.

[13] Szymon Pustelny et al. "The Global Network of Optical Magnetometers for Exotic physics (GNOME): A novel scheme to search for physics beyond the Standard Model". In: *Annalen der Physik* 525 (Sept. 2013). DOI: 10.1002/andp.201300061.

[14] S. Afach et al. "Characterization of the global network of optical magnetometers to search for exotic physics (GNOME)". In: *Physics of the Dark Universe* 22 (2018), pp. 162–180. ISSN: 2212-6864. DOI: https://doi.org/10.1016/j.dark.2018.10.002. URL: http://www.sciencedirect.com/science/article/pii/S2212686418301031.

[15] D. Budker et al. *Atomic Physics: An Exploration Through Problems and Solutions*. Oxford University Press, 2004. ISBN: 9780198509509.

[16] D.J. Griffiths. *Introduction to Quantum Mechanics*. Prentice Hall International Editions. Prentice Hall, 1994. ISBN: 9780131855137.

[17] E. Arimondo, M. Inguscio, and P. Violino. "Experimental determinations of the hyperfine structure in the alkali atoms". In: *Rev. Mod. Phys.* 49 (1 Jan. 1977), pp. 31–75. DOI: 10.1103/RevModPhys.49.31. URL: https://link.aps.org/doi/10.1103/RevModPhys.49.31.

[18] M. Auzinsh, D. Budker, and S. Rochester. *Optically Polarized Atoms: Understanding Light-atom Interactions*. OUP Oxford, 2010. ISBN: 9780199565122.

[19] Scott Jeffrey Seltzer. "Developments in Alkali-Metal Atomic Magnetometry". PhD thesis. Princeton University, 2008.

[20] Thomas Whitmore Kornack. "A Test of CPT and Lorentz Symmetry Using a K-^{3}He Co-magnetometer". PhD thesis. Department of Physics,Princeton University, 2005.

[21] A. Corney. *Atomic and Laser Spectroscopy*. Oxford Classic Texts in the Physical Sciences. OUP Oxford, 2006. ISBN: 9780199211456.

[22] Peter J. Mohr, David B. Newell, and Barry N. Taylor. "CODATA recommended values of the fundamental physical constants: 2014". In: *Rev. Mod. Phys.* 88 (3 Sept. 2016), p. 035009. DOI: 10.1103/RevModPhys.88.035009. URL: https://link.aps.org/doi/10.1103/RevModPhys.88.035009.

[23] Nicole Allard and John Kielkopf. "The effect of neutral nonresonant collisions on atomic spectral lines". In: *Rev. Mod. Phys.* 54 (4 Oct. 1982), pp. 1103–1182. DOI: 10.1103/RevModPhys.54.1103. URL: https://link.aps.org/doi/10.1103/RevModPhys.54.1103.

[24] Thomas J. Killian. "Thermionic Phenomena Caused by Vapors of Rubidium and Potassium". In: *Phys. Rev.* 27 (5 May 1926), pp. 578–587. DOI: 10.1103/PhysRev.27.578. URL: https://link.aps.org/doi/10.1103/PhysRev.27.578.

[25] I. K. Kikoin, ed. *Tablitsi Fizicheskikh Velichin (Tables of Physical Values)*. Atomizda, Moscow, 1976.

[26] H.J. Metcalf et al. *Laser Cooling and Trapping*. Graduate texts in contemporary physics. Springer, 1999. ISBN: 9780387987477.

[27] Thad G. Walker and William Happer. "Spin-exchange optical pumping of noble-gas nuclei". In: *Rev. Mod. Phys.* 69 (2 Apr. 1997), pp. 629–642. DOI: 10.1103/RevModPhys.69.629. URL: https://link.aps.org/doi/10.1103/RevModPhys.69.629.

[28] J. C. Allred et al. "High-Sensitivity Atomic Magnetometer Unaffected by Spin-Exchange Relaxation". In: *Phys. Rev. Lett.* 89 (13 Sept. 2002), p. 130801. DOI: 10.1103/PhysRevLett.89.130801. URL: https://link.aps.org/doi/10.1103/PhysRevLett.89.130801.

[29] W. Happer and H. Tang. "Spin-Exchange Shift and Narrowing of Magnetic Resonance Lines in Optically Pumped Alkali Vapors". In: *Phys. Rev. Lett.* 31 (5 July 1973), pp. 273–276. DOI: 10.1103/PhysRevLett.31.273. URL: https://link.aps.org/doi/10.1103/PhysRevLett.31.273.

[30] S. Appelt et al. "Theory of spin-exchange optical pumping of ^{3}He and ^{129}Xe". In: *Phys. Rev. A* 58 (2 Aug. 1998), pp. 1412–1439. DOI: 10.1103/PhysRevA.58.1412. URL: https://link.aps.org/doi/10.1103/PhysRevA.58.1412.

[31] L. Wilmer Anderson, Francis M. Pipkin, and James C. Baird. "N^{14}-N^{15} Hyperfine Anomaly". In: *Phys. Rev.* 116 (1 Oct. 1959), pp. 87–98. DOI: 10.1103/PhysRev.116.87. URL: https://link.aps.org/doi/10.1103/PhysRev.116.87.

[32] S. Kadlecek. PhD thesis. University of Wisconsin, Madison, 2000.

[33] W. C. Chen et al. "Spin-exchange optical pumping of ^{3}He with Rb-K mixtures and pure K". In: *Phys. Rev. A* 75 (1 Jan. 2007), p. 013416. DOI: 10.1103/PhysRevA.75.013416. URL: https://link.aps.org/doi/10.1103/PhysRevA.75.013416.

[34] A. Ben-Amar Baranga et al. "Polarization of ^{3}He by Spin Exchange with Optically Pumped Rb and K Vapors". In: *Phys. Rev. Lett.* 80 (13 Mar. 1998), pp. 2801–2804. DOI: 10.1103/PhysRevLett.80.2801. URL: https://link.aps.org/doi/10.1103/PhysRevLett.80.2801.

[35] D. Budker and D.F.J. Kimball. *Optical Magnetometry*. Cambridge University Press, 2013. ISBN: 9781107310827.

[36] J.S. Townsend. *A Modern Approach to Quantum Mechanics*. International series in pure and applied physics. University Science Books, 2000. ISBN: 9781891389139.

[37] F. Bloch. "Nuclear Induction". In: *Phys. Rev.* 70 (7-8 Oct. 1946), pp. 460–474. DOI: 10.1103/PhysRev.70.460. URL: https://link.aps.org/doi/10.1103/PhysRev.70.460.

[38] K. Blum. *Density Matrix Theory and Applications*. Physics of Atoms and Molecules. Springer US, 1996. ISBN: 9780306453410.

[39] D.J. Griffiths. *Introduction to Electrodynamics*. Prentice Hall, 1999. ISBN: 9780138053260.

[40] WILLIAM HAPPER. "Optical Pumping". In: *Rev. Mod. Phys.* 44 (2 Apr. 1972), pp. 169–249. DOI: 10.1103/RevModPhys.44.169. URL: https://link.aps.org/doi/10.1103/RevModPhys.44.169.

[41] Earl Babcock et al. "Hybrid Spin-Exchange Optical Pumping of H e 3". In: *Physical review letters* 91 (Oct. 2003), p. 123003. DOI: 10.1103/PhysRevLett.91.123003.

[42] E. Babcock. PhD thesis. University of Wisconsin, Madison, 2005.

[43] I. A. Nelson and T. G. Walker. "Rb-Xe spin relaxation in dilute Xe mixtures". In: *Phys. Rev. A* 65 (1 Dec. 2001), p. 012712. DOI: 10.1103/PhysRevA.65.012712. URL: https://link.aps.org/doi/10.1103/PhysRevA.65.012712.

[44] T. W. Kornack, R. K. Ghosh, and M. V. Romalis. "Nuclear Spin Gyroscope Based on an Atomic Comagnetometer". In: *Phys. Rev. Lett.* 95 (23 Nov. 2005), p. 230801. DOI: 10.1103/PhysRevLett.95.230801. URL: https://link.aps.org/doi/10.1103/PhysRevLett.95.230801.

[45] S. R. Schaefer et al. "Frequency shifts of the magnetic-resonance spectrum of mixtures of nuclear spin-polarized noble gases and vapors of spin-polarized alkali-metal atoms". In: *Phys. Rev. A* 39 (11 June 1989), pp. 5613–5623. DOI: 10.1103/PhysRevA.39.5613. URL: https://link.aps.org/doi/10.1103/PhysRevA.39.5613.

[46] T. W. Kornack and M. V. Romalis. "Dynamics of Two Overlapping Spin Ensembles Interacting by Spin Exchange". In: *Phys. Rev. Lett.* 89 (25 Dec. 2002), p. 253002. DOI: 10.1103/PhysRevLett.89.253002. URL: https://link.aps.org/doi/10.1103/PhysRevLett.89.253002.